

DEPARTMENT OF PHYSICS AND ASTRONOMY

UNIVERSITY OF HEIDELBERG

Master thesis in Physics
submitted by
Felix Kling
born in Staßfurt
2012

Tagging single tops

This Master thesis has been carried out by Felix Kling
at the Institut für Theoretische Physik
Universität Heidelberg
under the supervision of
Prof. Tilman Plehn

Abstract

The top quark is the heaviest known Standard Model particle and therefore plays an important role in new physics searches at LHC. Besides top pair production via strong interaction, the LHC will be able to observe electroweak single top production. In this thesis we analyze the possibility to extract the hadronic single top production mode in the boosted regime using the HEPTopTagger. Top tagging algorithms identify top quarks in geometrically large jets using their substructure. Based on this internal structure of the tagged top including filtering and pruning methods as well as b -tagging we are able to reject most multi-jet background events. We study the characteristics of the s -channel and t -channel single top production on a theoretical level to get a deeper understanding of their event topology. Using this knowledge we invented a way to measure the scattering angle directly which can be used to distinguish both production channels. Using the momentum distribution of the system consisting of the tagged top and hardest recoil jet and the internal structure of the recoil jet we are able to reject background events coming from top pair production. Finally, we achieve for both production channels a good signal resolution $S/B > 1$ with more than 5σ significance for the t -channel and a 3σ significance for the s -channel assuming 10 fb^{-1} luminosity at the 14 TeV LHC.

Zusammenfassung

Das Top Quark ist das schwerste im Standard Model enthaltende Teilchen dem daher bei der Suche nach neuer Physik am LHC große Bedeutung beigemessen wird. Neben der Produktion von Top Paaren werden wir auch in der Lage sein die Produktion einzelner Top Quarks mithilfe der elektro-schwachen Wechselwirkung zu beobachten. In dieser Abschlussarbeit wird die Möglichkeit der Entdeckung der voll hadronischen Produktion einzelner moderat geboosterter Top Quarks mithilfe des HEPTopTaggers analysiert. Top Tagger sind Algorithmen zur Identifikation von Top Quarks innerhalb großer Jets basierend auf deren Substruktur. Eine Analyse der internen Struktur des getaggeten Top Quarks unter der Zuhilfenahme von Filter- und Pruningmethoden sowie b -Tagging erlaubt es uns Multi-Jet Hintergrundereignisse auszusortieren. Um ein tieferes Verständnis für die zu erwartende Topologie von Signalereignissen zu erhalten werden die Eigenschaften der Produktionsprozesse einzelner Top Quarks im s - und t -Kanal theoretisch untersucht. Darauf basierend haben wir eine Möglichkeit gefunden den Streuwinkel direkt zu messen und die s - und t -Kanal Produktion einzelner Top Quarks zu unterscheiden. Die Impulsverteilung des Systems bestehend aus getaggetem Top Quark und dem dazugehörigen Rückstoß-Jet sowie dessen interne Struktur ermöglichen es Hintergrundereignisse durch die Produktion von Paaren von Top Quarks auszusortieren. Zusammenfassend erhalten wir für beide Produktionskanäle eine gute Auflösung $S/B > 1$ bei mehr als 5σ Signifikanz für den t -Kanal und einer 3σ Signifikanz für den s -Kanal bei einer Luminosität von 10 fb^{-1} am LHC mit 14 TeV.

Contents

1	Introduction	9
2	Theoretical Background	11
2.1	Standard Model	11
2.2	Electroweak interactions	12
2.3	QCD	13
2.4	Collider Phenomenology	14
3	Top Physics	17
3.1	Properties of the top quark	17
3.2	HEPTopTagger	19
3.3	Single Top production	22
3.4	Angular distribution in single top decay	28
4	Analysis	33
4.1	Event Generation	33
4.2	Top tag	34
4.3	Top and recoil jet system	38
4.4	Internal structure of the recoil jet	40
4.5	s -channel single top production	43
5	Results of event selection	45
5.1	t -channel at $\sqrt{s} = 8$ TeV	45
5.2	s -channel at $\sqrt{s} = 8$ TeV	47
5.3	Single top at $\sqrt{s} = 14$ TeV	48
6	Conclusion and Outlook	51
A	Delphes	55
A.1	What Delphes does	55
A.2	Isolated leptons	56
A.3	Tagging behavior	58
A.4	Tagging efficiency	61

Chapter 1

Introduction

Our current understanding for the physics of elementary particles and their interactions is summarized in the Standard Model of particle physics. It incorporates three of the four fundamental forces and has been able to accurately describe almost all observations in particle physics. Although the Standard Model is successful at describing physics at small scales we believe it to be a low energy approximation of a more fundamental theory. Such beliefs are motivated by observations in cosmology. Dynamics at cosmological scales is dominated by the gravitational force, which in this regime is well described by general relativity. However, at the level of fundamental interactions, there is no suitable framework to describe gravity, hence it has not been incorporated in the Standard Model. It is this dichotomy that motivates the idea that the Standard Model is an approximation of a more fundamental theory. Galactic rotation curves [1] suggest the existence of dark matter which is not identical with any particle of the Standard Model. Furthermore observations of distant supernovae and the cosmic microwave background [2, 3] predict that the expansion of the universe is driven by dark energy. According to these observations only 5% of the energy content of the universe can be explained by Standard Model particles while the rest consists of dark matter and dark energy [4].

Besides these cosmological observations there are theoretical problems within the Standard Model such as the fine-tuning problem [5] or neutrino masses [6]. Furthermore, the Standard Model is unable to explain the asymmetry between baryonic and anti-baryonic matter needed for the formation of galaxies and stellar objects [7]. Theories of physics beyond the Standard Model, like Supersymmetry [5], have been postulated to solve these problems. Some of them might be observable at the LHC, which is the currently world's highest energy collider.

Due to its large mass close to the scale of electroweak symmetry breaking the top quark is expected to be a window towards new physics. Since the top quark decays before hadronization it is a unique laboratory to test the behavior of a free quark. Most of its properties like mass, charge and W -helicity fraction have been measured at the Tevatron [8, 9, 10, 11]. These measurements are mainly based on the observation of top pair production. The Standard Model also predicts top quarks to be produced via electroweak interactions. We distinguish three single top production modes. In s -channel single top production, a top produced in association with a b -quark through a time-like virtual W -boson. tq production via a space-like W -boson is called t -channel single top production. In a third process, the top is produced in association with a real W -boson.

Since the tbW -vertex is proportional to the squared CKM matrix element V_{tb} the observation of single top production allows us to measure V_{tb} directly. Due to unitarity of the CKM matrix we assume $V_{tb} > 0.999$ which is consistent with the combined result of Tevatron which sets a lower limit $V_{tb} > 0.77$ with 95% C.L. [12]. Deviations in the measured cross section for any of the three single top production processes from its expected value could be a first hint towards physics beyond the Standard Model. A fourth generation, heavy W' gauge boson or flavour-changing neutral currents would be examples for such theories [13, 14, 15] .

Both the CDF and D0 experiments at the Tevatron measured the production cross section for the different single top production channels separately. At CDF, the resulting ratio between s -channel and t -channel single top cross section shows a 2.5σ deviation from the Standard Model prediction while their sum is consistent with the Standard Model [16, 17]. For D0 the results agree with the

Standard Model [18, 19, 20]. This discrepancy has not disappeared after using a larger integrated luminosity. The results still differ at the 3σ level [21, 22]. To get a deeper understanding of single top production we need to analyze this process at the LHC. For an analysis we have to take into account that at the LHC the production cross section for s -channel single top is much smaller than for the t -channel single top and therefore their cross section ratio will be small.

In our analysis we concentrate on hadronically decaying tops which can be detected using top tagging algorithms [23, 24, 25, 26, 27, 28]. These identify tops inside geometrically large jets using their jet substructure [29, 30, 31, 32, 33, 34, 35]. An efficient algorithm to tag moderately boosted tops is the HEPTopTagger [36, 37, 38, 39, 40]. Focusing on the boosted regime $p_{T,t} > 200$ GeV has the additional advantage that the cross section ratio between s -channel and t -channel single top production increases by a factor of two. Unfortunately this also enhances the top-pair background.

In this thesis, we study the possibility of extracting fully hadronic single top production using top tagging. In the first part, we summarize important aspects of the Standard Model needed for the understanding of single top production. Basic concepts of collider phenomenology are reviewed. In the second part is contained a detailed description of the top tagging algorithm. We analyze the s -channel and t -channel single top production cross section to get a deeper understanding of their kinematic distributions. This knowledge is used in the third part to develop a strategy for separate identification of both production channels. A set of selection cuts based on properties of the tagged top and the recoil jet is introduced. In chapter 5 we show the analysis results for both single top production channels at LHC energies of 8 TeV and 14 TeV.

The work presented in this thesis was done together with Tilman Plehn and Michihisa Takeuchi and follows the discussion done in [41].

Chapter 2

Theoretical Background

2.1 Standard Model

The Standard Model (SM) of particle physics is our current theory to describe elementary particles and their interactions using the framework of Quantum Field Theory (QFT). A detailed description of QFT and the SM can be found in [42, 43, 44] and references therein. Some important results are presented in this and the following chapters. The particles are classified as quarks, leptons, gauge bosons and the Higgs boson. Quarks and leptons are spin- $\frac{1}{2}$ fermions, gauge bosons have spin-1 while the Higgs boson is predicted to be spin-0. Let us first write down a Lagrangian for free quarks and leptons. It contains a kinetic and a mass term for each field ψ

$$\mathcal{L} = i\bar{\psi}\gamma^\mu\partial_\mu\psi - m_\psi\bar{\psi}\psi \quad (2.1)$$

where m_ψ is the mass of the particle. The quarks and leptons are grouped into three generations. Each generation consist of a charged lepton, a neutral neutrino and an up-type and down-type quark. These particles are summarized in Tab. 2.1. Although we know from neutrino oscillation experiments [6] that neutrinos must have a mass we will treat them as massless in the SM. Each of the quarks and leptons has an anti-particle with the same mass but opposite quantum numbers.

generation	quark flavour	quark mass	lepton flavour	lepton mass
I	up u	$2.3^{+0.7}_{-0.5}$ MeV	electron e	0.511 MeV
	down d	$4.8^{+0.7}_{-0.3}$ MeV	e -neutrino ν_e	< 2 MeV
II	charm c	1.275 ± 0.025 GeV	muon μ	105.7 MeV
	strange s	95 ± 5 MeV	μ -neutrino μ_ν	< 0.19 MeV
III	top t	173.5 ± 1.4 GeV	tau τ	1.77 GeV
	bottom b	4.18 ± 0.03 GeV	τ -neutrino ν_τ	< 18.2 MeV

Table 2.1: Summary of quarks and leptons. Masses are taken from [45, 46, 6].

To describe interactions we require the theory to respect gauge symmetries. This implies that the Lagrangian has to be invariant under symmetry transformations. A symmetry transformation $SU(N)$ is described by a unitary operator U acting on the fields $\psi \rightarrow U\psi$. This operator can be expressed as linear combination of the $N^2 - 1$ group generators T^a with real coefficients $\theta_a(x)$.

$$U(\theta) = \exp(i\theta_a T^a) \quad (2.2)$$

Since the gauge theory is local, these coefficients θ will depend on the position in space time. The algebra of the generators is defined by their commutation relation

$$[T^a, T^b] = if^{abc}T_c \quad (2.3)$$

where f^{abc} are the structure coefficients of the group. Since the transformation is unitary the mass terms will be invariant under such a transformation. If we want to construct a kinetic term for the Lagrangian that is invariant under the symmetry transformation we have to replace the partial derivative ∂^μ by a covariant derivative

$$D^\mu = \partial^\mu - igA_a^\mu T^a \quad (2.4)$$

where we have introduced $N^2 - 1$ gauge fields A_a^μ . Under a gauge transformation this covariant derivative transforms into

$$D^\mu \rightarrow UD^\mu U^\dagger. \quad (2.5)$$

This implies that a covariant derivative acting on a field transforms like the field itself $D^\mu\psi \rightarrow UD^\mu\psi$. Therefore, the fermion kinetic term in the Lagrangian is gauge invariant as well. To construct a kinetic term for the gauge fields we introduce the field strength tensor

$$F^{\mu\nu} = \frac{i}{g}[D^\mu, D^\nu]. \quad (2.6)$$

which transforms like $F^{\mu\nu} \rightarrow UF^{\mu\nu}U^\dagger$. Therefore we are able to write down the gauge fields kinetic term as

$$\mathcal{L}_{gauge} = -\frac{1}{2}\text{Tr}(F_{\mu\nu}F^{\mu\nu}) \quad (2.7)$$

where the trace sums over the group indices. It turns out that this is the only possible term contributing to the Lagrangian. We can finally write down the Lagrangian for a gauge theory

$$\mathcal{L} = \mathcal{L}_{particle} + \mathcal{L}_{gauge} = \bar{\psi}(i\gamma^\mu D_\mu - m_\psi)\psi - \frac{1}{2}\text{Tr}(F_{\mu\nu}F^{\mu\nu}). \quad (2.8)$$

For the Standard model we have a field for each quark and lepton. The full symmetry group is $SU(3)_C \times SU(2)_L \times U(1)_Y$. The $SU(3)_C$ group only acts on quarks and describes the strong interaction. The corresponding gauge fields are called gluons. The $SU(2)_L \times U(1)_Y$ group describes the weak and electromagnetic interaction. The fourth fundamental force, gravity, is currently not described by the Standard Model. Its effect can be ignored in the context of particle physics. Furthermore the Standard model predicts the existence of the Higgs particle which is a spin-0 boson. All particles except the Higgs boson have been observed. While writing this thesis, both ATLAS and CMS reported an excess for a boson with mass $m = 125$ GeV that might correspond to the Higgs Boson [47, 48].

2.2 Electroweak interactions

From experiment we know that the charged weak interaction only acts on left-handed fermions. We introduce left-handed fields using the projection operator $P_L = \frac{1}{2}(1 - \gamma_5)$

$$\psi_L = P_L\psi = \frac{1}{2}(1 - \gamma_5)\psi \quad (2.9)$$

where $\gamma_5 = i\gamma_0\gamma_1\gamma_2\gamma_3$. The electroweak interaction is described by an $SU(2)_L$ group acting on doublets of left-handed fields and a $U(1)_Y$ group where Y denotes the hypercharge. The right handed fields are singlets under the $SU(3)$ group. Since the neutrino is electrically neutral it does not interact with anything and we will ignore its right handed field. Therefore we can write down the lepton fields

$$\begin{pmatrix} \nu_{eL} \\ e_L \end{pmatrix}, \begin{pmatrix} \nu_{\mu L} \\ \mu_L \end{pmatrix}, \begin{pmatrix} \nu_{\tau L} \\ \tau_L \end{pmatrix}, (e_R), (\mu_R), (\tau_R) \quad (2.10)$$

and the quark fields

$$\begin{pmatrix} u_L \\ d'_L \end{pmatrix}, \begin{pmatrix} c_L \\ s'_L \end{pmatrix}, \begin{pmatrix} t_L \\ b'_L \end{pmatrix}, (u_R), (d'_R), (c_R), (s'_R), (t_R), (b'_R). \quad (2.11)$$

The quark fields d' , s' and b' involved in the weak interaction are not the mass eigenstates. We can express them as a linear combination of mass eigenstates d , s and b using the CKM matrix.

$$\begin{pmatrix} d' \\ s' \\ b' \end{pmatrix} = \begin{pmatrix} V_{ud} & V_{us} & V_{ub} \\ V_{cd} & V_{cs} & V_{cb} \\ V_{td} & V_{ts} & V_{tb} \end{pmatrix} \begin{pmatrix} d \\ s \\ b \end{pmatrix} \quad (2.12)$$

The covariant derivative of the $SU(2)_L \times U(1)_Y$ group is

$$D_{L\mu} = \partial_\mu - igW_{\mu a}\tau^a - ig'YB_\mu \quad (2.13)$$

The gauge fields W_μ and B_μ correspond to the $SU(2)$ and $U(1)$ group. They have different coupling constants g and g' since the gauge groups commute with one another. For the generators of the $SU(2)$ group we use $\tau_a = \frac{1}{2}\sigma_a$ where σ_a are the Pauli matrices and Y is the hypercharge. Since the right handed particles are singlets under the $SU(2)$ group their covariant derivative is

$$D_{R\mu} = \partial_\mu - ig'YB_\mu. \quad (2.14)$$

The mass eigenstates for gauge bosons are

$$W^\pm = \frac{1}{\sqrt{2}}(W_\mu^1 \mp iW_\mu^2), \quad Z^0 = \frac{1}{\sqrt{g^2 + g'^2}}(gW_\mu^3 - g'B_\mu), \quad A_\mu = \frac{1}{\sqrt{g^2 + g'^2}}(g'W_\mu^3 + gB_\mu). \quad (2.15)$$

The fields W^\pm and Z^0 correspond to the charged and neutral weak gauge bosons and A is the electromagnetic field. Using these fields and $\tau^\pm = (\tau_1 \pm i\tau_2)$ we can express the covariant derivative for the left handed fermion fields as

$$D_{L\mu} = \partial_\mu - i\frac{g}{\sqrt{2}}(W_{\mu+}\tau^+ + W_{\mu-}\tau^-) - i\frac{1}{\sqrt{g^2 + g'^2}}Z_\mu^0(g^2\tau^3 - g'^2Y) - i\frac{gg'}{\sqrt{g^2 + g'^2}}A_\mu(\tau^3 + Y) \quad (2.16)$$

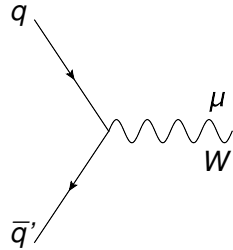
From this expression we can extract the form of the interaction between fermions and gauge bosons. We will concentrate on first generation quarks and charged gauge bosons W^\pm . Taking into account that left-handed quarks form a doublet Q_L we can write down the kinetic part for the Lagrangian as

$$\begin{aligned} \mathcal{L} &= i\bar{Q}_L \not{D}_L Q_L + i\bar{u}_R \not{D}_R u_R + i\bar{d}_R \not{D}_R d_R \\ &= i\bar{u}_R \not{\partial} u_R + i\bar{d}_R \not{\partial} d_R + i\begin{pmatrix} \bar{u}_L & \bar{d}'_L \end{pmatrix} \gamma^\mu \left[\partial_\mu - \frac{ig}{\sqrt{2}} \begin{pmatrix} 0 & W_\mu^+ \\ W_\mu^- & 0 \end{pmatrix} \right] \begin{pmatrix} u_L \\ d'_L \end{pmatrix} \\ &= i\bar{u} \not{\partial} u + i\bar{d} \not{\partial} d - \frac{ig}{\sqrt{2}}\bar{u}_L\gamma^\mu W_\mu^+ d'_L - \frac{ig}{\sqrt{2}}\bar{d}'_L\gamma^\mu W_\mu^- u_L. \end{aligned} \quad (2.17)$$

Using the projection operators with $\psi_L = P_L\psi$ and $\bar{\psi}_L = \bar{\psi}P_R$ and the relation $\gamma^\mu P_L = P_R\gamma^\mu$ we can write the interaction term as

$$\begin{aligned} \mathcal{L}_{int} &= -\frac{ig}{\sqrt{2}}\bar{u}_L\gamma^\mu W_\mu^+ d'_L = -\frac{ig}{\sqrt{2}}\bar{u}P_R\gamma^\mu W_\mu^+ P_L d' = -\frac{ig}{\sqrt{2}}\bar{u}\gamma^\mu W_\mu^+ P_L d' \\ &= -\frac{ig}{2\sqrt{2}}\bar{u}\gamma^\mu(1 - \gamma_5)d' W_\mu^+ = -\frac{ig}{2\sqrt{2}}\bar{u}\gamma^\mu(1 - \gamma_5)(V_{ud}d + V_{us}s + V_{ub}b) W_\mu^+. \end{aligned} \quad (2.18)$$

Now we can read off the charged-current weak interaction vertex:



$$= -\frac{ig}{2\sqrt{2}}\gamma^\mu(1 - \gamma_5)V_{qq'}.$$

Since left and right-handed fermions fields transform differently under the $SU(2)_L$ group it is not possible to write down mass terms in the Lagrangian. These mass terms and the mass terms for the gauge bosons appear as a result of electroweak symmetry breaking [42].

2.3 QCD

The theory describing the strong interaction is called Quantum Chromo Dynamics (QCD). It is described by an $SU(3)_C$ gauge group where C denotes color. The corresponding gauge bosons are gluons. This symmetry group acts on quarks only which are considered as color triplets

$$q = \begin{pmatrix} q_R \\ q_G \\ q_B \end{pmatrix}. \quad (2.19)$$

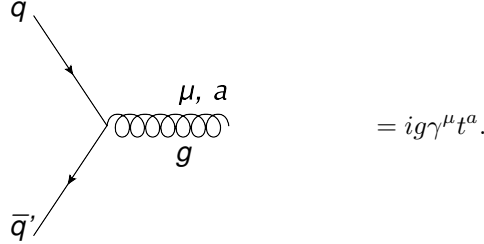
If we denote the generators of the $SU(3)_C$ group as t_a and the gluon fields as g_a^μ we can write down the covariant derivative as

$$D^\mu = \partial^\mu - ig_s G_a^\mu t^a. \quad (2.20)$$

The strong interactions coupling constant is g_s . Inserting this into the kinetic part of the quark Lagrangian gives

$$\mathcal{L}_{quark} = \bar{u}(i\gamma^\mu D_\mu - m)u = \bar{u}(i\gamma^\mu \partial_\mu - m)u + g_s G_{\mu a} t^a \bar{u}\gamma^\mu u \quad (2.21)$$

From this we can read off the quark gluon interaction vertex:



$$= ig\gamma^\mu t^a.$$

Since QCD is a non-abelian gauge theory more terms will appear in the QCD Lagrangian

$$\mathcal{L}_{QCD} = \mathcal{L}_{quark} + \mathcal{L}_{gauge} + \mathcal{L}_{gauge\ fixing} + \mathcal{L}_{ghost}. \quad (2.22)$$

The kinetic term for the gauge fields $\mathcal{L}_{gauge} = -\frac{1}{2}\text{Tr}(F_{\mu\nu}F^{\mu\nu})$ will contain the gluon kinetic part and additional gluon self-interactions. Since this term alone would not define the gluon propagator properly we have to introduce an additional gauge fixing term and ghost fields (see [42]).

2.4 Collider Phenomenology

LHC is a proton-proton collider which has a fixed center-of-mass energy. Since the protons have opposite momentum their center-of-mass frame is the laboratory frame. Each proton consists of partons which will be the initial state particles of the hard process. Since partons only carry a fraction of the protons momentum their center-of-mass energy frame will be boosted along the beam axis which we will choose to be the z -axis. Here we assume the initial state partons transverse momentum to be negligible. We need to find variables that respects the cylindrical symmetry of the detector and that are invariant under longitudinal boosts.

Therefore we can consider the projection of momenta onto the plane transverse to the beam axis. This transverse momentum \vec{p}_T vector can be parameterized using polar coordinates: the magnitude of the transverse momentum p_T and the azimuthal angle ϕ . Since we assume the initial state partons to have vanishing transverse momentum we expect the sum of the final state particles transverse momentum to vanish as well $\sum \vec{p}_T = 0$.

Both energy and longitudinal momentum transform in a complicated way under Lorentz boosts. It is more convenient to parameterize the longitudinal by the rapidity y and the particle mass m which is invariant by construction. Using a Lorentz boost from the rest frame of the particle along the beam axis we get [44]

$$\begin{pmatrix} E \\ p_L \end{pmatrix} = \exp \left[y \begin{pmatrix} 0 & 1 \\ 1 & 0 \end{pmatrix} \right] \begin{pmatrix} m \\ 0 \end{pmatrix} = m \begin{pmatrix} \cosh y \\ \sinh y \end{pmatrix} \quad (2.23)$$

Since the rapidity appears in an exponent we can simply add rapidities when performing different Lorentz boosts. The rapidity describing the boost from the particles rest frame to the LHC lab frame can be expressed in terms of the particles energy and momentum measured at LHC as

$$y = \frac{1}{2} \log \frac{E + p_L}{E - p_L}. \quad (2.24)$$

For massless particles we can use that $|\vec{p}| = E$ to get the expression

$$y = \frac{1}{2} \log \frac{E + p_L}{E - p_L} = \frac{1}{2} \log \frac{|\vec{p}| + p_L}{|\vec{p}| - p_L} = \frac{1}{2} \log \frac{1 + \cos \theta}{1 - \cos \theta} \equiv \eta. \quad (2.25)$$

Here we have introduced a new quantity, the pseudorapidity η . It only depends on the polar angle θ which can be easily measured at LHC. For massive particles rapidity and pseudorapidity are different and therefore pseudorapidity is not additive. At ATLAS and CMS we can observe pseudorapidities up to $\eta = 5$. Since both rapidity and azimuthal angle lie in the same range we define a distance measure for the detector

$$(\Delta R)^2 = (\Delta\eta)^2 + (\Delta\phi)^2. \quad (2.26)$$

At LHC we do not measure quarks and gluons that appear in the final state of the hard process. Due to color confinement they can not exist freely. These particles will hadronize before they can decay and form mesons and baryons. After further decay we will observe bunches of particles in the detector. They are highly boosted and not well separated. Narrow cones of such particles form jets. These will leave an energy deposit in the detector calorimeter cells which we finally observe. Assuming that each parton forms a jet the partons four-momentum should be described by the jets four-momentum. Therefore the term parton and jet is often used synonymously. We are left with the problem of reconstructing jets out of the calorimeter data. This is done by jet-algorithms. From QCD we know that partons emit soft and collinear radiation. This is described by the parton shower. The resulting particles will hadronize and cause an energy deposit in the detector. Therefore, a jet reconstruction algorithm has to decide if two subjets originated from the same parton. This is done based on a distance measure between two jets y_{ij} or between jet and beam axis y_{iB} . There are different jet algorithms available. We present the mostly used algorithms, the k_T , Cambridge-Aachen (C/A) and anti- k_T algorithms, following [44]. A detailed description can be found in [49].

k_T -algorithm: The k_T algorithm starts combining the soft constituents which have small transverse momentum p_T . The distance measures are

$$y_{ij} = \frac{\Delta R_{ij}}{R} \min(p_{T,i}, p_{T,j}) \quad y_{iB} = p_{T,i} \quad (2.27)$$

C/A-algorithm: The C/A recombines jets purely based on their geometrical distance. The distance measures are

$$y_{ij} = \frac{\Delta R_{ij}}{R} \quad y_{iB} = 1 \quad (2.28)$$

anti- k_T -algorithm: The anti- k_T algorithm starts combining the hard constituents which have large transverse momentum p_T . The distance measures are

$$y_{ij} = \frac{\Delta R_{ij}}{R} \min(p_{T,i}^{-1}, p_{T,j}^{-1}) \quad y_{iB} = p_{T,i}^{-1} \quad (2.29)$$

In all presented algorithms, ΔR_{ij} is the distance in R -space between two jets i and j . R describes the angular size of the jet. The algorithms start with the calorimeter cells four-momentum which form proto-jets. After defining a scale y_{cut} the algorithm proceeds as follows:

- For all proto-jets in the event, find combinations of two proto-jets i and j with the minimal distance $y_{min} = \min_{ij}(y_{ij}, y_{iB})$
- If two proto-jets i and j are close enough $y_{min} = y_{ij} < y_{cut}$ merge their momenta and go back to the first step
- If there is a proto-jet i close enough to the beam $y_{min} = y_{iB} < y_{cut}$ call it beam radiation and therefore remove it and go back to the first step
- If all proto-jets are well separated from each other and the beam axis $y_{min} > y_{cut}$ keep all jets and stop

In the case of the k_T and C/A algorithm the clustering history should be similar to the branching history and therefore has a physical meaning.

If we want to reconstruct heavy particles, like top quarks or Higgs bosons, we expect the corresponding jet to have a large geometrical size. Such jets are called fat jets. Due to the large jet-size we expect to see subjets inside the fat jet that correspond to the decay products of the heavy

particle. Therefore the k_T and C/A algorithm will work best since their clustering history has a physical meaning.

Due to its large size, the fat jet may also include QCD radiation. Such contribution could contaminate the momentum of the reconstructed fat jet, and hence we would like to avoid this. We distinguish different sources of QCD radiation

final state radiation (FSR): As mentioned before final state partons will emit soft and collinear radiation which is called final state radiation. This radiation we would like to collect since it contains momentum contributions needed to reconstruct the fat jet.

initial state radiation (ISR): The initial state partons may radiate. This so called initial state radiation we would like to remove during reclustering.

underlying event (UE): In a proton-proton interaction there could also be an interaction of the proton remnants which do not participate in the hard process. Activity coming from such events is called the underlying event. The amount of radiation in a fat jet coming from UE depends on its jetsize. The effect on the jet mass can be described by [50]

$$\langle \delta m_j^2 \rangle \simeq \Lambda_{UE} p_{T,j} \left(\frac{R^4}{4} + \frac{R^8}{4608} + \mathcal{O}(R^{12}) \right) \quad (2.30)$$

where at LHC Λ_{UE} is expected to be about $\mathcal{O}(10)$ GeV [51]. To lower the contributions from UE we have to reduce the area of the fat jet used for its reconstruction. This can be done using filtering algorithms.

pile up: Since the beam does not consist of single protons but bunches of protons there can be multiple collisions within one beam crossing. Again we would like to remove this contribution by applying filtering methods.

Up to now we have only considered problems appearing during the event reconstruction. Another problem we have to face is that we do not only detect the signal but also the background. Here the signal is the process we want to detect. With background we mean uninteresting Standard Model or QCD events that unfortunately look like our signal.

We want to predict the number of signal and background events that we expect to be measured for each process. This number N_{event} can be expressed as

$$N_{event} = \sigma_{event} \cdot \mathcal{L} \quad (2.31)$$

where σ_{event} is the cross section for the specific event measured in fb . The luminosity \mathcal{L} is a collider specific number describing the number of particles crossing a unit area which is measured in fb^{-1} . In 2011 the LHC has reached an integrated luminosity of around $5fb^{-1}$ at $\sqrt{s} = 7$ TeV and for the 2012 run we expect a luminosity of $10fb^{-1}$ at $\sqrt{s} = 8$ TeV [52].

In order to clearly measure the signal process we would like to have a good signal S over background B ratio

$$\frac{S}{B} > 1 \quad (2.32)$$

Furthermore we have to make sure that the signal we observe is not just a fluctuation of the background. The high-energy-physics community agreed that for discovery we need to have a five sigma excess over the background. This implies that we require

$$\frac{S}{\sqrt{B}} > 5. \quad (2.33)$$

Chapter 3

Top Physics

3.1 Properties of the top quark

In our analysis we will focus on one Standard Model particle, the top quark. It was postulated in 1973 by Kobayashi and Maskawa [53] and observed for the first time by CDF and D0 [54, 55] in 1995. The top quark has a mass of 173.5 ± 1.4 GeV [56] and is therefore the most massive Standard Model particle. Due to its large mass it is a window to new physics as it couples strongly to the Higgs sector and top partners are likely to decay into top quarks [15, 57]. Furthermore the Tevatron has left some open questions about the top forward-backward asymmetry [58, 59] and the ratio of s -channel and t -channel single top cross sections [21]. These results could also be a hint for new physics.

Due to its high mass the top has a short lifetime of $4 \cdot 10^{-25}$ seconds [56]. This is much faster than typical timescales for strong interactions. Therefore it will decay before hadronization. No other quark has this property. This gives us a unique possibility to probe the behavior of an unbound quark. To make use of this advantage we need a large top quark cross section. Compared with older colliders, the top quark will be copiously produced at the LHC. Most top quarks are produced in pairs via the strong interaction $p + p \rightarrow t + \bar{t}$. The dominant subprocesses of quark annihilation ($q + \bar{q} \rightarrow t + \bar{t}$) and gluon-gluon fusion ($g + g \rightarrow t + \bar{t}$) are shown in Fig. 3.1. At the LHC gluon-gluon fusion is the dominant subprocess. The $t\bar{t}$ cross section rises from $\sigma_{t\bar{t}}^{\text{Tevatron}} = 7.08$ pb at Tevatron to $\sigma_{t\bar{t}}^{7\text{TeV}} = 163$ pb at LHC 7 TeV and $\sigma_{t\bar{t}}^{14\text{TeV}} = 920$ pb at LHC 14 TeV [60].

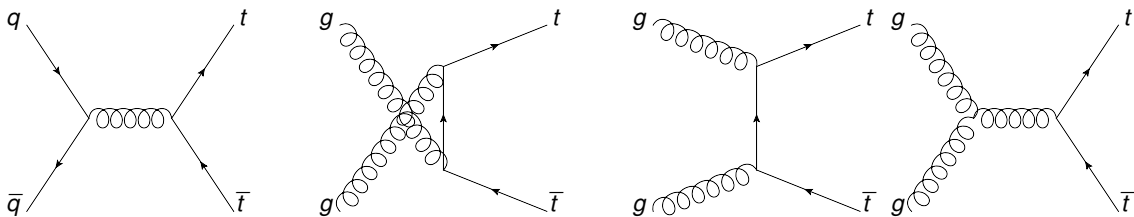


Figure 3.1: $t\bar{t}$ production via quark annihilation and gluon-gluon fusion.

To detect the top quark we need to know its decay behavior. The Standard model predicts that the top quark will decay into a W -boson and a quark q which could in principle be any d -like quark. The corresponding decay rate Γ is proportional to the squared CKM-matrix element $|V_{tq}|^2$. According to the PDG [56] the branching ratio $W \rightarrow b$ versus $W \rightarrow q$ is

$$\frac{\Gamma(t \rightarrow Wb)}{\Gamma(t \rightarrow Wq)} = \frac{|V_{tb}|^2}{|V_{td}|^2 + |V_{ts}|^2 + |V_{tb}|^2} = 0.99. \quad (3.1)$$

We see that the dominant decay mode is $t \rightarrow Wb$. Of course this does not tell us that $|V_{tb}| \approx 1$ unless we assume unitarity of the CKM matrix. To prove unitarity of the CKM matrix we would have to measure V_{tb} . This is possible by measuring single top production as we will see later. If it would turn out that the CKM matrix is not unitary assuming three generations of quarks this would be a hint towards a 4th generation. For analysis we will assume three generations and therefore have a branching ratio $BR(t \rightarrow tW) = 99\%$.

The b -quark will hadronize and form a jet which we can observe. The W -boson will further decay either into leptons or quarks. For the leptonic decay $W \rightarrow l + \nu_l$ all three generations are allowed $l = e, \mu, \tau$. For the hadronic decays the W -decay rate is proportional to $|V_{qq'}|$. Decays into tops are not allowed due to its high mass. For the allowed hadronic decays we have to take into account the three color states of the quarks. Therefore we get an approximate branching ratio

$$\frac{\Gamma(W \rightarrow l + \nu_l)}{\Gamma(W \rightarrow q + \bar{q})} = \frac{3}{3 \cdot (|V_{ud}|^2 + |V_{us}|^2 + |V_{cd}|^2 + |V_{cs}|^2)} = 0.50 \quad (3.2)$$

where we have used the PDG results for the CKM matrix [61]. Using this number we can calculate the branching ratios.

$$\begin{aligned} BR(t \rightarrow b + q + \bar{q}') &= 66.7\% \\ BR(t \rightarrow b + \bar{l} + \nu_l) &= 33.3\% \end{aligned} \quad (3.3)$$

Each lepton flavour e, μ, τ has equal probability to appear as decay product.

Since the top quark decays before hadronization we have a chance to probe the parity-violating structure of the tbW -coupling. In the Standard Model, a W -bosons emitted in top decay have a specific distribution of helicity states. These can be easily understood in the top quark rest frame as shown in Fig. 3.2.

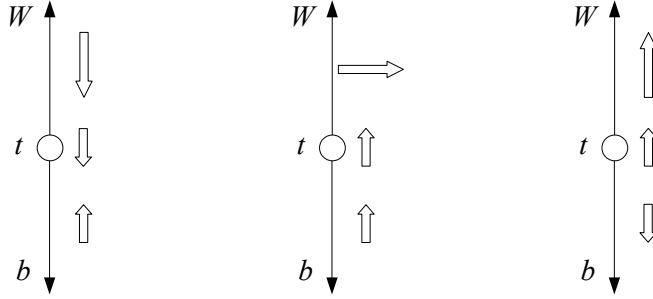


Figure 3.2: Top decay with left-handed (left), longitudinal (center) and right-handed (right) W -boson. Figure based on [62].

If we assume the b -quark to be massless it will always have a left-handed helicity due to the chirality of the tbW -vertex. If the b -quark is emitted parallel to top quark spin axis (left panel) its spin has to point in the opposite direction. Due to conservation of angular momentum the spin of the W -boson and its direction of motion are also anti-parallel. Therefore the W -boson is in the left-handed state. If the b -quark is emitted in the opposite direction of the top quark spin (central panel) their spin directions are parallel. Therefore, the projection of the spin of the W -boson has to be zero due to conservation of angular momentum which means that it is longitudinal polarized. The right panel shows the right-handed helicity state for the W -boson which is suppressed due to the small mass of the b -quark relative to its energy.

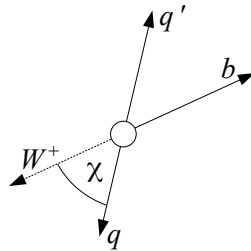


Figure 3.3: Definition of the decay angle χ between the opposite b -quark direction and the direction of the quark q in the W rest frame. Figure based on [62].

Different helicity states of the W -boson lead to different distributions for the decay angle χ of the quark q measured in the W -rest frame as shown in Fig. 3.3. For the left-handed helicity state, in

which the W -boson is emitted antiparallel to the top spin axis, the normalized differential cross section shows an characteristic behavior [62]

$$\frac{1}{\sigma} \frac{d\sigma}{d\cos\chi} \sim \frac{1}{2}(1 - \cos\chi)^2. \quad (3.4)$$

If the W -boson is emitted along the top spin axis and therefore longitudinal polarized, the normalized differential cross section behaves as

$$\frac{1}{\sigma} \frac{d\sigma}{d\cos\chi} \sim \sin^2\chi. \quad (3.5)$$

These distribution only describe the special cases in which the W -boson is emitted parallel or antiparallel to the top spin axis. If we take into account all possible decay angles between the W -boson and the top quark and all top spin states, the distribution for the differential cross section with respect to quark decay angle χ in the W -rest frame becomes

$$\frac{1}{\sigma} \frac{d\sigma}{d\cos\chi} = \frac{3}{4} \frac{m_t^2 \sin^2\chi + 2m_W^2 \frac{1}{2}(1 - \cos\chi)^2}{m_t^2 + 2m_W^2} = a_{long} \sin^2\chi + a_{left} \frac{1}{2}(1 - \cos\chi)^2. \quad (3.6)$$

We still see the different terms for the decay behavior of left-handed and longitudinal polarized W -bosons. We can read off the ratio between the two polarization states as $a_{left}/a_{long} = 2m_W^2/m_t^2$. This has been verified experimentally [11, 63].

The helicity structure of top decay can also be used in top tagging as implemented in the Johns Hopkins tagger [25]. In principle we are unable to distinguish the quarks produced in W -decay. Therefore we expect to see an almost uniform distribution for the decay angle χ using one (for instance the lower p_T) quark. This behavior will stay similar using the information of the reconstructed top. Light quarks or gluons that might mimic a top quark prefer to emit collinear jets. If we define χ similar the case of top decay based on the reconstructed top information we expect a behavior

$$\frac{1}{\sigma} \frac{d\sigma}{d\cos\chi} \sim \frac{1}{1 - \cos\chi} \quad (3.7)$$

describing the collinear radiation. This leads to a peak for small χ which can be rejected to distinguish the top signal from background events.

3.2 HEPTopTagger

If the top decays leptonically we will observe a b-jet and a lepton plus missing energy [64]. The neutrino will be undetected, which causes the inferred missing transverse momentum $p_{T,miss}$. Normally it is assumed that the transverse momentum of the neutrino is described by this missing transverse momentum. The longitudinal neutrino momentum can be determined using the assumption that the invariant mass of the neutrino and lepton should be the W -mass m_W . From this picture the top momentum can be reconstructed. Of course this strategy is limited. Events in which more than one particle causes contributions to the missing momentum are difficult to reconstruct. This happens in fully leptonic $t\bar{t}$ decay in which there are two neutrinos, or stop pair decay in which there are two neutralinos. Furthermore, this technique can not be used for hadronically decaying tops.

If the top decays hadronically we will observe its decay products in the form of an accumulation of jets concentrated in a certain region of the detector. These jets we want to analyze and identify as top decay products. An algorithm that finds top quarks inside accumulations of jets is called a top tagger. Compared with other top taggers, like the John-Hopkins Tagger [25] or the Thaler-Wang Tagger [23], which focus on highly boosted tops, we want to tag moderately boosted tops. Highly boosted tops have a very large transverse momentum $p_{T,top} > 800$ GeV and are expected to appear as decay products of heavy particles [57]. For tagging standard model tops this transverse momentum region is not sufficient enough. Therefore our tagger, the HEPTopTagger, is designed to find tops with transverse momentum $p_{T,top} > 200$ GeV. A summary about different top taggers can be found in [28]. In this section we describe the tagging algorithm as presented in [37].

1. **define fat jet using C/A algorithm with $R = 1.5$:** First we need to define the region of the calorimeter which we want to use as input for the HEPTopTagger. We will choose a fat jet based on the Cambridge/Aachen algorithm. The jetsize R should be similar to the typical size of a decaying top with $p_T = 200$ GeV. To define this size we employ the following procedure [65, 66, 67]. From the top decay products in parton level we first identify the two top decay products (i, j) that have the smallest distance $\Delta R_{i,j}$ from each other. We combine these two particle momenta p_i, p_j and calculate the distance $\Delta R_{ij,k}$ between the resulting momentum $p_{ij} = p_i + p_j$ and the third decay product k . The size of the decayed top can be approximated by the larger one of these two distances in R -space $R_{top} = \max(\Delta R_{i,j}, \Delta R_{ij,k})$. The two dimensional correlation between the size of the top R_{top} and its transverse momentum p_T is shown in Fig. 3.4. We can see that the decay products are well separated for low p_T tops. If we want to detect tops with $p_T \approx 200$ GeV we need to look at large fat jets with $R = 1.5$. If we would choose an even larger R we could in principle detect tops with smaller transverse momentum. However, we would risk a crossover between different tops or other jets. This would contaminate the tagging result and would lead to poorly reconstructed or mis-tagged tops. Therefore we require a fat jet using the C/A algorithm with $R = 1.5$ and $p_T^{fat} > 200$ GeV.

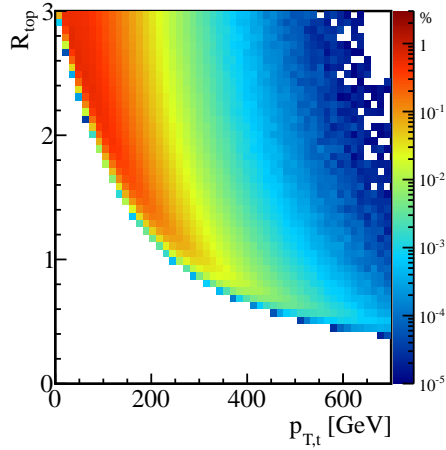


Figure 3.4: Size of the top R_{top} vs. p_T distribution for a sample of top quarks from $t\bar{t}$ production. Figure based on [37].

2. **find hard subjects inside each fat jet:** We have seen that the top decay products are well separated. Therefore it will be possible to identify the subjects corresponding to the decay products. Unfortunately the fat jet does not only include the top decay products and their final state radiation but also QCD effects like initial state radiation, underlying events or pile up. These impurities we want to reject. To find the subjects we will undo the last clustering step using a mass drop criterion [68, 25]. Let us therefore consider a jet j that decays into two subjects j_1 and j_2 where we assume j_1 to have a larger mass $m_{j_1} > m_{j_2}$. If j corresponds to a massive particles we expect it to decay into two jets with small masses $m_j \gg m_{j_1}, m_{j_2}$. If j_2 corresponds to a QCD jet we expect it to leave the massive jets mass almost unchanged while clustering $m_j \approx m_{j_1} \gg m_{j_2}$. Therefore we require $m_{j_1} < 0.8 m_j$ to keep both jets j_1 and j_2 . If this criterion is not fulfilled we will keep only j_1 . Jets are further decomposed until they drop under a mass $m_j < 50$ GeV.
3. **filtering of the subjects:** If we look at the hard subjects, its size is large enough to contain also QCD radiation. Initial state radiation, underlying events and pile up may contaminate the subject recombination. To avoid this we will use filtering [68]. We recombine the hard subjects using C/A algorithm with small resolution

$$R_{filter} = \min(0.3, \Delta R_{jk}/2) \quad (3.8)$$

where ΔR_{jk} is the distance between the subject and its closest neighbor subject. This reduces the effective fraction of the fat jet area we are actually using for the reconstruction of the

top mass. We will keep the five hardest filtered subjects for the next analysis steps. This procedure is illustrated in Fig. 3.5

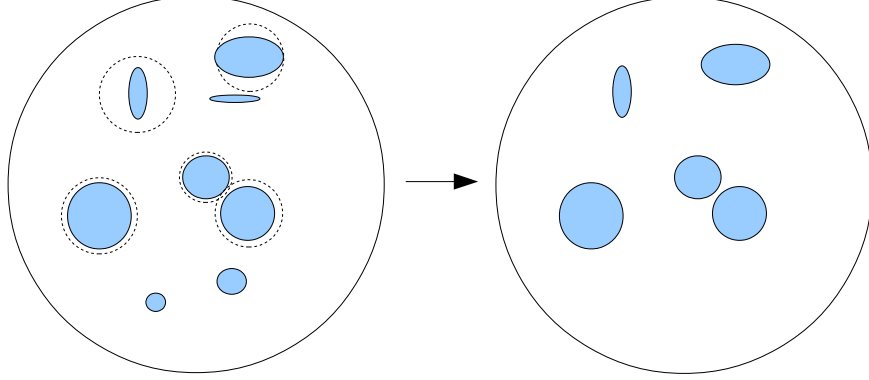


Figure 3.5: Fat jet and hard subjects before (left) and after (right) filtering. The dotted circles have a size R_{filter} .

4. **find top candidates:** We say that a fat jet is considered as a top candidate if we can find three filtered subjects that have a combined jet mass close to the top mass m_t . To find these three subjects, we iterate through all pairings of three subjects and choose the combination that gives a combined mass m_{fat} closest to m_t . If this mass lies inside the top mass window $150 \text{ GeV} < m_{fat} < 200 \text{ GeV}$ we call this fat jet a top candidate.
5. **mass plane cut:** Up to now we have used that the combined mass m_{123} of the three (p_T ordered) subjects j_1, j_2, j_3 should be close to the top mass m_t . Furthermore we know that two of these jets j_i and j_j should be W -decay products. Therefore their di-jet mass m_{ij} should be close to the W -mass m_W . If we assume all jets to be massless $p_i^2 = 0$ the top mass constraint can be expressed in terms of di-jet masses:

$$m_t^2 = m_{123}^2 = (p_1 + p_2 + p_3)^2 = (p_1 + p_2)^2 + (p_1 + p_3)^2 + (p_2 + p_3)^2 = m_{12}^2 + m_{13}^2 + m_{23}^2. \quad (3.9)$$

This is the equation of the surface of a sphere in m_{ij} -space with radius m_t . We have already fixed m_{123} to lie inside the top mass window. Therefore there are two variables left for a full description of the decay kinematics. We choose m_{23}/m_{123} and $\arctan m_{13}/m_{12}$ which would correspond to the spherical coordinates θ and ϕ in m_{ij} -space. For the W -mass constraint will require $R_{min} = 0.85 \cdot m_W/m_t < m_{ij}/m_{123} < 1.15 \cdot m_W/m_t = R_{max}$ for at least one combination of subjects (i, j) . Using the relation between mass ratios

$$1 = \left(\frac{m_{12}}{m_{123}}\right)^2 \left(1 + \left(\frac{m_{13}}{m_{12}}\right)^2\right) + \left(\frac{m_{23}}{m_{123}}\right)^2 \quad (3.10)$$

we can reformulate this constraint. The subjects need to fulfill at least one of the following criteria:

$$\begin{aligned} \text{Case 1: } & R_{min} < \frac{m_{23}}{m_{123}} < R_{max} \\ \text{Case 2: } & R_{min}^2 \left(1 + \left(\frac{m_{13}}{m_{12}}\right)^2\right) < 1 - \left(\frac{m_{23}}{m_{123}}\right)^2 < R_{max}^2 \left(1 + \left(\frac{m_{13}}{m_{12}}\right)^2\right) \\ \text{Case 3: } & R_{min}^2 \left(1 + \left(\frac{m_{12}}{m_{13}}\right)^2\right) < 1 - \left(\frac{m_{23}}{m_{123}}\right)^2 < R_{max}^2 \left(1 + \left(\frac{m_{12}}{m_{13}}\right)^2\right) \end{aligned} \quad (3.11)$$

The two dimensional correlation between the two mass plane variables is shown in Fig. 3.6. Indeed we see that for events including a top the di-jet masses cluster in the expected area of the mass plane. Up to now we have only used two constraints. We can choose

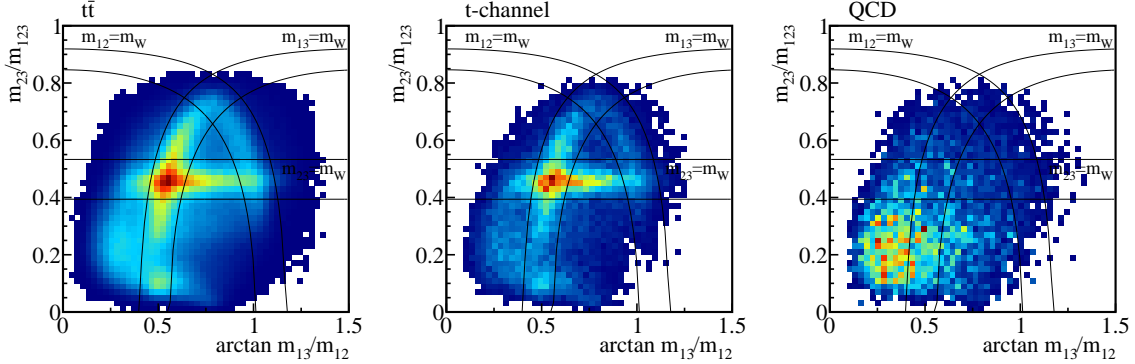


Figure 3.6: Distribution of $t\bar{t}$ (left), t -channel (center) and QCD (right) events in $\arctan m_{13}/m_{12}$ vs. m_{23}/m_{123} plane. The lines denote the area allowed by W -mass condition. Dense region is shown in red. Figure based on [37].

a third constraint to reduce the background coming from QCD. Since background events cluster at low m_{23} and low ratios m_{13}/m_{12} we can cut off this region. For case 1 we require $0.2 < \arctan \frac{m_{13}}{m_{12}} < 1.3$ and for the other cases $\frac{m_{23}}{m_{123}} > 0.35$.

6. **p_T -cut on filtered subjects:** Finally the three filtered subjects need to have a combined transverse momentum $p_T > 200$ GeV.

After tagging we can label the subjects as b , W_1 and W_2 subjects. The labeling is chosen such that m_W is reconstructed best by the subjects W_1 and W_2 . We can further decrease the number of mis-tagged tops coming from QCD or W +jets events using b -tagging. We assume a tagging rate ϵ_b and a mis-tag rate ϵ_{mis} for light quarks and gluon jets. As mentioned in [39] the most promising strategy is to perform one b -tag inside the b labeled subject. This decreases the background rate by a factor of ϵ_{mis} and the signal rate by a $\epsilon_{id} \cdot \epsilon_b$. Here ϵ_{id} denotes the probability of a correct assignment of the b -labeled subject which is about 70% for signal events (see Analysis).

If we would perform b -tags in all subjects to use this information during the tagging algorithm we would have to deal with a mis-tagging efficiency of $3 \cdot \epsilon_{mis}$. This can not be compensated by improvement in the mass plane cuts or for ϵ_{id} .

Besides the filtered mass we used in the tagging algorithm, the HEPTopTagger also provides the pruned [69, 70, 71, 72] and unfiltered mass [39]. These variables show a different behavior for signal and background events as we will discuss later.

3.3 Single Top production

Beside top pair production the Standard Model also predicts the production of single top quarks via the weak interaction. At leading order there are three subprocesses: t -channel, s -channel and Wt -associated single top production.

$$\begin{aligned}
 t\text{-channel:} &= q + b \rightarrow q' + t \\
 s\text{-channel:} &= q + \bar{q}' \rightarrow \bar{b} + t \\
 Wt\text{-associated:} &= b + g \rightarrow W + t
 \end{aligned} \tag{3.12}$$

The corresponding Feynman diagrams are shown in Fig. 3.7. To understand angular correlations we calculate the differential cross section of the t -channel and s -channel single top production. Let us do this calculation for the t -channel first. We will only look at the process $u + b \rightarrow d + t$ since this is the biggest contribution. Feynman diagrams with antiquarks or charm quarks instead of an up quark are suppressed by their parton distribution function. Diagrams with a d or s instead of a b are suppressed by their value of the CKM matrix $|V_{td}|$ and $|V_{ts}|$.

For this process we can write the matrix element as

$$-i\mathcal{M} = \left[\bar{u}_t \frac{ig_w}{2\sqrt{2}} \gamma^\mu (1 - \gamma_5) V_{tb} u_b \right] \left[\frac{-ig_{\mu\nu}}{k^2 - m_w^2} \right] \left[\bar{u}_d \frac{ig_w}{2\sqrt{2}} \gamma^\nu (1 - \gamma_5) V_{ud} u_u \right] \tag{3.13}$$

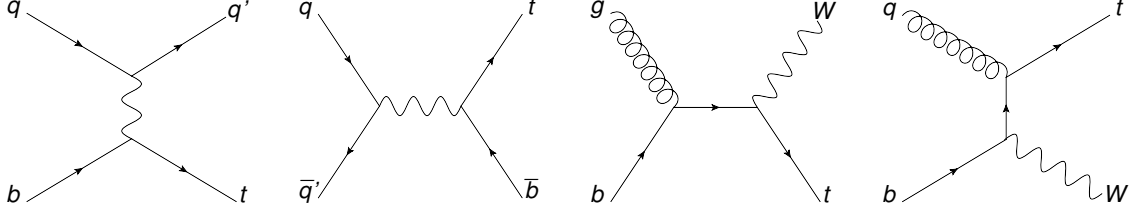


Figure 3.7: Feynman Diagram of the t -channel (left), s -channel (center left) and Wt -associated (right) single top production.

where $k = p_b - p_t$. Then the squared matrix element averaged over initial spins and summed over final spins becomes

$$\begin{aligned}
 |\mathcal{M}|^2 &= \frac{1}{4} \sum_{\text{all spins}} \frac{g_w^4 |V_{ud}|^2 |V_{tb}|^2}{64} \left| [\bar{u}_t \gamma^\mu (1 - \gamma_5) u_b] \left[\frac{g_{\mu\nu}}{k^2 - m_w^2} \right] [\bar{u}_d \gamma^\nu (1 - \gamma_5) u_u] \right|^2 \\
 &= \frac{1}{256} g_w^4 |V_{ud}|^2 |V_{tb}|^2 X^{\mu\kappa} Y_{\mu\kappa\nu\lambda} Z^{\nu\lambda}
 \end{aligned} \tag{3.14}$$

Here we have introduced the three tensors $X^{\mu\kappa}$, $Y_{\mu\kappa\nu\lambda}$ and $Z^{\nu\lambda}$. At first we realize that we can write the complex conjugate as

$$\begin{aligned}
 [\bar{u}_t \gamma^\kappa (1 - \gamma_5) u_b]^* &= [\bar{u}_t \gamma^\kappa (1 - \gamma_5) u_b]^\dagger = u_b^\dagger (1 - \gamma_5) \gamma^{\dagger\kappa} \gamma^0 u_t \\
 &= u_b^\dagger \gamma^0 (1 + \gamma_5) \gamma^\kappa u_t = \bar{u}_b \gamma^\kappa (1 - \gamma_5) u_t
 \end{aligned} \tag{3.15}$$

Using this relation and the completeness relations we can write the tensor $X^{\mu\kappa}$ as

$$\begin{aligned}
 X^{\mu\kappa} &= \sum_{\text{spin } b,t} [\bar{u}_t \gamma^\mu (1 - \gamma_5) u_b] [\bar{u}_t \gamma^\kappa (1 - \gamma_5) u_b]^* \\
 &= \sum_{\text{spin } b,t} [\bar{u}_t \gamma^\mu (1 - \gamma_5) u_b] [\bar{u}_b \gamma^\kappa (1 - \gamma_5) u_t] \\
 &= \text{Tr} [(\not{p}_t + m_t) \gamma^\mu (1 - \gamma_5) (\not{p}_b) \gamma^\kappa (1 - \gamma_5)] \\
 &= 2 \text{Tr} [(\not{p}_t + m_t) \gamma^\mu (\not{p}_b) \gamma^\kappa (1 - \gamma_5)] \\
 &= 2 p_{t\alpha} p_{b\beta} \text{Tr} [\gamma^\alpha \gamma^\mu \gamma^\beta \gamma^\kappa (1 - \gamma_5)] + 2 m_t p_{b\beta} \text{Tr} [\gamma^\mu \gamma^\beta \gamma^\kappa (1 - \gamma_5)] \\
 &= 2 p_{t\alpha} p_{b\beta} \text{Tr} [\gamma^\alpha \gamma^\mu \gamma^\beta \gamma^\kappa (1 - \gamma_5)] \\
 &= 8 p_{t\alpha} p_{b\beta} (g^{\alpha\mu} g^{\beta\kappa} - g^{\alpha\beta} g^{\mu\kappa} + g^{\alpha\kappa} g^{\mu\beta} + i \epsilon^{\alpha\mu\beta\kappa}) \\
 &= 8 (p_t^\mu p_b^\kappa - p_t \cdot p_b \cdot g^{\mu\kappa} + p_t^\kappa p_b^\mu + i p_{t\alpha} p_{b\beta} \epsilon^{\alpha\mu\beta\kappa})
 \end{aligned} \tag{3.16}$$

In the second line we used the formula for the complex conjugate that we derived before. In the third line we used the completeness relations. In the fourth line we commuted γ_5 twice and used $(1 - \gamma_5)^2 = 2(1 - \gamma_5)$. In the fifth line we split the right hand side into two traces and used $\not{p} = \gamma^\alpha p_\alpha$. In the next step we used that any trace of an odd number of γ^α 's vanishes. In the eighth line we use the expression for the traces and in the last line we evaluated that expression. Similarly we get

$$\begin{aligned}
 Z^{\nu\lambda} &= \sum_{\text{spin } u,d} [\bar{u}_d \gamma^\nu (1 - \gamma_5) u_u] [\bar{u}_d \gamma^\lambda (1 - \gamma_5) u_u]^* \\
 &= \sum_{\text{spin } u,d} [\bar{u}_d \gamma^\nu (1 - \gamma_5) u_u] [\bar{u}_u \gamma^\lambda (1 - \gamma_5) u_d] \\
 &= \text{Tr} [(\not{p}_d) \gamma^\nu (1 - \gamma_5) (\not{p}_u) \gamma^\lambda (1 - \gamma_5)] \\
 &= 8 (p_d^\nu p_u^\lambda - p_d \cdot p_u \cdot g^{\nu\lambda} + p_d^\lambda p_u^\nu + i p_{d\alpha} p_{u\beta} \epsilon^{\alpha\nu\beta\lambda})
 \end{aligned} \tag{3.17}$$

and

$$Y_{\mu\kappa\nu\lambda} = \frac{g_{\mu\nu} g_{\kappa\lambda}}{(k^2 - m_W^2)^2} \tag{3.18}$$

Putting everything together we get

$$\begin{aligned}
|\mathcal{M}|^2 &= \frac{1}{256} g_w^4 |V_{ud}|^2 |V_{tb}|^2 X^{\mu\kappa} Y_{\mu\kappa\nu\lambda} Z^{\nu\lambda} \\
&= \frac{64}{256} g_w^4 |V_{ud}|^2 |V_{tb}|^2 (p_t^\mu p_b^\kappa - (p_t \cdot p_b) g^{\mu\kappa} + p_t^\kappa p_b^\mu + i p_{t\alpha} p_{b\beta} \epsilon^{\alpha\mu\beta\kappa}) \\
&\quad \cdot \frac{g_{\mu\nu} g_{\kappa\lambda}}{(k^2 - m_W^2)^2} (p_d^\nu p_u^\lambda - (p_d \cdot p_u) g^{\nu\lambda} + p_d^\lambda p_u^\nu + i p_{d\alpha'} p_{u\beta'} \epsilon^{\alpha'\nu\beta'\lambda}) \\
&= \frac{1}{4} g_w^4 |V_{ud}|^2 |V_{tb}|^2 \frac{1}{(k^2 - m_W^2)^2} \{ (p_t \cdot p_d)(p_b \cdot p_u) \\
&\quad - (p_t \cdot p_b)(p_d \cdot p_u) + (p_t \cdot p_u)(p_b \cdot p_d) - (p_t \cdot p_b)(p_d \cdot p_u) + 4(p_t \cdot p_b)(p_d \cdot p_u) \\
&\quad - (p_t \cdot p_b)(p_d \cdot p_u) + (p_t \cdot p_u)(p_b \cdot p_d) - (p_t \cdot p_b)(p_d \cdot p_u) + (p_t \cdot p_d)(p_b \cdot p_u) \\
&\quad + i p_{t\alpha} p_{b\beta} \epsilon^{\alpha\mu\beta\kappa} (p_{d\mu} p_{u\kappa} + p_{d\kappa} p_{u\mu}) + i p_{d\alpha'} p_{u\beta'} \epsilon^{\alpha'\nu\beta'\lambda} (p_{t\nu} p_{b\lambda} + p_{t\lambda} p_{b\nu}) \\
&\quad - i p_{t\alpha} p_{b\beta} \epsilon_{\nu\lambda}^{\alpha\beta} g^{\nu\lambda} (p_d \cdot p_u) - i p_{d\alpha'} p_{u\beta'} \epsilon_{\mu\kappa}^{\alpha'\beta'} g^{\mu\kappa} (p_t \cdot p_b) \\
&\quad + i^2 p_{t\alpha} p_{b\beta} p_d^{\alpha'} p_u^{\beta'} \epsilon^{\alpha\mu\beta\kappa} \epsilon_{\alpha'\mu\beta'\kappa} \} \\
&= \frac{1}{4} g_w^4 |V_{ud}|^2 |V_{tb}|^2 \frac{1}{(k^2 - m_W^2)^2} \{ 2(p_t \cdot p_d)(p_b \cdot p_u) + 2(p_t \cdot p_u)(p_b \cdot p_d) \\
&\quad - p_{t\alpha} p_{b\beta} p_d^{\alpha'} p_u^{\beta'} (-2)(\delta_{\alpha'}^\alpha \delta_{\beta'}^\beta - \delta_{\beta'}^\alpha \delta_{\alpha'}^\beta) \} \\
&= \frac{1}{4} g_w^4 |V_{ud}|^2 |V_{tb}|^2 \frac{1}{(k^2 - m_W^2)^2} \{ 2(p_t \cdot p_d)(p_b \cdot p_u) + 2(p_t \cdot p_u)(p_b \cdot p_d) \\
&\quad + 2(p_t \cdot p_d)(p_b \cdot p_u) - 2(p_t \cdot p_u)(p_b \cdot p_d) \} \\
&= \frac{1}{4} g_w^4 |V_{ud}|^2 |V_{tb}|^2 \frac{(2p_t \cdot p_d)(2p_b \cdot p_u)}{(k^2 - m_W^2)^2}
\end{aligned} \tag{3.19}$$

We can use this squared matrix element to calculate the differential cross section

$$\frac{d\sigma}{d\cos\theta} = \frac{1}{32\pi s} \frac{|p_t|}{p_b} |\mathcal{M}|^2 \tag{3.20}$$

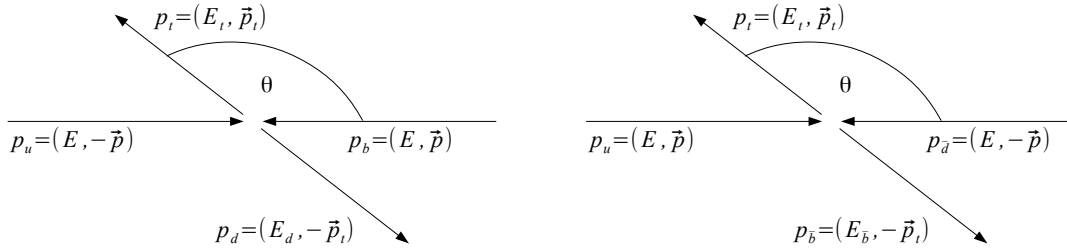


Figure 3.8: Kinematics of the s -channel (left) and t -channel (right) single top production

Let us first calculate the kinematic variables in the center-of-mass frame. We can parameterize the momenta as $p_b = (E, \vec{p})$, $p_u = (E, -\vec{p})$, $p_t = (E_t, \vec{p}_t)$ and $p_d = (E_d, -\vec{p}_t)$ where $|\vec{p}| = E$, $|\vec{p}_t| = E_d$ and $|\vec{p}_t|^2 + m_t^2 = E_t^2$. We know from energy conservation that

$$(E_t + E_d)^2 = (2E)^2 = s \tag{3.21}$$

where s is the squared center of mass energy. Therefore we can express E_t as

$$E_t^2 = |\vec{p}_t|^2 + m_t^2 = E_d + m_t^2 = (2E - E_t)^2 + m_t^2 = s - 2\sqrt{s}E_t + E_t^2 + m_t^2. \tag{3.22}$$

Solving this equation gives an expression for E_t :

$$E_t = \frac{s + m_t^2}{2\sqrt{s}} \quad (3.23)$$

Similarly we get

$$|\vec{p}_t| = \frac{s - m_t^2}{2\sqrt{s}} \quad (3.24)$$

Using this equation we can calculate the product of the momentum 4-vectors

$$\begin{aligned} 2p_b p_u &= (p_b + p_u)^2 = 4E^2 = s \\ 2p_t p_d &= (p_t + p_d)^2 - m_t^2 = 4E^2 - m_t^2 = s - m_t^2 \\ k^2 &= (p_b - p_t)^2 = m_t^2 - 2p_b p_t = m_t^2 - 2[E E_t + |\vec{p}| |\vec{p}_t| \cos \theta] \\ &= m_t^2 - 2 \left[\frac{1}{2} \sqrt{s} \frac{s + m_t^2}{2\sqrt{s}} + \frac{1}{2} \sqrt{s} \frac{s - m_t^2}{2\sqrt{s}} \cos \theta \right] \\ &= m_t^2 - \frac{1}{2} [s + m_t^2 + (s - m_t^2) \cos \theta] \\ &= -\frac{1}{2} (s - m_t^2) (1 + \cos \theta) \end{aligned} \quad (3.25)$$

Putting everything together, we get

$$\begin{aligned} \frac{d\sigma}{d \cos \theta} &= \frac{1}{32\pi s} \frac{|p_t|}{p_b} |\mathcal{M}|^2 \\ &= \frac{1}{128\pi s} g_w^4 |V_{ud}|^2 |V_{tb}|^2 \frac{s - m_t^2}{s} \frac{(2p_t \cdot p_d)(2p_b \cdot p_u)}{(k^2 - m_W^2)^2} \\ &= \frac{1}{128\pi s} g_w^4 |V_{ud}|^2 |V_{tb}|^2 \frac{s - m_t^2}{s} \frac{(s - m_t^2)s}{\left(-\frac{1}{2}(s - m_t^2)(1 + \cos \theta) - m_W^2\right)^2} \\ &= \frac{1}{32\pi s} g_w^4 |V_{ud}|^2 |V_{tb}|^2 \frac{1}{\left((1 + \cos \theta) + \frac{2m_W^2}{s - m_t^2}\right)^2} \end{aligned} \quad (3.26)$$

This means that decays with large θ are more likely which means that the top is emitted in the direction of the incoming bottom. We can also calculate the cross section for s -channel single top production

$$|\mathcal{M}|^2 = \frac{1}{4} g_w^4 |V_{ud}|^2 |V_{tb}|^2 \frac{(2p_t \cdot p_{\bar{d}})(2p_{\bar{b}} \cdot p_u)}{(k^2 - m_W^2)^2} \quad (3.27)$$

where $k^2 = (p_u + p_{\bar{d}})^2 = 2p_u p_{\bar{d}}$. Let us again calculate the kinematic variables. We can parameterize the incoming momenta as $p_u = (E, \vec{p})$ and $p_{\bar{d}} = (E, -\vec{p})$ and the outgoing momenta as $p_t = (E_t, \vec{p}_t)$ and $p_{\bar{b}} = (E_{\bar{b}}, -\vec{p}_t)$ where $|\vec{p}| = E$, $|\vec{p}_t| = E_{\bar{b}}$ and $|\vec{p}_t|^2 + m_t^2 = E_t^2$. We know from energy conservation that

$$(E_u + E_{\bar{d}})^2 = (2E)^2 = s \quad (3.28)$$

where s is the squared center of mass energy. We can express E_t as

$$E_t^2 = |\vec{p}_t|^2 + m_t^2 = E_{\bar{b}}^2 + m_t^2 = (2E - E_t)^2 + m_t^2 = s - 2\sqrt{s}E_t + E_t^2 + m_t^2. \quad (3.29)$$

Solving this equation gives an expression for E_t :

$$E_t = \frac{s + m_t^2}{2\sqrt{s}} \quad (3.30)$$

Similarly we get

$$|\vec{p}_t| = \frac{s - m_t^2}{2\sqrt{s}} \quad (3.31)$$

Using this equation we can calculate the product of the momentum 4-vectors

$$\begin{aligned}
2p_t p_{\bar{d}} &= 2 [E E_t + |\vec{p}| |\vec{p}_t| \cos \theta] \\
&= \frac{1}{2} [(s + m_t^2) + (s - m_t^2) \cos \theta] = m_t^2 + \frac{1}{2}(s - m_t^2)(1 + \cos \theta) \\
2p_{\bar{b}} p_u &= 2 [E E_{\bar{b}} + |\vec{p}| |\vec{p}_t| \cos \theta] \\
&= \frac{1}{2} [(s - m_t^2) + (s - m_t^2) \cos \theta] = \frac{1}{2}(s - m_t^2)(1 + \cos \theta) \\
k^2 &= (p_u - p_{\bar{d}})^2 = 4E^2 = s
\end{aligned} \tag{3.32}$$

Plugging everything together we get

$$\begin{aligned}
\frac{d\sigma}{d \cos \theta} &= \frac{1}{32\pi s} \frac{|p_t|}{p_u} |\mathcal{M}|^2 \\
&= \frac{1}{128\pi s} g_w^4 |V_{ud}|^2 |V_{tb}|^2 \frac{s - m_t^2}{s} \frac{(2p_t \cdot p_{\bar{d}})(2p_{\bar{b}} \cdot p_u)}{(k^2 - m_W^2)^2} \\
&= \frac{1}{128\pi s} g_w^4 |V_{ud}|^2 |V_{tb}|^2 \frac{s - m_t^2}{s} \\
&\quad \cdot \frac{(m_t^2 + \frac{1}{2}(s - m_t^2)(1 + \cos \theta))(\frac{1}{2}(s - m_t^2)(1 + \cos \theta))}{(s - m_W^2)^2} \\
&= \frac{1}{256\pi} g_w^4 |V_{ud}|^2 |V_{tb}|^2 (1 - \frac{m_t^2}{s}) \\
&\quad \cdot \frac{(\frac{m_t^2}{s}(1 + \cos \theta) + \frac{1}{2}(1 - \frac{m_t^2}{s})(1 + \cos \theta)^2)}{(1 - \frac{m_W^2}{s})^2}
\end{aligned} \tag{3.33}$$

Here θ is the angle between the top and the up quark. We see that the top is more likely to be emitted in the direction of the incoming up quark.

Up to now we looked only at the leading order contribution for s -channel and t -channel single top production. At this stage we can distinguish both channels by their different final states. At next to leading order this situation is not obvious anymore. Let us consider that there is an initial state gluon that splits into two quarks. Then it is possible that both channels have the same initial state consisting of a gluon and a light quark q and the same final state consisting of a top, a \bar{b} and a light quark q' . Therefore, it might be possible that both channels interfere. The corresponding Feynman diagrams are shown in Fig. 3.9.

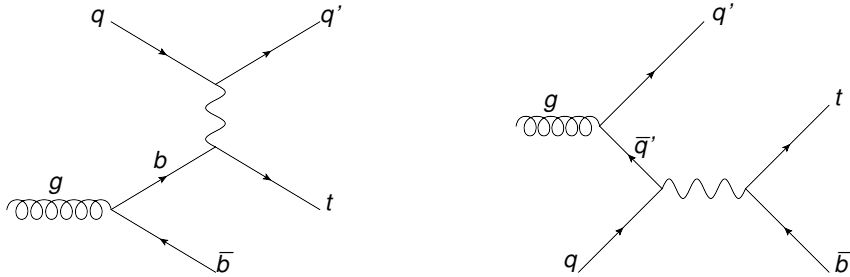


Figure 3.9: NLO correction for t -channel and s -channel single top production with the same initial state and final state particles.

If such an interference term exist we cannot distinguish the two productions channels anymore at NLO. Let us therefore look at the matrix elements. Each quark q has a momentum p_q in the direction of the fermion line and a color c_q . The gluon has a SU(3)-symmetry group index a and a spin σ . For the left diagram coming from t -channel single top production we get

$$\begin{aligned}
i\mathcal{M}_t &= \left[\bar{u}_{q'}(p_{q'}, c_{q'}) \frac{ig_W}{2\sqrt{2}} \gamma^\mu (1 - \gamma_5) V_{qq'} \delta_{c_q c_{q'}} u_q(p_q, c_q) \right] \frac{-ig_{\mu\nu}}{p_W^2 - m_W^2} \\
&\quad \cdot \left[\bar{u}_t(p_t, c_t) \frac{ig_W}{2\sqrt{2}} \gamma^\nu (1 - \gamma_5) V_{tb} \delta_{c_t c_b} \right] \frac{i(\not{p}_b + m_b)}{p_b^2 - m_b^2} [ig\gamma^\sigma (t^a)_{c_b, c_{\bar{b}}} v_{\bar{b}}(p_{\bar{b}}, c_{\bar{b}})] \\
&= \delta_{c_q c_{q'}} \delta_{c_t c_b} (t^a)_{c_b, c_{\bar{b}}} \cdot A(p, s) = \delta_{c_q c_{q'}} (t^a)_{c_t, c_{\bar{b}}} \cdot A(p, s).
\end{aligned} \tag{3.34}$$

In the last step we have split the matrix element into a color part and a part $A(p, s)$ that depends on the momentum and spin variables. Analogously, we can write for the diagram coming from s -channel single top production,

$$\begin{aligned}
i\mathcal{M}_s &= \left[\bar{u}_t(p_t, c_t) \frac{ig_W}{2\sqrt{2}} \gamma^\mu (1 - \gamma_5) V_{bt} \delta_{c_t c_{\bar{b}}} v_{\bar{b}}(p_{\bar{b}}, c_{\bar{b}}) \right] \frac{-ig_{\mu\nu}}{p_W^2 - m_W^2} \\
&\cdot \left[\bar{u}_{q'}(p_{q'}, c_{q'}) ig \gamma^\sigma (t^a)_{c_{q'}, c_{\bar{q}'}} \right] \frac{i(\not{p}_{\bar{q}'} + m_{\bar{q}'})}{p_{\bar{q}'}^2 - m_{\bar{q}'}^2} \left[\frac{ig_W}{2\sqrt{2}} \gamma^\nu (1 - \gamma_5) V_{qq'} \delta_{c_q c_{\bar{q}'}} u_q(p_q, c_q) \right] \\
&= \delta_{c_q c_{\bar{q}'}} \delta_{c_t c_{\bar{b}}} (t^a)_{c_{q'}, c_{\bar{q}'}} \cdot B(p, s) = \delta_{c_t c_{\bar{b}}} (t^a)_{c_{q'}, c_q} \cdot B(p, s).
\end{aligned} \tag{3.35}$$

Again $B(p, s)$ is a function depending on momentum and spin variables. The squared matrix element is

$$|\mathcal{M}|^2 = |\mathcal{M}_t + \mathcal{M}_s|^2 = |\mathcal{M}_t|^2 + |\mathcal{M}_s|^2 + \mathcal{M}_t^* \mathcal{M}_s + \mathcal{M}_s^* \mathcal{M}_t \tag{3.36}$$

The interference is described by $\mathcal{M}_t^* \mathcal{M}_s$. After summing over all final state color configurations and averaging over initial state colors we get

$$\begin{aligned}
\frac{1}{3} \sum_{colors} \mathcal{M}_t^* \mathcal{M}_s &= \frac{1}{3} \sum_{c_q} \sum_{c_{q'}} \sum_{c_{\bar{b}}} \sum_{c_t} \delta_{c_q c_{q'}} (t^a)_{c_t, c_{\bar{b}}} \delta_{c_t c_{\bar{b}}} (t^a)_{c_{q'}, c_q} \cdot A(p, s)^* B(p, s) \\
&= \frac{1}{3} \sum_{c_q} \sum_{c_t} (t^a)_{c_t, c_t} (t^a)_{c_q, c_q} \cdot A(p, s)^* B(p, s) \\
&= \frac{1}{3} \text{Tr}(t^a) \text{Tr}(t^a) A(p, s)^* B(p, s) = 0.
\end{aligned} \tag{3.37}$$

We have used that the generators t^a of the SU(3) group are traceless. Therefore we have shown that there is no interference of s -channel and t -channel single top production at next-to-leading order. At next to next to leading order this is not true anymore. Let us therefore look at the Feynman diagrams shown in Fig. 3.10.

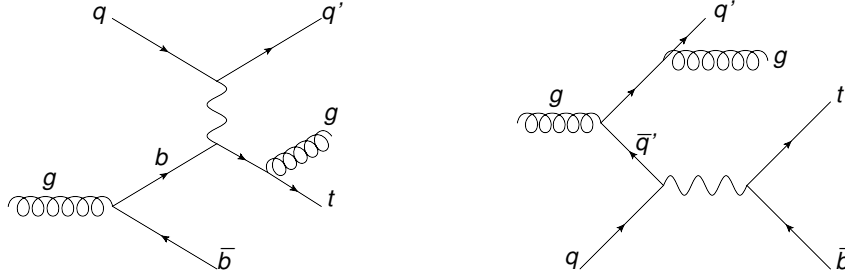


Figure 3.10: NNLO correction for t -channel and s -channel single top production with the same initial state and final state particles.

Again we assign a color c_q to each quark q . The incoming gluon has a group index a , the outgoing gluon has a group index b . Then we can write the matrix elements for both processes as

$$\begin{aligned}
i\mathcal{M}_t &= \delta_{c_q c_{q'}} (t^a)_{c_b, c_{\bar{b}}} \delta_{\tilde{c}_t c_b} (t^b)_{c_t, \tilde{c}_t} \cdot A(p, s) = \delta_{c_q c_{q'}} (t^b t^a)_{c_t, c_{\bar{b}}} \cdot A(p, s) \\
i\mathcal{M}_s &= \delta_{c_q c_{\bar{q}'}} (t^a)_{\tilde{c}_{q'}, c_{\bar{q}'}} (t^b)_{c_{q'}, \tilde{c}_{q'}} \delta_{c_t c_{\bar{b}}} \cdot B(p, s) = (t^b t^a)_{c_{q'}, c_q} \delta_{c_t c_{\bar{b}}} \cdot B(p, s).
\end{aligned} \tag{3.38}$$

where \tilde{c}_t and $\tilde{c}_{q'}$ are used for color of the internal quark. Therefore the interference term can be written as

$$\begin{aligned}
\frac{1}{3} \sum_{colors} \mathcal{M}_t^* \mathcal{M}_s &= \frac{1}{3} \sum_{c_q} \sum_{c_{q'}} \sum_{c_{\bar{b}}} \sum_{c_t} \delta_{c_q c_{q'}} (t^b t^a)_{c_t, c_{\bar{b}}} (t^b t^a)_{c_{q'}, c_q} \delta_{c_t c_{\bar{b}}} \cdot A(p, s)^* B(p, s) \\
&= \frac{1}{3} \sum_{c_q} \sum_{c_t} (t^b t^a)_{c_t, c_t} (t^b t^a)_{c_q, c_q} \cdot A(p, s)^* B(p, s) \\
&= \frac{1}{3} \text{Tr}(t^b t^a) \text{Tr}(t^b t^a) A(p, s)^* B(p, s) = \frac{1}{3} C(r)^2 \delta^{ab} A(p, s)^* B(p, s).
\end{aligned} \tag{3.39}$$

where $C(r)$ is a constant depending on the representation of the group which does not vanish. Therefore there exists an interference between s -channel and t -channel single top production at next-to-next to leading order.

3.4 Angular distribution in single top decay

Now we want to measure the angular correlation in t -channel single top production. Therefore we must know the direction of the incoming bottom quark. To determine this direction we can use properties of decay kinematics and the parton distribution function of the incoming quarks.

At first we expect to tag one top and one recoil jet that balance this top. The combined transverse momentum should be small and the center of mass momentum of the top and the hardest recoil jet should be parallel to the beam axis. Furthermore, we expect the bottom to have a smaller momentum fraction than the up quark and therefore the center of mass momentum should point in the direction of the incoming up quark. If we define $\theta^*(p_t, p_j)$ [73] to be the angle between the top momentum p_t in the rest frame and the center of mass momentum $p_t + p_j$ in the lab frame (which we expect to point in the direction of the up quark) we see that $\theta^* \approx \theta$ where θ is the angle we calculated before (see Fig. 3.11).

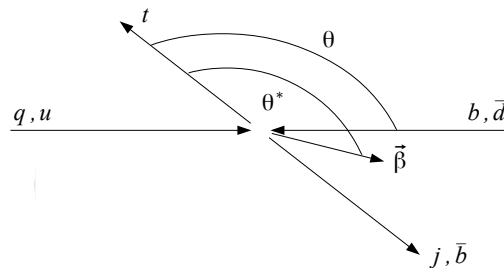


Figure 3.11: Definition of angle θ^* for t,s -channel single top production. β denotes the center of mass momentum $p_t + p_j$ in the lab frame. Figure taken from [41]

That means the angle θ^* should be large as well and therefore $\cos\theta^* \approx -1$. As we will see this behavior only occurs for t -channel single top production and we can use this angle to identify this process.

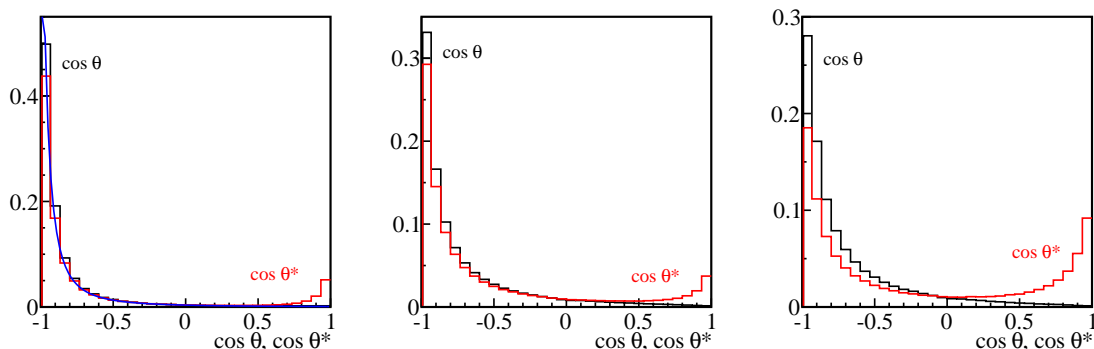


Figure 3.12: θ (black) and θ^* (red) distribution for t -channel single top production. Curves are discussed in the text.

In the left panel of Fig. 3.12 we show the normalized differential cross section as a function of θ and θ^* of the process $u + b \rightarrow t + d$ and $d + \bar{b} \rightarrow u + \bar{t}$ for a fixed center of mass energy $\sqrt{s} = 500$ GeV. The blue line shows the prediction by theory using the equation derived in the previous section, the black line shows the distribution of $\cos\theta(p_t, p_u)$ and the red line shows the distribution

of $\cos\theta^*(p_t, p_d)$. We see that the theory prediction matches the distribution of the decay angle θ . For some events the distributions for $\pi - \theta$ and θ^* differ due to the fact that the center of mass momentum does not point in the direction of the u quark but in the direction of the b quark.

The central panel of Fig. 3.12 shows the same distribution for the whole center-of-mass energy range. We see that this distribution did not change significantly and still has a peak for $\cos\theta^* \approx -1$. The right plot shows the same distribution but for the processes with an incoming antiquark: $\bar{u} + \bar{b} \rightarrow \bar{t} + \bar{d}$ and $\bar{d} + b \rightarrow \bar{u} + t$. The differential cross section (black line) does not change. But sometimes the center of mass momentum points into the direction of the incoming bottom quark and therefore $\theta^* = \pi - \theta$. As a result we observe an additional peak at $\cos\theta^* \approx 1$. Fortunately this process is suppressed by the parton distribution function.

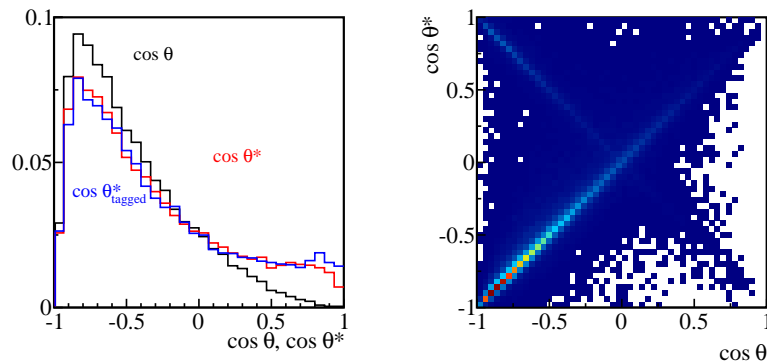


Figure 3.13: (left: θ (black) and θ^* distribution for t -channel single top production using parton level top (red) and tagged top (blue) information. right: $\cos\theta$ vs. $\cos\theta^*$ distribution for t -channel single top production. Dense region is shown in red. Figure taken from [41].

Fig. 3.13 (left panel) shows the same distribution for events in which a top is tagged. We can see that tops with $\cos\theta = \pm 1$ are not detected since they are emitted in direction of the beam (black line). But we still have a peak at negative values of $\cos\theta^*$ (red line). Using the tagged top and its recoil jet instead of the parton level top does not change this behavior (blue line). The right panel of Fig. 3.13 shows the correlation between $\cos\theta$ and $\cos\theta^*$ at parton level. We see that for most events both variables are equal $\cos\theta^* = \cos\theta$. In some events, the incoming b quark is harder than the incoming light quark what leads to the relation $\cos\theta^* = -\cos\theta$.

We can calculate the same angle also for s -channel single top production. We have seen that the top prefers to be emitted in the direction of the incoming up quark. Again we expect that the center of mass momentum of the top and the bottom should have low transverse momentum and should be parallel to the beam axis. But we also expect that the up quark has a bigger momentum fraction than the anti-down quark and therefore the center of mass momentum should point into the direction of the up quark. The angle $\theta^*(p_t, p_{\bar{b}})$ is similar to the angle we used in the calculation of the cross section above $\theta^* \approx \theta$. Therefore should have a peak at $\cos\theta^* \approx 1$. This is exactly the opposite behavior of the t -channel single top production.

Let us compare this prediction with a Monte Carlo simulation (see Fig. 3.14). The left plot shows the differential cross section as a function of θ and θ^* for the process $u + \bar{d} \rightarrow t + \bar{b}$ for a fixed center of mass energy $\sqrt{s} = 500$ GeV. The blue line shows the prediction by theory using the equation derived in the previous section, the black line shows the distribution of $\cos\theta(p_t, p_u)$ and the red line shows the distribution of $\cos\theta^*(p_t, p_{\bar{b}})$. Again we see that the theory prediction matches the distribution of the decay angle θ . For some events the distributions for θ and θ^* differs due to the fact that the center of mass momentum does not point in the direction of the u quark but in the direction of the \bar{d} quark. This happens in about 10% of the events.

If we look at the distribution for the whole range of center of mass energies \sqrt{s} shown in the central panel we see that the distribution did not change significantly. Again $\cos\theta$ and $\cos\theta^*$ may differ since the center of mass momentum points not in the direction of the up quark.

The right plot shows the same distribution for the process $\bar{u} + d \rightarrow \bar{t} + b$ which occurs in approximately 30% of the s -channel single top events. This does not change the differential cross section (where θ is now the angle between the anti-top and the incoming down quark) as we can

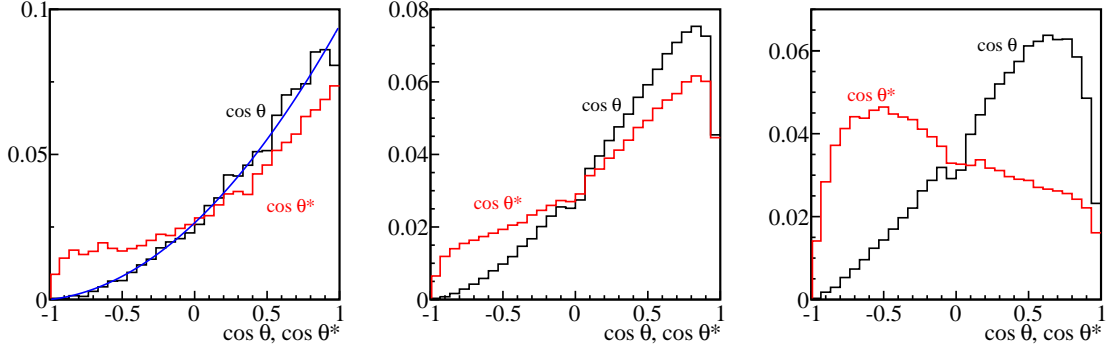


Figure 3.14: $\cos(\theta)$ (black) and $\cos(\theta^*)$ (red) for s -channel single top production. Curves are discussed in the text.

see looking at the black line. But now the center of mass momentum tends to be parallel to the incoming down quark and therefore the peak of the $\cos \theta^*$ distribution (red line) is shifted towards negative values.

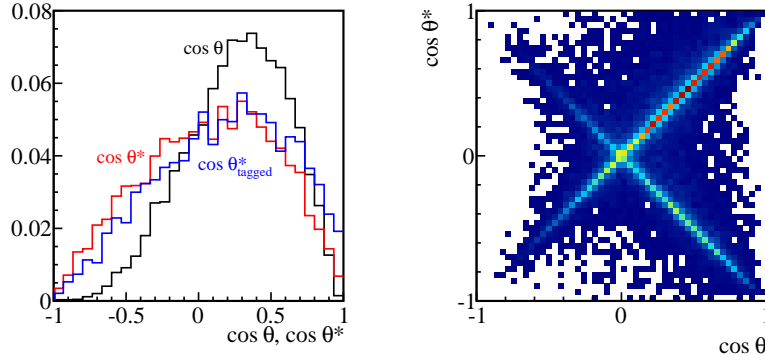


Figure 3.15: left: $\cos \theta$ (black) and $\cos \theta^*$ distribution using parton level top (red) and tagged top (blue) for s -channel single top production. right: $\cos \theta$ vs. $\cos \theta^*$ distribution for s -channel single top production. Dense region is shown in red. Figure taken from [41].

These distributions change significantly after we use the top tagger. Fig. 3.15 shows the distributions for events with exactly one tagged top. The black line shows the distribution of $\cos \theta$ where θ is the angle between the top quark and the incoming anti-down (or down) quark in parton level. We see that it still has a peak at positive values as we would expect. Large values of $\cos \theta$ are cut off since we require a minimal transverse momentum of the top. Tops emitted parallel to the beamline are not detected anymore. The red line shows the distribution of θ^* using again the parton level quarks. Since both processes contribute, there is no clear peak anymore. But since the process $u + \bar{d} \rightarrow t + \bar{b}$ occurs more often, the peak is slightly shifted towards a positive value of $\cos \theta^*$. This behavior does not change if we use the tagged top momentum (blue line). As we can see in the right panel of Fig. 3.15, $\cos \theta^* = \pm \cos \theta$ depending on the center-of-mass momentum direction of the system.

One of the main backgrounds for single top production will be $t\bar{t}$ production. In our analysis we will apply a lepton veto and require exactly one tagged top. That means for top pair production that the second top did not pass the HEPTopTagger. But there should still be at least one jet (probably more than one) that comes from the second top. The kinematic situation for $t\bar{t}$ events is shown in Fig. 3.16. We expect one of these jets to be the hardest recoil jet. Since this jet does not include the complete second top, it will not balance the transverse momentum of the tagged top. We can use this information to eliminate most of the $t\bar{t}$ events if we require the transverse

part of the center-of-mass momentum in the lab frame $p_t + p_j$ to be small.

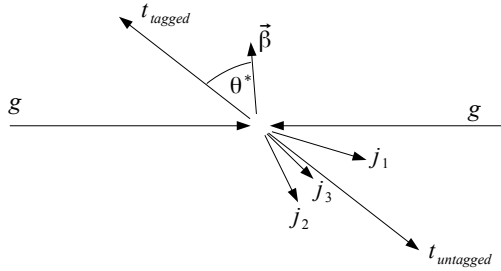


Figure 3.16: Angle θ^* for $t\bar{t}$ production. Instead of the untagged top we detect several recoil jets corresponding to the top decay products. β denotes the boost vector towards the center-of-mass system of the tagged top and the hardest recoil jet.

Since the top has a higher momentum than the hardest recoil jet we expect the center of mass momentum of these two jets to point in the direction of the tagged top. Therefore the angle θ^* should be small and $\cos\theta^* \approx 1$. This is again different compared to t -channel single top production. If we look at Fig. 3.17 we see this is indeed the case. The red line shows the θ^* distribution of the parton level top that correspond to the tagged top and the hardest subjet of the other top. The red line show the same distribution using the tagged top and the hardest recoil jet. We see that both prefer to have positive values and there is no big difference between these distributions.

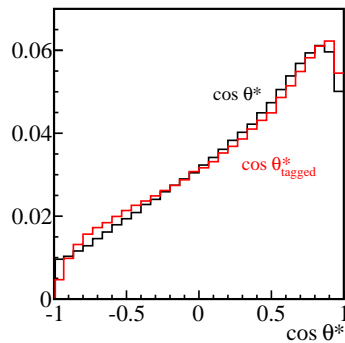


Figure 3.17: θ^* distribution using parton level top (black line) and tagged top (red line) for $t\bar{t}$ production.

For the QCD background, we expect events that pass our tagger to look similar to a signal event including a top quark. Due to their di-jet topology we expect one jet to mimic a top quark while the other jet forms a recoil which can balance the mis-tagged tops transverse momentum. Since there are a lot of possible QCD events we expect no specific angular dependence of the top. If the top and the recoil jet balance each other the center of mass momentum should be parallel to the beam direction but there is no preferred direction with respect to the incoming partons.

Chapter 4

Analysis

4.1 Event Generation

The aim of our analysis is to detect single top events. Therefore we have to distinguish them from other background events predicted by the standard model [74, 75, 76]. Since the HEPTopTagger uses hadronically decaying tops our main background will be QCD jets as well as W +jets in which some of these jets are misidentified as a top. The other main background is top pair production. Furthermore we consider $tW(b)$ single top production as an additional background in this paper. Here, tWb production is similar to top pair production but with one off-shell top which then decays into a W and b .

For this analysis we use ALPGEN+PYTHIA [77, 78, 79] to generate all event samples. To simulate the signal events as well as the single top background $tW(b)$ we use only leading order production without matching. For tWb we use the ALPGEN default description. Here the Wb invariant mass is restricted to be $|m_{Wb} - m_t| < 5$ GeV. This avoids double counting with $t\bar{t}$ events. For the other background processes additional hard radiation is encountered. We use MLM matching [80] to simulate it. For $t\bar{t}$ samples we take into account up to two additional jets. This is necessary since the cross section of $t\bar{t} + 2$ jets is about 25% of the leading order cross section. After top tagging this number will be smaller since additional jets will decrease the transverse momentum of each top and therefore it will not exceed the p_T -threshold anymore. Therefore we will not encounter more additional jets. For QCD we will take into account 3-5 jet samples. Although W +jets turns out to be a minor background we simulate up to three additional jets for 8 TeV and up to five jets for 14 TeV.

The cross sections for s/t -channel, $t\bar{t}$ and tW -channel are normalized to the approximate NNLO rates [60, 81]. A top mass $m_t = 173$ GeV is used. For QCD and W +jet background we use the leading order normalization. These cross sections are shown in Tab. 4.1 [82, 83, 84, 85, 86].

cross section[pb]	s -channel	t -channel	$t\bar{t}$	$tW(b)$	QCD	W +jet
8 TeV	5.55	87.1	234	22.2 + 18.4	$652 \cdot 10^3$	1576
14 TeV	11.86	248	920	83.6 + 76.6	$1.94 \cdot 10^6$	3880

Table 4.1: Signal and background cross sections in pb for LHC at 8 [81] and 14 TeV [60] used for the analysis.

To get a more realistic description we will use the fast detector simulation Delphes to simulate the ATLAS detector [87]. For our analysis this has two effects: a finite efficiency for isolated lepton detection and a smearing of the kinematic variables of the final state particles. Delphes considers a lepton as isolated if there is no other charged particle with $p_T > 10$ GeV within a cone of $R = 0.5$. This leads to a detection probability of isolated leptons of approximately 56% for leptonic top decays. This is similar to the tight configuration ATLAS uses [88] and can therefore be considered as realistic. If we would choose a looser configuration this would lead to a larger number of misidentified, unisolated leptons. We try to avoid this behavior because we will reject leptonic events in our analysis.

As input for the tagging algorithm we will use the calorimeter data provided by Delphes. This takes into account the segmentation of the calorimeter and the smearing of the calorimeter cell

energy. This can lead to different clustering behaviors under a jet algorithm. Therefore, it may happen that tops that were tagged without Delphes are not tagged anymore after applying Delphes or vice-versa. A more detailed discussion of Delphes and its effect on the tagging procedure can be found in the Appendix.

In this section we will discuss our strategy for the detection of single top production. This strategy will be illustrated using the t -channel single top production at 8 TeV LHC. It will turn out that most of these steps can be used for the detection of s -channel single top production and for the analysis at 14 TeV as well. Our analysis can be divided into three steps: the analysis of the tagged top itself, the analysis of the system of top and recoil jet and finally the recoil jet itself. Afterwards we will show changes in our strategy and additional cuts needed for the detection of s -channel single top production.

4.2 Top tag

In parton level the final state in signal events consists of a top and a recoil jet. We will first focus on the top itself. As a first step we will require a top tag. Since our top tagger is designed to tag hadronic top we expect signal events to be fully hadronic. Therefore we will reject events including isolated leptons in our analysis. Furthermore we will reject all events with more than one top since we want to avoid $t\bar{t}$ contamination.

The HEPTopTagger algorithm requires a C/A fat jet [65] with $p_{T,fat} > 200$ GeV with specific internal structure of the subjets where we used the default configuration as described in [37]. Fig. 4.1 shows the distribution of the transverse momentum of tops in single top and top pair production at LHC with 8 TeV. The table shows the predicted rates for tops exceeding different transverse momentum thresholds. We see that tops in $t\bar{t}$ background tend to have larger transverse momentum. Therefore top tagging itself will decrease $\sigma_t/\sigma_{t\bar{t}}$. On the other hand the ratio between s -channel and t -channel cross section becomes better after requiring larger p_T .

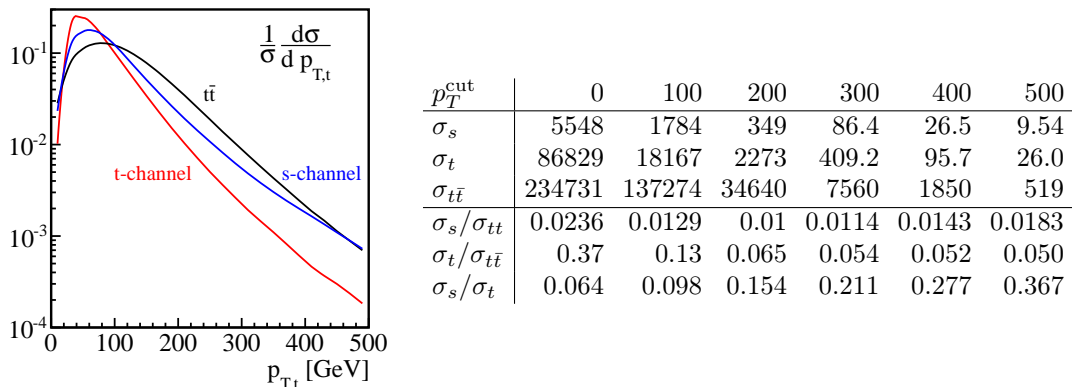


Figure 4.1: Left: Normalized p_T distribution for s -channel (blue), t -channel (red) and $t\bar{t}$ (black) at LHC 14 TeV run. Right: Signal and background cross section with top p_T cuts at 8 TeV LHC in fb. For $t\bar{t}$ the numbers are for the events with at least one top passing the p_T cut. Figure taken from [41].

event	t -ch.	s -ch.	$t\bar{t}$	$tW(b)$	QCD	W +jets
cross section [fb]	$87.2 \cdot 10^3$	$5.55 \cdot 10^3$	$234 \cdot 10^3$	$(22.2+18.4) \cdot 10^3$	$652 \cdot 10^6$	$1.57 \cdot 10^6$
hadronic events [fb]	$72.5 \cdot 10^3$	$4.70 \cdot 10^3$	$173 \cdot 10^3$	$31.5 \cdot 10^3$	$652 \cdot 10^6$	$1.36 \cdot 10^6$
tagged events [fb]	400	60.9	8389	676	$259 \cdot 10^3$	4106

Table 4.2: Signal and background cross section for all events, after isolated lepton veto and after requiring exactly one top tag.

Tab. 4.2 shows the cross sections for the signal and background after top tagging. We can see that

top tagging itself it not sufficient enough to reduce QCD background. We will therefore modify the configuration of the HEPTopTagger to achieve a better QCD rejection. In the HepTopTagger algorithm we look at the plane of mass ratios m_{23}/m_{123} and $\arctan m_{13}/m_{12}$. Afterwards we assign the subjects in a way so that the jets number 2 and 3 correspond to the W decay products and jet 1 is the b subjet. Since we expect two of these jets to be decay product of a W in the algorithm we require m_{23}/m_{123} to give the expected mass ratio of m_W/m_t with an uncertainty of $\pm f_W/2 \cdot m_W/m_t$. The other mass plane variable is used to reject QCD events which tend to have small values of m_{13}/m_{12} . For these variables we can choose stronger cuts. Another variable we can look at is the mass of the tagged top m_{top} . This variables are shown in Fig. 4.2.

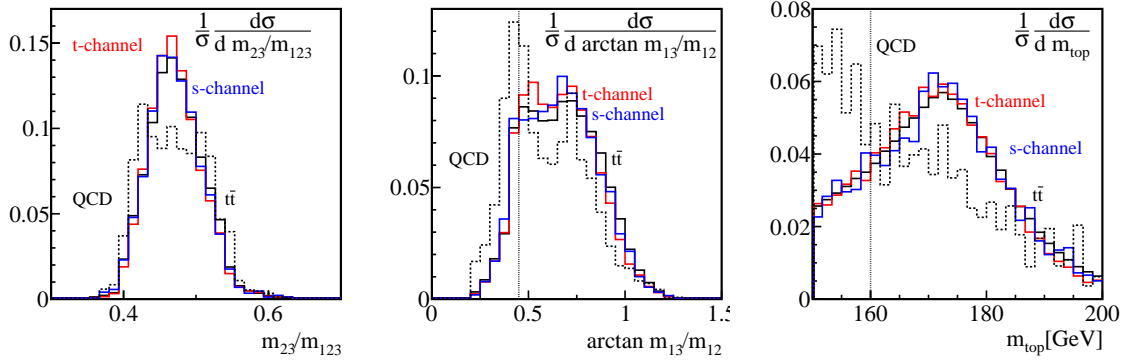


Figure 4.2: Normalized distribution of m_{23}/m_{123} (left), $\arctan m_{13}/m_{12}$ (center) and m_{top} (right) using the default configuration of the HEPTopTagger.

We can see clear differences between the events including a top and mis-tagged QCD events. For QCD events the m_{23}/m_{123} distribution (left panel) is broader and the $\arctan m_{13}/m_{12}$ (central panel) shows a peak at small values. This peak corresponds to soft radiation. Therefore we can choose a smaller window for the W -mass and cut off the peak. The right panel shows the mass of the top quark itself. Events including a top have a peak around the top mass. The number of QCD events decreases exponentially with higher masses. We can therefore cut off tagged tops with small masses. Different choices for cuts and their improvement factor compared to the default setting are shown in Tab. 4.3. A good choice for cuts which we will use later is $f_W = 0.2$, $\arctan m_{13}/m_{12} > 0.45$ and $160 \text{ GeV} < m_{top} < 200 \text{ GeV}$ as denoted by the black line in Fig. 4.2.

	tagged	$f_W=0.25$	0.2	0.15	$\arctan \frac{m_{13}}{m_{12}} > 0.4$	0.45	0.5	$m_t > 155$	160	165
t-ch. [fb]	400	354	318	266	376	345	307	367	326	274
QCD [10^3 fb]	258	210	173	127	211	178	149	203	161	126
$\epsilon_{S/B}$	1	1.09	1.18	1.33	1.15	1.24	1.52	1.16	1.30	1.40
$\epsilon_{S/\sqrt{B}}$	1	0.96	0.97	0.94	1.04	1.04	1.01	1.04	1.04	0.98
$t\bar{t}$ [fb]	8390	7141	6236	5088	7836	7166	6446	7626	6745	5707
$\epsilon_{S/B}$	1	1.04	1.07	1.10	1.01	1.01	1.00	1.01	1.01	1.01
$\epsilon_{S/\sqrt{B}}$	1	0.96	0.92	0.85	0.97	0.93	0.88	0.96	0.91	0.83

Table 4.3: Tagged top rate (in fb for t -channel, QCD and $t\bar{t}$) after several choices for a cuts on m_{23}/m_{123} , $\arctan m_{13}/m_{12}$ and m_{top} . $\epsilon_{S/B}$ and $\epsilon_{S/\sqrt{B}}$ denote improvement factors relative to no cuts.

Up to now we have only looked at the filtered [68] mass which is used as the mass of the tagged top. In Ref. [39] there are mentioned two other mass variables provided by the HEPTopTagger: the pruned mass [69] and the unfiltered mass. These can be used to distinguish signal and background events. Since both variables show a similar behavior, we will concentrate on the pruned mass first. Pruning is a procedure that removes soft radiation while clustering the fat jet. Therefore it should have a similar impact on the top mass as filtering does. We have seen in the analysis of $t\bar{t}$ events [39], that we can use pruning to reject QCD background. Fig. 4.3 shows the correlation between the pruned mass m_{prune} and the filtered mass m_{filter} .

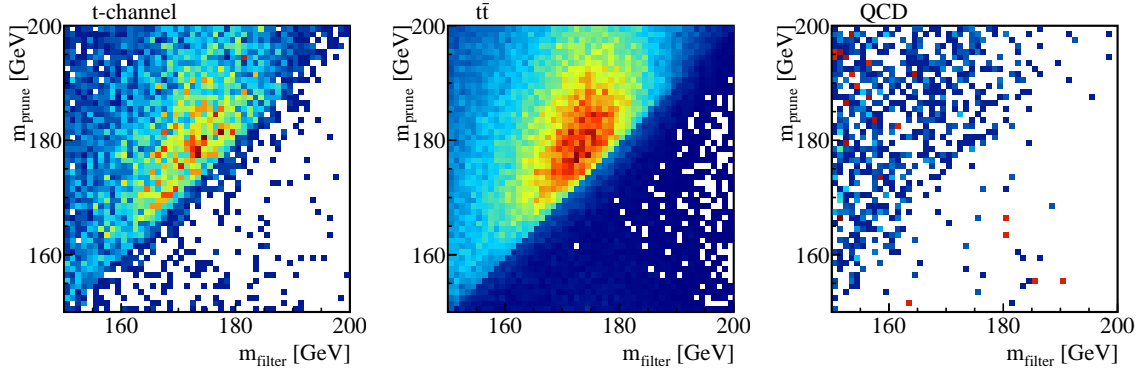


Figure 4.3: Two dimensional correlation of pruned mass and filtered mass for t -channel (left), $t\bar{t}$ (center) and QCD (right) using the HEPTopTagger default configuration. Dense region is shown in red.

We can see that for events including a top quark the pruned mass and the filtered mass are closely related. For QCD events there is not such a correlation. We will therefore look at the variable

$$\Delta m_{prune} = m_{prune} - m_{filter} \quad (4.1)$$

to distinguish the signal from the QCD background (see left panel of Fig. 4.4). While single top and $t\bar{t}$ events prefer small mass differences, QCD events tend to have larger values of Δm_{prune} . Compared with filtering, pruning discards less constituents. Therefore the pruned mass increases in the presence of radiation. This is the environment we expect in QCD. Therefore those events have a larger mass difference which we can cut off. Several choices for such cuts are shown in Tab. 4.4. We could also consider the unfiltered mass. Since we did not removed radiation we expect a higher unfiltered mass. The corresponding mass difference $\Delta m_{unfilter} = m_{unfilter} - m_{filter}$ can be seen in the right panel of Fig. 4.4. It shows a similar behavior as Δm_{prune} but with a shift towards larger mass differences. It would also be possible to use this variable instead of Δm_{prune} . An additional cut on the pruned mass itself is not promising.

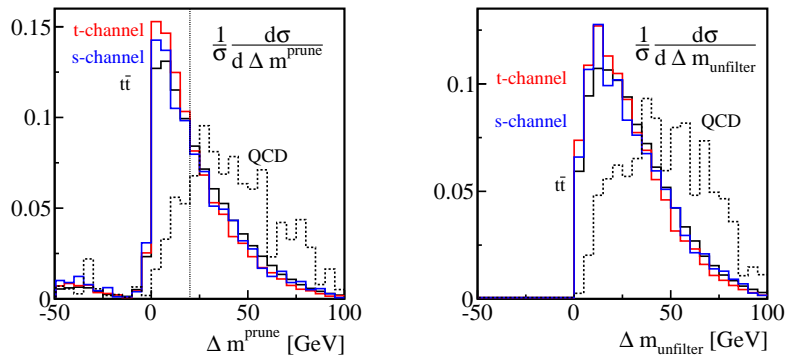


Figure 4.4: Δm_{prune} (left) and $\Delta m_{unfilter}$ (right) using the default configuration of the HEPTopTagger. Figure taken from [41].

To reduce more QCD background we require a bottom tag in the subset of the tagged top that is initiated from a bottom. As discussed in [39] this is the most promising strategy. Therefore, we check if a parton level bottom is inside this subset. Of course this subset-parton matching does not work perfectly and we will lose events due to the misassignment of a bottom initiated jet. On the other hand, we only have to perform one b -tag and can therefore reject much more QCD events than we would be able to reject if we perform three b -tags, one for each subset. In Fig. 4.5 we show how many b -subsets are really b -initiated or not. Assuming a b -tagging rate of $\epsilon_b = 50\%$ and

	tagged	$\Delta m_{prune} < 10$ GeV	20 GeV	30 GeV
t-ch. [fb]	400	108	191	251
QCD [10^3 fb]	258	16	40	76
$\epsilon_{S/B}$	1	4.41	3.11	2.11
$\epsilon_{S/\sqrt{B}}$	1	1.09	1.22	1.15
$t\bar{t}$ [fb]	8390	1716	3270	4542
$\epsilon_{S/B}$	1	1.32	1.22	1.16
$\epsilon_{S/\sqrt{B}}$	1	0.60	0.76	0.85

Table 4.4: Tagged top rate (in fb for t -channel, QCD and $t\bar{t}$) after several choices for a cuts on Δm_{prune} . $\epsilon_{S/B}$ and $\epsilon_{S/\sqrt{B}}$ denote improvement factors relative to the default configuration.

a mis-tagging rate of $\epsilon_{mis} = 1\%$ [89] we get improvement factors for b -tagging for each process. QCD and W +jets background events are suppressed by ϵ_{mis} since we assume that they do not contain a bottom quark.

We can see that events with a simple structure like $t\bar{t}$ (without additional jets), s -channel and t -channel top production have a higher probability for a correct assignment of the b -subjct. A busy environment with additional jets lowers the b -tagging rate within the top. In such a case more tops are incorrectly reconstructed.

process	s-ch.	t-ch.	$t\bar{t}$	$t\bar{t}j$	$t\bar{t}jj$	tW	tbW
correct matching	70.3%	67.1%	70.4%	58.4%	47.3%	56.4%	60.0%
b-tag improvement	35.4%	33.9%	35.5%	30.0%	24.2%	28.6%	30.3%

Table 4.5: Bottom tag efficiency for different channels. We consider each channel separately and determine how often the b-subjet is b-initiated. Afterwards, we include the b-tagging rate of 50% for correctly assigned b-subjets and a mis-tag rate of 1% for incorrectly assigned subjets.

To get a better QCD rejection we could change even more variables in the HEPTopTagger setting. An optimized choice was suggested by the Heidelberg ATLAS group [90]. Following their analysis we will change four variables in the tagging algorithm.

- maximal mass of single subjet:** After we find a fat jet, we undo the clustering (including a mass drop criteria) until we achieve a subjet with a mass smaller than m_j . We change this parameter from its default value of $m_j < 50$ GeV to $m_j < 30$ GeV.
- maximal size of filtered jet:** In the next step we filter this subjets with a resolution $R_{filter} = \min(R_{max}, \Delta R_{jk}/2)$. We change this R_{max} from its default value of 0.3 to 0.2.
- number of filtered jets:** Afterwards we take the n_{filt} hardest subjets and look for a combination of three of these subjets that is closest to the top mass. We change n_{filt} from 5 to 4.
- mass ratio uncertainty:** After we find the top candidate, we require that the mass of two of these subjets divided by the mass of the top candidate gives the expected mass ratio of m_W/m_t with an uncertainty of $\pm \frac{f_W}{2} \cdot m_W/m_t$. We change f_W from 30% to 20%.

The resulting cross sections after tagging and a comparison with the default configuration can be seen in Tab. 4.6. We can recognize that less QCD events pass the tagger since we have chosen more strict criteria. The signal over background ratio increases significantly. Especially the change of the maximal subjet size reduces the size of the jet and therefore only jets in which the energy is accumulated in the center of the jet will be used. As we can see in Fig. 4.5 (right) the filtered mass tends to be too small. It has a peak at $m = 165$ GeV but almost no tagged tops have a mass $m > 175$ GeV. By choosing stronger criteria in the tagging algorithm we have removed too much information while filtering and therefore decreased the mass of the top jet. Therefore, a cut on the top-mass window as applied in the default configuration is not promising anymore. We will still require $\arctan m_{13}/m_{12} > 0.45$.

The pruned mass (left panel) has its peak at the expected top mass of $m_{top} \approx 175$ GeV. Again, we look at the mass difference Δm_{prune} . Since the jet mass and the pruned mass have different

positions for their peak, we expect Δm_{prune} to have its peak not at zero. We will require $-10 \text{ GeV} < \Delta m_{prune} < 20 \text{ GeV}$. Indeed in Fig. 4.5 (center) we observe this shift. As before we will reduce the QCD background by requiring a b -tag in the b -initiated subject.

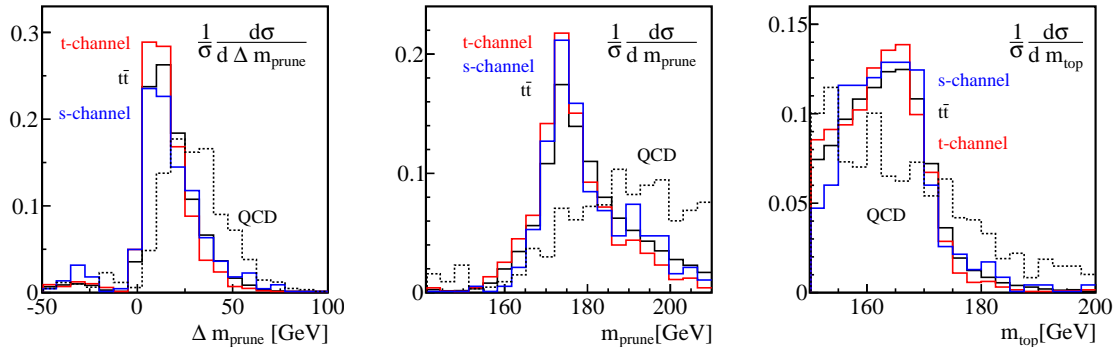


Figure 4.5: Normalized distribution of Δm_{prune} (left), m_{prune} (center) and m_{top} using the changed configuration of the HEPTopTagger.

The combined results after the cuts using the default and optimized configuration is shown in Tab. 4.6. The optimized setting of the HEPTopTagger itself gives a better signal over background but the efficiency of the applied cuts decreases. After applying all cuts the number of events S , S/B and S/\sqrt{B} are almost the same. On the other hand, we have seen that the filtered top mass is shifted towards smaller values. Therefore, we also expect that the momentum and energy in the top is shifted in some way from the parton level value. We want to avoid such an effect since we want to use the top momentum for further analysis. Therefore in the next sections we will use the default setting.

event	t -ch.	s -ch.	$t\bar{t}$	$tW(b)$	QCD	W +jets	S/B	$S/\sqrt{B}_{10fb^{-1}}$
tagged [fb] (default)	400	60.9	8389	676	$259 \cdot 10^3$	4106	0.0014	2.42
config [fb] (default)	244	35.5	4659	360	$79.3 \cdot 10^3$	1598	0.0028	2.63
Δm_{prune} [fb] (default)	124	16.56	1978	145	$10.8 \cdot 10^3$	601	0.0091	3.37
b -tag [fb] (default)	49.9	6.24	728	52.2	108.4	6.01	0.055	5.26
tagged [fb] (optimized)	280	48.0	5087	429	$64.2 \cdot 10^3$	1769	0.0039	3.31
config [fb] (optimized)	210	35.4	3820	318	$33.8 \cdot 10^3$	1135	0.0053	3.36
Δm_{prune} [fb] (optimized)	142	19.2	2171	180	$6.6 \cdot 10^3$	539	0.015	4.62
b -tag [fb] (optimized)	54.7	8.16	821	70.1	66.1	5.39	0.056	5.55

Table 4.6: Number of events that pass the selection cuts for t -channel single top production for 1 fb^{-1} . The upper part uses the default setting of the HEPTopTagger, the lower part uses the optimized setting.

4.3 Top and recoil jet system

Until now we have only concentrated on properties of the tagged top. This allowed us to reject most of the QCD background. After top tagging, $t\bar{t}$ production becomes the major background. To distinguish single top and top pair production we can use the properties of the recoil jet balancing the top. To obtain the recoil jet we cluster the calorimeter cells using the C/A algorithm with $R=0.5$. To avoid double usage of calorimeter information we only take into account the calorimeter cells that were not used for the reconstruction of the tagged top. Out of the set of jets we obtain, we select the hardest jet to be the recoil jet. We require this jet to be outside the fat jet corresponding to the tagged top and to have a transverse momentum $p_{T,j} > 25 \text{ GeV}$.

For single top production we expect the recoil jet to be initiated by a light quark (t -channel) or b -quark (s -channel) and therefore to balance the top. Thus, we will look at the momentum distribution of the system composed of a top and a recoil jet. We expect the behavior of the recoil jet

and its momentum to be independent of the internal structure of the top jet. Therefore we will look at event samples in which one top is tagged using the default configuration of the HEPTopTagger. Additional cuts discussed in the previous section are not applied.

To describe the tj -system we look at its transverse momentum $p_{T,tj}$ and its longitudinal momentum $p_{L,tj}$. The two-dimensional correlation $p_{L,tj}$ vs. $p_{T,tj}$ for t -channel single top production, $t\bar{t}$ production and their ratio is shown in Fig. 4.6.

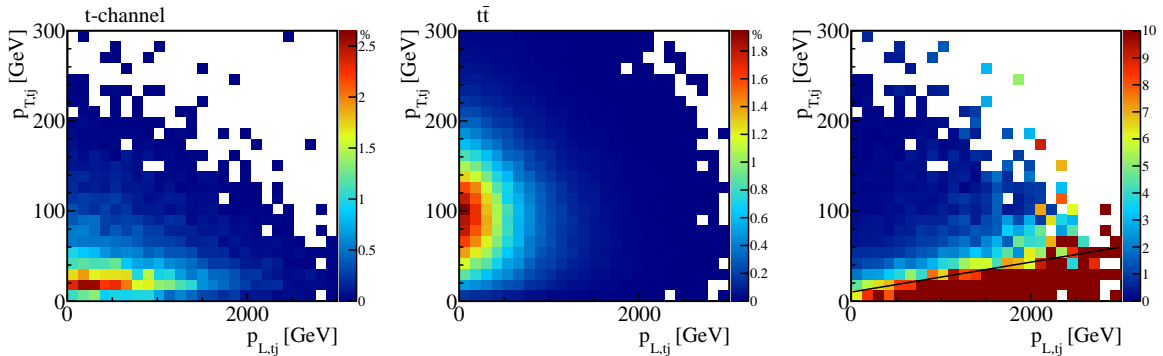


Figure 4.6: Transverse momentum $p_{T,tj}$ vs. longitudinal momentum $p_{L,tj}$ distribution for t -channel single top production (left), $t\bar{t}$ (center) and their ratio (right). Figure taken from [41].

We can see differences in the distributions between signal and background. For single top production we expect the top and recoil jet to balance each other and therefore the system to have small transverse momentum $p_{T,tj}$. The systems longitudinal momentum $p_{L,tj}$ in t -channel single top tends to be high since the initial state bottom quark carries a small momentum fraction and cannot balance the initial state light quark longitudinal momentum. The s -channel single top distribution is similar since we expect the initial state longitudinal momenta to be unbalanced as well.

In $t\bar{t}$ production we expect the recoil jet to correspond to a top decay product but not to the entire top. Therefore, the recoil jet cannot balance the tagged tops transverse momentum which results in a large $p_{T,tj}$. At the LHC, top pairs are mainly produced in gluon fusion. We expect the gluons longitudinal momentum to balance in a large event sample and therefore $p_{L,tj}$ to be relatively small. The right panel of Fig. 4.6 shows the ratio between the t -channel and $t\bar{t}$ distributions. We can see that there is a region with small $p_{T,tj}$ and large $p_{L,tj}$ which can be selected to enhance the signal versus $t\bar{t}$ background. Therefore we will apply a cut

$$p_{T,tj} < p_{L,tj0} + \frac{p_{L,tj}}{60}. \quad (4.2)$$

The black line in the right panel of Fig. 4.6 corresponds to the choice $p_{L,tj0} = 10$ GeV. Improvement factors for several choices of $p_{L,tj0}$ are shown in Tab. 4.7. We see that this cut also reduces some QCD background which is dominated by di-jets events. One of these jets will be mis-tagged as a top, the other jet will be detected as a recoil jet. If the recoil jet does not split in to jets with large separation $\Delta R > 0.5$, the event may look similar to the signal. Otherwise it will be similar to the $t\bar{t}$ case.

As discussed in the previous chapter in t -channel single top production it is possible to measure the decay angle. The initial state consists of a bottom quark and a light quark. Due to a softer PDF for b -quarks the bottom momentum p_b is expected to be smaller than the light quark momentum p_q . Therefore the center-of-mass momentum $p_b + p_q$ will point in the direction of the incoming light quark. If the tagged top and recoil jet correspond to the final state particles their system momentum p_{tj} should be similar to the initial state particles center-of-mass momentum. Therefore, the decay angle θ between the top and initial state light quark momentum is similar to the angle θ^* between the tagged tops direction in the systems rest frame and the system momentum direction in the lab frame. Using this relation we can predict θ^* to be large.

For s -channel single top production the initial state consists of a light quark and an anti-quark. If we define θ to be the angle between the d -like initial state quark and the top, it depends on the top charge if θ and θ^* as defined above are the same or not. Taking into account both s -channel top and anti-top production, we still expect to have small θ^* . Fig. 4.7 shows the normalized

	tagged	$p_{L,tj0} = 5$ GeV	10 GeV	15 GeV
t-ch. [fb]	400	85.1	118	152
QCD [10^3 fb]	258	23.5	40.2	58.1
$\epsilon_{S/B}$	1	2.33	1.90	1.70
$\epsilon_{S/\sqrt{B}}$	1	0.70	0.75	0.80
$t\bar{t}$ [fb]	8390	81.0	137	211
$\epsilon_{S/B}$	1	21.8	17.9	14.9
$\epsilon_{S/\sqrt{B}}$	1	2.15	2.30	2.37

Table 4.7: Tagged top rate (in fb for t -channel, QCD and $t\bar{t}$) after several choices for a cuts on the system momentum p_{tj} . $\epsilon_{S/B}$ and $\epsilon_{S/\sqrt{B}}$ denote improvement factors relative to the default configuration.

distribution for the angle θ^* before and after applying the cuts on the system momentum p_{tj} . We show t -channel (red line), s -channel (blue line) and $t\bar{t}$ (black line).

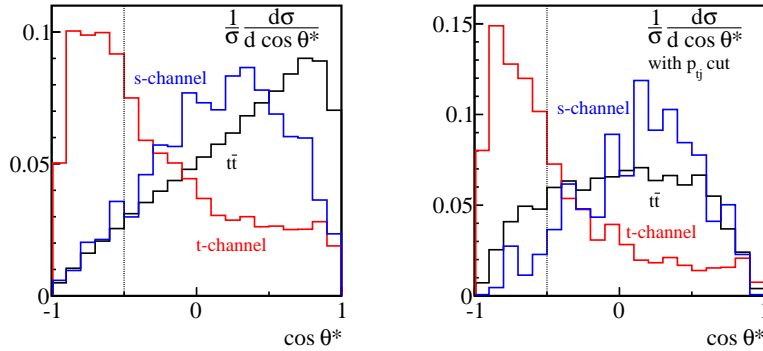


Figure 4.7: Normalized distribution of $\cos \theta^*$ before (left) and after (right) cut on the system momentum p_{tj} for t -channel (red), s -channel (blue) and $t\bar{t}$ (black). Figure taken from [41].

We see that the $t\bar{t}$ background events prefer to have large values for $\cos \theta^*$. If the recoil jet corresponds to a top decay product, it will not balance the top anymore. Therefore, the system momentum will point in the tagged top direction which leads to a small value for θ^* . Therefore this angle can be used to distinguish t -channel single top production from $t\bar{t}$ background. For QCD events we expect no special angular correlation and therefore a uniform distribution.

If we apply the cut on the system momentum p_{tj} we already force the system momentum to point along the beam direction. Since this is expected in single top production this cut does not change the distribution for single top events. For $t\bar{t}$ events the peak in the $\cos \theta^*$ distribution vanishes since it was caused by events with large $p_{T,tj}$. We obtain an almost uniform distribution. For QCD events we expect a similar behavior. If we want to extract the signal corresponding to t -channel single top production we have to choose events with small values for $\cos \theta^*$. Improvement factors for several choices of cuts are shown in Tab. 4.8. The black line in Fig. 4.7 corresponds to the choice $\cos \theta^* < -0.5$.

4.4 Internal structure of the recoil jet

Besides cuts in the tj -system, we can also look at the recoil jet itself. In top pair production we expect the recoil jet to be a top decay product of the untagged top. This top is expected to form a large jet. Therefore we can try to identify this recoil jet as part of a larger jet corresponding to the top. In single top production we only expect to see one recoil jet coming from a light or b -quark. This jet should have a small size without energy contributions around it.

In $t\bar{t}$ production we should be able to observe one jet coming from the b -quark produced in the decay of the untagged top. This jet can be identified using bottom tagging outside of the tagged top. For t -channel single top production we do not expect a b -tag since the recoil jet corresponds

	tagged	$\cos\theta^* < -0.7$	-0.5	-0.3
t-ch. [fb]	118	45.2	70.5	85.7
QCD [10^3 fb]	40.2	12.8	18.5	20.7
$\epsilon_{S/B}$	1	1.20	1.29	1.40
$\epsilon_{S/\sqrt{B}}$	1	0.67	0.87	1.01
$t\bar{t}$ [fb]	137	13.1	27.9	44.2
$\epsilon_{S/B}$	1	4.01	2.92	2.25
$\epsilon_{S/\sqrt{B}}$	1	1.23	1.32	1.27

Table 4.8: Tagged top rate (in fb for t -channel, QCD and $t\bar{t}$) after several choices for a cuts on the angle $\cos\theta^*$. $\epsilon_{S/B}$ and $\epsilon_{S/\sqrt{B}}$ denote improvement factors relative to the cross sections after applying the cut on system momentum p_{tj} .

to a light quark. Therefore we will require no bottom tag outside the tagged top. Again we assume a tagging efficiency of $\epsilon_b = 50\%$ and a mis-tag rate of $\epsilon_{mis} = 1\%$. The probability for at least one recoil jet to be b -initiated can be seen in the first row of Tab. 4.9. The second row shows the corresponding rate of events that pass the b -veto. We see that about one third of the $t\bar{t}$ -background events can be rejected while almost all signal events pass the b -veto.

process	s-ch.	t-ch.	$t\bar{t}$	$t\bar{t}j$	$t\bar{t}jj$	tW	tbW
correct matching	96.4%	0.55%	59.6%	65.4%	72.4%	8.8%	75.9%
b-tag rejection	51.8%	98.7%	69.8%	66.9%	63.5%	94.7%	61.8%

Table 4.9: Efficiency for bottom rejection in recoil jets for different channels. We consider each channel separately and determine how often a recoil jet is b -initiated. Afterwards we include the b -tagging rate of 50% for correctly assigned b -subjets and a mis-tag rate of 1% for incorrectly assigned subjets.

The cut on the tj -system momentum that we have applied before ensures the top and recoil jet transverse momentum to be balanced. Since we required a minimal transverse momentum for the tagged jet $p_{T,min} = 200$ GeV, we expect the recoil jet to exceed this threshold as well. Therefore, the recoil jet should be embedded in a fat jet where we again use the C/A algorithm with $R = 1.5$ for reconstruction and require $p_{T,fat} > 200$ GeV. In Fig. 4.8 (left) we show the number of fat jets after applying the cuts on the tj -system. In about 90% of the signal and $t\bar{t}$ background events we see a second fat jet besides the fat jet corresponding to the tagged top. Therefore, we can make the requirement to see exactly two fat jets without decreasing the number of signal events significantly.

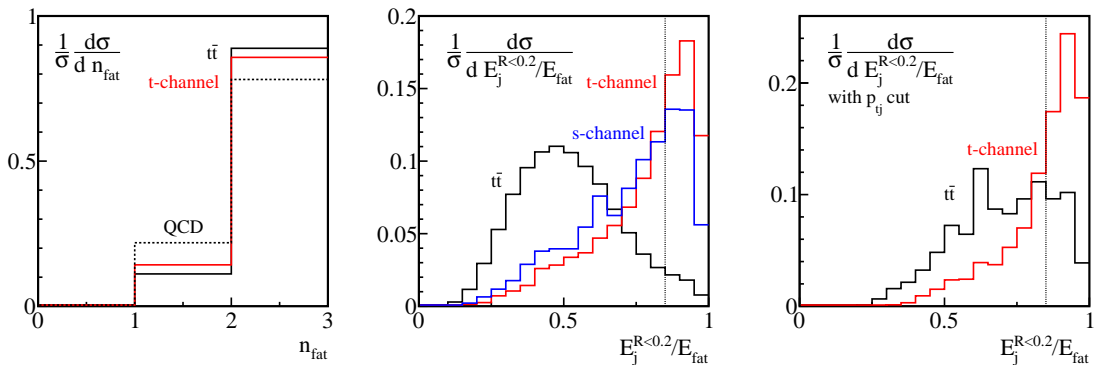


Figure 4.8: Left: Number of C/A fat jets $R = 1.5$ and $p_{T,fj} > 200$ GeV for different processes after cuts on tj -system and b -rejection. Right: Energy ratio $E_j^{R<0.2}/E_{fat}$ before (center) and after (right) cuts on tj -system and b -rejection. We show t -channel (red line), s -channel (blue line), $t\bar{t}$ (black line) and QCD (black dotted line). Figure taken from [41].

To reject even more $t\bar{t}$ background, we use the internal structure of the recoil fat jet. The recoil

jet in single top events is initiated by a light or b -quark and therefore should be narrow. No other energy deposit around it is expected. Therefore the energy of the recoil jet and the fat jet it is embedded in should be the same. For $t\bar{t}$ background the recoil fat jet corresponds to the untagged top but the recoil jet will be just one subjet. Therefore, there should be other energy contributions besides the recoil jet inside the recoil fat jet corresponding to the other decay products. Thus, the energy of the recoil jet will be smaller than the energy of the fat jet it is embedded in. To quantify this we introduce the energy ratio $E_j^{R<0.2}/E_{fat}$ between the energy of the filtered recoil jet $E_j^{R<0.2}$ and the fat jet energy E_{fat} . For filtering we use a jetsize $R = 0.2$ and $n_{filter} = 1$. The energy ratio distribution before and after applying the cuts on the tj -system are shown in Fig. 4.8. Indeed we observe this energy ratio to be large for signal events and small for $t\bar{t}$ background. This behavior does not change significantly if we apply the cut on the tj -system before. Only those $t\bar{t}$ background events will pass the tj -system cut in which one jet carries almost all momentum and therefore can balance the tagged top itself. This results in a shift for the energy ratios towards larger values as we can see in the right panel of Fig. 4.8. In Tab. 4.10 we show the improvement factor for different choices of cuts on $E_j^{R<0.2}/E_{fat}$. The dotted line in Fig. 4.8 corresponds to the most promising choice $E_j^{R<0.2}/E_{fat} > 0.85$.

	tagged	$E_j^{R<0.2}/E_{fat} > 0.8$	0.85	0.9	$m_{jet} < 65$ GeV
t-ch. [fb]	69.6	48.6	40.2	27.8	68.6
QCD [10^3 fb]	18.3	8.58	7.85	5.53	18.3
$\epsilon_{S/B}$	1	1.49	1.35	1.32	0.99
$\epsilon_{S/\sqrt{B}}$	1	1.02	0.88	0.72	0.99
$t\bar{t}$ [fb]	18.7	5.83	3.96	2.41	16.7
$\epsilon_{S/B}$	1	2.24	2.73	3.10	1.10
$\epsilon_{S/\sqrt{B}}$	1	1.25	1.25	1.11	1.05

Table 4.10: Tagged top rate (in fb for t -channel, QCD and $t\bar{t}$) after several choices for a cuts on the energy ratio $E_j^{R<0.2}/E_{fat}$ and the recoil jet mass m_{jet} . $\epsilon_{S/B}$ and $\epsilon_{S/\sqrt{B}}$ denote improvement factors relative to the cross sections after applying the cuts on tj -system and b -rejection.

For $t\bar{t}$ background events the recoil will mostly likely be initiated by the decay products of the tagged top: either the b -quark or the W -boson. We already reduced the number of events in which the recoil jet is b -initiated by applying a bottom tag. To identify the jet as W -initiated, we will look at its mass as shown in Fig. 4.9. For $t\bar{t}$ background events we see a small peak around $m_{jet} = 80$ GeV which corresponds to the W mass. Recoil jets in signal events prefer to have a smaller mass. Therefore we will require $m_{jet} < 65$ GeV. The corresponding improvement factors can be seen in Tab. 4.10.

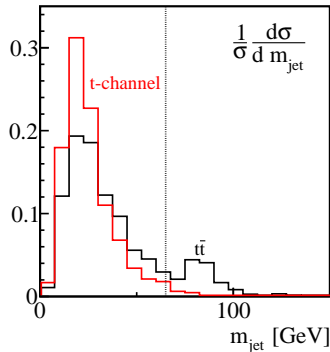


Figure 4.9: Normalized distribution of the recoil jet mass m_{jet} for t -channel (red line) and $t\bar{t}$ (black line) after applying cuts on the tj -system and b -rejection.

Using this cuts on the internal structure we can successfully reject most $t\bar{t}$ events in which the untagged top decays hadronically. Due to a finite efficiency for isolated lepton identification there are some semileptonic $t\bar{t}$ events passing the selection cuts. In such events the neutrino would leave

the detector undetected. Therefore it will cause a missing transverse momentum $p_{T,miss}$. The corresponding distribution for t -channel signal events and $t\bar{t}$ background is shown in the left panel of Fig. 4.10. To further reduce the background we require $p_{T,miss} < 40$ GeV as denoted by the dotted line.

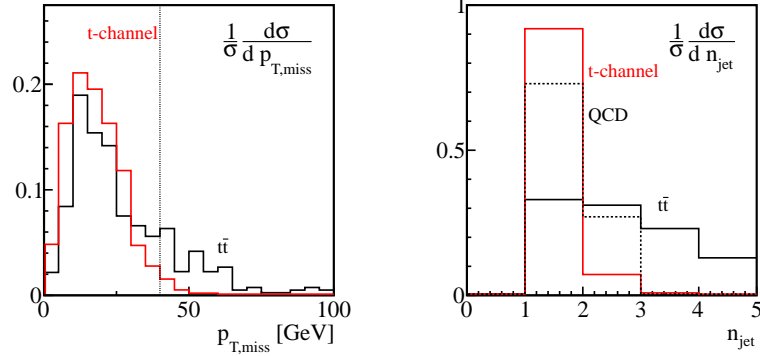


Figure 4.10: Left: Normalized distribution of missing transverse momentum $p_{T,miss}$ after cuts on the tj -system, internal structure of the recoil jet and b -rejection. Right: Normalized distribution of number of recoil jets with $p_T > 25$ GeV after applying all discussed cuts. We show t -channel (red line), $t\bar{t}$ (black line) and QCD (black dotted line).

There are other variables and techniques we could use to reject background events that we want to mention here. In principle we could try to identify τ leptons produced in semileptonic $t\bar{t}$ decays using a τ tagger [91]. Since this is expected to be a small effect we will not discuss it here in detail. Another possibility would be to look at additional jets. After top tagging we cluster the remaining calorimeter cells using C/A algorithm to obtain a set of recoil jets with $p_{t,jet} > 25$ GeV. In our analysis we only used the hardest recoil jet but no additional jets. A distribution for the number of recoil jets after applying all discussed cuts is shown in the right panel of Fig. 4.10. We can see that QCD and $t\bar{t}$ background events prefer to have more than one recoil jet while the single top signal has no additional jets. In principle we can apply a jet veto. This we will not do in our analysis since our detector simulation does not treat effects like underlying events and pile up properly. These would cause additional jets which would change the distribution for number of recoil jets.

4.5 s -channel single top production

As we can see in Fig. 4.1 at LHC 8 TeV the s -channel single top production cross section $\sigma_s = 5.5$ pb is much smaller compared with the t -channel single top and $t\bar{t}$ production cross sections $\sigma_t = 86$ pb and $\sigma_{t\bar{t}} = 234$ pb. Furthermore, in the boosted top regime $p_T > 200$ GeV the cross section ratio $\sigma_s/\sigma_{t\bar{t}} = 0.01$ becomes worse.

To identify the s -channel process we follow the same strategy as for t -channel single top production. We first look at the tagged top itself where we again choose a stronger configuration for the HEPTopTagger. As we can see in Fig. 4.2 and 4.4 the distributions for variables describing the tagged top are almost identical. Therefore, we require a small mass difference between pruned mass and filtered mass as well as a bottom tag inside the b -labeled subjet. This will reject most of the QCD background events.

Compared with the t -channel process the recoil jet in s -channel single top production is b -initiated. Since no other additional jet is produced the recoil jet will still balance the tagged top. Therefore we can use the tj -system momentum cut. Due to the different initial and final state particles the angular correlation between the decay products will change. Since the initial state consists of a light quark and antiquark which have a similar parton distribution function the center-of-mass momentum will not have a preferred direction anymore. Unfortunately the angular distribution of the angle θ^* for the dominant subprocess of s -channel single top production looks similar to the distribution for $t\bar{t}$. This can be seen in Fig. 4.7. We can use this distribution to distinguish both single top production channels. We will require $\cos\theta^* > -0.5$ to reject the t -channel single top

background.

We can check if the recoil jet is b -initiated using a bottom tag. Similar to the b -tag of the b -labeled subjet inside the tagged top, the most promising strategy is to apply only one b -tag inside the hardest recoil jet to minimize the mis-tag probability. This will effectively reject most of the remaining QCD, W +jets and t -channel single top background. This selection cut is also efficient for $t\bar{t}$ since the hardest recoil jet does not always initiated by a b -quark produced in the decay of the untagged top. As shown in Tab. 4.11 half of the s -channel single top events but only about 20 % of the $t\bar{t}$ events will have a b -tag in the recoil jet.

process	s-ch.	t-ch.	$t\bar{t}$	$t\bar{t}j$	$t\bar{t}jj$	tW	tbW
correct matching	99.8%	0.25%	46.2%	35.7%	27.0%	6.0%	51.6%
b-tag efficiency	50%	1.12%	23.6%	18.5%	14.2%	3.96%	26.3%

Table 4.11: Efficiency for bottom tagging in recoil jets for different channels. We consider each channel separately and determine how often a recoil jet is b -initiated. Afterwards, we include the b -tagging rate of 50% for correctly assigned b -subjets and a mis-tag rate of 1% for incorrectly assigned subjets.

After the two bottom tags, which reject t -channel, QCD and W +jets background contributions, the remaining dominant background is top pair production. As before we can reduce this using cuts on the internal structure of the recoil fat jet, the mass of the recoil jet and the missing transverse momentum $p_{T,miss}$. The left panel of Fig. 4.11 shows the distribution of the ratio of the filtered jet energy to the fatjet energy. As we can see the cut $E_j^{R<0.2}/E_{fat} > 0.85$, that we have already used in the previous analysis, effectively reduces the top pair background. Only 2.5% of the $t\bar{t}$ events will pass this cut while about 25% of the signal passes. We will still apply a cut on the jet mass although it turn out to be less effective in the s -channel single top search. Since we require the recoil jet to be b -tagged, the mass distribution will no longer show a peak around the W -mass. The right panel of Fig. 4.11 shows the missing transverse momentum $p_{T,miss}$ distribution after all discussed cuts. We again observe small values of $p_{T,miss}$ for signal events but large values of $p_{T,miss}$ for the top pair background.

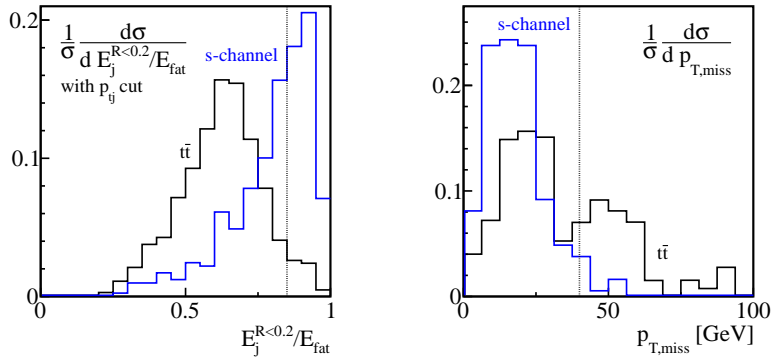


Figure 4.11: Left: Normalized distribution of energy ratio $E_j^{R<0.2}/E_{fat}$ (left) after cut on tj -system momentum and missing transverse momentum $p_{T,miss}$ (right) after all discussed cuts. We show s -channel (blue line) and $t\bar{t}$ (black line).

Chapter 5

Results of event selection

In the previous chapters we analyzed the event topology for single top signal and major background processes. This led us to distributions for kinematic variables that motivated the several selection cuts which can be used to distinguish signal from background events. We want to measure the s -channel and t -channel single top production cross section separately. Therefore we have developed two separate strategies to identify the production process. As background we consider QCD jets, W +jets, $t\bar{t}$ +jets and $tW(b)$ single top production, where QCD and $t\bar{t}$ turn out to be the dominant background contributions. To get a more realistic description we use the detector simulation Delphes. The results of this analysis for both single top production channels will be presented for the LHC at 8 and 14 TeV.

5.1 t -channel at $\sqrt{s} = 8$ TeV

At first we will focus on t -channel single top production at the 8 TeV LHC and summarize the selection cuts we apply. The expected cross sections after successive cuts for the signal and background processes are summarized in Tab. 5.1. In the first two lines we again present the theoretical cross sections used for the analysis result of a preselection for hadronic events with two fat jets.

1. **preselection:** The HEPTopTagger is designed to detect hadronically decaying tops. Therefore we will veto all events which contain isolated leptons. Furthermore, we require each event to have two C/A $R = 1.5$ fat jets with $p_{T,fat} > 200$ GeV. These correspond to the top and recoil jets. In Fig. 4.8 we have seen that after cuts on the tj -system the recoil jet is embedded in a recoil fat jet in about 90 % of the events. Therefore we will require two fat jets at the beginning.

$$n_\ell = 0, \quad n_{fat} = 2 \quad (5.1)$$

At this stage QCD jets turn out to be the major background. In the next step we require one of the fat jets to be top-tagged using the HEPTopTagger. The next three lines of Tab. 5.1 (step 2 - 4) concern the internal structure of the tagged top itself.

2. **one top tag:** We will require exactly one tagged top in the event. We veto events with more than one top tag to avoid contamination from $t\bar{t}$. For top tagging we use the default configuration of the HEPTopTagger but with modified cuts on the mass plane variables and filtered top mass to enhance QCD rejection. We choose

$$\frac{m_{23}}{m_{123}} = \frac{m_W}{m_{top}} \pm 10\%, \quad \arctan \frac{m_{13}}{m_{12}} > 0.45 \quad (5.2)$$
$$160 \text{ GeV} < m_{top} < 200 \text{ GeV}.$$

3. **pruned mass:** As we have seen in the previous discussion we can use the pruned mass to distinguish events including tops from QCD background events. Since pruning discards less constituents of the fat jet compared to filtering, we expect the pruned mass m_{prune} to be larger than the filtered mass m_{filter} . This effect increases in a busy jet environment such as

QCD. Therefore the difference between pruned mass and filtered mass is larger in QCD than in events containing a top. We will require a small mass difference of

$$\Delta m_{prune} = m_{prune} - m_{filter} < 20 \text{ GeV}. \quad (5.3)$$

4. ***b*-tag in top:** Additionally we require the subjet of the tagged top that is labeled as *b*-initiated by the tagging algorithm to be *b*-tagged. This efficiently reduces the QCD and *W*+jets background.

Using a top tag and cuts on its internal structure sufficiently reduces QCD background. For events including a top quark we observe an efficiency of 3%. QCD jet events are reduced by a factor of $1.5 \cdot 10^{-5}$. Up to this step we achieve $S/\sqrt{B} = 5.41$ for 10 fb^{-1} . Although this would be enough to measure this process we still have a bad signal over background ratio $S/B = 0.06$. This is caused by the $t\bar{t}$ production which turns out to be the dominating background at this step as we can see in Tab. 5.1.

Once we have identified the top, we concentrate on the system containing the tagged top and the recoil jet. To identify the recoil jet, we cluster the remaining calorimeter cells that we have not used to reconstruct the tagged top using the C/A algorithm with $R = 0.5$. We obtain a set of jets and choose the hardest jet to be the recoil jet. The cuts and corresponding cross sections can be seen in the next two lines (step 5 and 6) of Tab. 5.1.

5. ***tj*-system momentum p_{tj} :** In single top decay the recoil jet is expected to balance the tagged top. Therefore the transverse momentum of the system consisting of the tagged top and the recoil jet, $p_{T,tj}$, should be small. The initial state for single top decay consists of a light quark and a *b*-quark for *t*-channel and an anti-quark for *s*-channel single top production. Since the light quark PDF is harder than the *b* or anti-quark PDF, we expect the system to be boosted in the direction of the light quark. Therefore we will observe large longitudinal momentum $p_{L,tj}$ for the *tj*-system. In top pair production, the recoil jet will correspond to a decay product of the untagged top and therefore not be able to balance the tagged top. Furthermore there is no special reason for large longitudinal *tj*-system momentum. Therefore we observe large $p_{T,tj}$ and small $p_{L,tj}$. To enhance the single top signal and reduce top pair background we require

$$p_{T,tj} < 10 \text{ GeV} + \frac{p_{L,tj}}{60}. \quad (5.4)$$

6. **angular correlation:** In *t*-channel single top decay the *tj*-system momentum will point in the direction of the incoming light quark. Therefore we are able to measure the decay angle θ^* which is defined as the angle between the top momentum in the *tj*-systems rest frame and the direction of the *tj*-system in the lab frame. Due to the kinematics of *t*-channel single top decay we expect large angles θ^* . For top pair production there is no preferred direction of the center-of-mass momentum. Furthermore the *tj*-system momentum tends to point in the top direction what leads to small angles θ^* . Therefore we require

$$\cos \theta^* < -0.5 \quad (5.5)$$

Using these cuts we obtain 8.6 fb signal events against 2.2 fb $t\bar{t}$ and 3.8 fb QCD background as we can see in step 6 in Tab. 5.1. The other background turn out to be negligible. We achieve a signal over background ratio $S/B = 1.28$ and $S/\sqrt{B} = 10.6$ for 10 fb^{-1} .

If we want to further reduce $t\bar{t}$ background we can apply cuts on the internal structure of the recoil jet.

7. ***b*-veto in recoil jet:** The recoil jet in the *t*-channel single top signal is initiated by a light quark while we expect to see at least one recoil jet in $t\bar{t}$ initiated by a *b*-quark coming from the decay of the untagged top. Therefore we will require a *b*-veto for recoil jets.
8. **internal structure of the recoil jet:** The recoil jet itself has a large transverse momentum and therefore forms a fat jet. For single top decay this recoil jet should contain only one narrow jet corresponding to the recoil jet. For top pair production the recoil fat jet corresponds to the untagged top and is expected to contain more than one subjet. Therefore we compute the energy fraction of the filtered recoil jet using $R_{filter} = 0.2$ and the fat jet energy and

require it to be large. Furthermore we require the mass of the recoil jet to be small to reject *W*-initiated recoil jets.

$$E_j^{<0.2}/E_{fat} > 0.85, \quad m_{jet} < 65 \text{ GeV} \quad (5.6)$$

9. **missing transverse momentum** $p_{T,miss}$: In our analysis we assumed a finite isolated lepton identification and no tau identification. Therefore some of the remaining $t\bar{t}$ events include leptonically decaying tops. These can be rejected by requiring a small missing transverse momentum

$$p_{T,miss} < 40 \text{ GeV} \quad (5.7)$$

The last set of cuts reduces the top pair background by a factor of 10 while letting 50 % of the signal events pass. Combining all suggested cuts we can reject almost all $t\bar{t}$ events and achieve $S/B = 2.38$ and $S/\sqrt{B} = 10.9$ for 10 fb^{-1} . We see that the first set of cuts concerning the tagged top successfully reduces QCD background while the cuts on the tj -system and the structure of the recoil jet mainly reduce top pair background. Depending on the required signal over background ratio it may be possible to only apply the cuts described in step 1 to 6.

number of events	<i>t</i> -ch.	<i>s</i> -ch.	$t\bar{t}$	$tW(b)$	QCD	<i>W</i> +jets	S/B	S/\sqrt{B}
0. cross section [pb]	87.2	5.55	234	40.6	$6.58 \cdot 10^5$	$1.57 \cdot 10^3$	–	–
1. preselection [eq.(5.1)] [pb]	1.57	0.23	18.8	1.63	$6.67 \cdot 10^3$	48.1	0.0002	1.91
2. one top tag [eq.(5.2)] [fb]	204	28.2	3069	227	$6.4 \cdot 10^4$	1297	0.0029	2.46
3. pruned mass [eq.(5.3)] [fb]	110	13.9	1422	102	9707	529	0.0093	3.21
4. <i>b</i> -tag in top [fb]	44.3	5.29	524	37.4	97.1	5.29	0.066	5.41
5. p_{tj} cut [eq.(5.4)] [fb]	14.7	1.24	12.1	1.17	11.0	1.10	0.55	9.02
6. $\cos\theta^*$ cut [eq.(5.5)] [fb]	8.52	0.08	2.20	0.15	3.85	0.19	1.31	10.6
7. <i>b</i> -veto in recoil jet [fb]	8.41	0.04	1.49	0.12	3.81	0.18	1.49	11.2
8. recoil jet [eq.(5.6)] [fb]	5.08	0.02	0.34	0.02	2.00	0.08	2.05	10.2
9. $p_{T,miss}$ cut [eq.(5.7)]	4.94	0.02	0.26	0.02	1.67	0.08	2.38	10.9

Table 5.1: Number of events for 8 TeV LHC that pass the selection cuts optimized for *t*-channel single top search. The significance values are quoted for *t*-channel single top production assuming the other processes as backgrounds. S/\sqrt{B} is for 10 fb^{-1} . We take *b*-(mis)tag efficiency as 50% (1%) for *b*-quark (light quarks).

5.2 *s*-channel at $\sqrt{s} = 8$ TeV

Let us now have a look at *s*-channel single top production at LHC 8 TeV. The expected cross sections after successive cuts for the signal and background processes are summarized in Tab. 5.2. Again in the first two lines we show the theoretical cross section and the cross section after the preselection using a lepton veto and requiring two fat jets.

Again we first look at the internal structure of the tagged top where we apply the same cuts as discussed for the *t*-channel single top production (see step 2 - 4 in Tab. 5.2). The resulting signal over background ratio is much smaller since the *s*-channel single top production cross section is small compared with all other considered processes. The dominant background processes are $t\bar{t}$, QCD and *t*-channel single top production.

Again we expect a large longitudinal momentum but a small transverse momentum for the tj -system. Therefore we apply the same selection cut on the tj -system momentum as described in step 5. Differences in the kinematics between the two single top production channels can be seen in the angular correlation. Furthermore we can use that the recoil jet is *b*-initiated.

- 6(s). **angular correlation:** As we have seen in the analysis of the decay angles for *s*-single top production the center-of-mass momentum does not have a preferred direction anymore. The position of the peak for the angle $\cos\theta^*$ depends on the initial state particles. For the dominant subprocess the distribution of $\cos\theta^*$ looks similar to the $t\bar{t}$ background. But we can still use this angle to distinguish *s*-channel and *t*-channel single top production. Therefore we require

$$\cos\theta^* > -0.5 \quad (5.8)$$

- 7(s). ***b*-tag in recoil jet:** The recoil jet in the *s*-channel single top signal is initiated by a *b*-quark. Therefore we will require a *b*-veto for the recoil jets. Since we only look at the hardest recoil jet instead of the whole set of recoil jets we can reject $t\bar{t}$ events in which the *b*-subjett produced in the decay of the untagged top is not the hardest jet.

The selection cuts on the internal structure of the recoil jet and the missing transverse momentum apply for both single top channels and can be used as presented in step 8 and 9. We see that *b*-tagging inside the recoil jet successfully reduces QCD and *t*-channel single top background. The remaining $t\bar{t}$ background is sufficiently reduced by the cut on the internal structure. We finally achieve $S/B = 1.96$ and $S/\sqrt{B} = 2.23$ for 10 fb^{-1} . Although the signal over background ratio looks promising the expected number of observed signal events is very small. Therefore the resulting value for S/\sqrt{B} is not enough to claim an observation of this process.

number of events	<i>t</i> -ch.	<i>s</i> -ch.	$t\bar{t}$	$tW(b)$	QCD	<i>W</i> +jets	S/B	S/\sqrt{B}
0. cross section [pb]	87.2	5.55	234	40.6	$6.58 \cdot 10^5$	$1.57 \cdot 10^3$	–	–
1. preselection [eq.(5.1)] [pb]	1.57	0.23	18.8	1.63	$6.67 \cdot 10^3$	48.1	0.0002	1.91
2. one top tag [eq.(5.2)] [fb]	204	28.2	3069	227	$6.4 \cdot 10^4$	1297	0.0004	0.34
3. pruned mass [eq.(5.3)] [fb]	110	13.9	1422	102	9707	529	0.0011	0.40
4. <i>b</i> -tag in top [fb]	44.3	5.29	524	37.4	97.1	5.29	0.0074	0.62
5. p_{tj} cut [eq.(5.4)] [fb]	14.7	1.24	12.1	1.17	11.0	1.10	0.031	0.61
6s. $\cos \theta^*$ cut [eq.(5.8)] [fb]	6.21	1.16	9.95	1.02	7.16	0.91	0.045	0.72
7s. <i>b</i> -veto in recoil jet [fb]	0.06	0.58	2.07	0.15	0.07	0.01	0.244	1.19
8. recoil jet [eq.(5.6)] [fb]	0.03	0.26	0.11	0.01	0.01	–	1.59	2.04
9. $p_{T,miss}$ cut [eq.(5.7)]	0.03	0.25	0.07	0.01	0.01	–	1.97	2.23

Table 5.2: Number of events for 8 TeV LHC that pass the selection cuts optimized for *s*-channel single top search. The significance values are quoted for *s*-channel single top production assuming the other processes as backgrounds. S/\sqrt{B} is for 10 fb^{-1} . We take *b*-(mis)tag efficiency as 50% (1%) for *b*-quark (light quarks).

5.3 Single top at $\sqrt{s} = 14 \text{ TeV}$

After a shutdown LHC is planned to reopen in 2014 with a larger center-of-mass energy of 14 TeV. Therefore we also analyze the perspective of single top search results at a 14 TeV run of the LHC. For this run we expect a larger integrated luminosity and therefore more data. Due to the larger beam energy the cross sections for all relevant processes will be larger but the event topology stay similar. Therefore we will use the same selections cuts as in the analysis for LHC 8 TeV.

number of events	<i>t</i> -ch.	<i>s</i> -ch.	$t\bar{t}$	$tW(b)$	QCD	<i>W</i> +jets	S/B	S/\sqrt{B}
0. cross section [10^2 pb]	2.48	0.118	9.20	1.60	$1.94 \cdot 10^4$	38.8	0.0003	–
1. $n_\ell = 0$ with 2 fat jets [pb]	6.59	0.670	95.3	10.2	$2.83 \cdot 10^4$	129	0.0004	–
2. one top tag [eq.(5.2)] [fb]	819	81.4	14820	1350	$3.00 \cdot 10^5$	3015	0.0026	4.58
3. pruned mass [eq.(5.3)] [fb]	416	40.4	6439	578	$3.60 \cdot 10^4$	1005	0.0094	6.26
4. <i>b</i> -tag in top [fb]	166	15.5	2347	211	360	10.0	0.056	9.69
5. p_{tj} cut [eq.(5.4)] [fb]	64.5	3.80	73.0	8.23	41.4	2.40	0.50	18.0
6. $\cos \theta^*$ cut [eq.(5.5)]	41.0	0.32	17.4	1.30	12.5	0.62	1.28	22.9
7. <i>b</i> -veto in recoil jet [fb]	40.5	0.16	11.6	1.04	12.3	0.61	1.57	25.2
8. recoil jet [eq.(5.6)] [fb]	22.2	0.08	2.36	0.14	5.36	0.32	2.68	24.4
9. $p_{T,miss}$ cut [eq.(5.7)]	20.3	0.08	1.69	0.12	3.7	0.31	3.42	26.35

Table 5.3: Number of events for 14 TeV LHC that pass the selection cuts optimized for *t*-channel single top search. The significance values are quoted for *t*-channel single top production assuming the other processes as backgrounds. S/\sqrt{B} is for 10 fb^{-1} . We take *b*-(mis)tag efficiency as 50% (1%) for *b*-quark (light quarks).

In Tab. 5.3 we show the cross sections after the successive cuts for *t*-channel single top described in the previous section. Again, we preselect hadronic events with two fat jets. Using the modified

setting for the HepTopTagger we get a tagging efficiency of 12% for single top, 15% for $t\bar{t}$ and a mis-tag rate of 1% for QCD background events. This is similar to the result for 8 TeV. If we additionally apply a cut on the pruned mass and require a b -tag inside the top quark we can reduce QCD background by a factor of 0.12% and W +jets background by a factor of 0.3% while keeping 20% of the signal events. As we can see in step 4 of Tab. 5.3 we achieve a $S/B = 0.056$ and $S/\sqrt{B} = 9.69$ for 10 fb^{-1} .

The dominant remaining background after top tagging and cuts on the tagged top is top pair production. Again this can be reduced by applying cuts on the tj -system. We achieve $S/B = 1.28$ and $S/\sqrt{B} = 22.9$ for 10 fb^{-1} as shown in step 6 in Tab. 5.3. If we want to further reduce the top pair background we can apply cuts on the internal structure of the recoil jet and on the missing transverse momentum and a b -veto for the recoil jet. As shown in step 9 of Tab. 5.3 we achieve a $S/B = 3.42$ and $S/\sqrt{B} = 26.35$ for 10 fb^{-1} .

In the analysis for s -channel single top at 14 TeV we have to take into account the transverse momentum distribution. Compared with LHC 8 TeV the boosted cross sections becomes three times larger for the s -channel but five times larger for $t\bar{t}$. Since $t\bar{t}$ is the main background process we expect a smaller signal over background ratio compared with LHC 8 TeV. In Tab. 5.4 we show the corresponding cross sections after the same cuts discussed in the previous section. The QCD background is rejected efficiently requiring two b -tags in the tagged top and the recoil jet while cuts on the tj -system and the recoil jet reduce $t\bar{t}$ background. Finally we achieve $S/B = 1.29$ and $S/\sqrt{B} = 3.02$ for 10 fb^{-1} as shown in step 9 in Tab. 5.4. Compared with the result of the LHC 8 TeV analysis the final signal over background ratio differs by a factor of 3/5 as expected from the boosted top cross sections. Again the expected cross section after applying all cuts is small. A large integrated luminosity is needed to improve s -channel single top production at LHC 14.

number of events	t -ch.	s -ch.	$t\bar{t}$	$tW(b)$	QCD	W +jets	S/B	S/\sqrt{B}
0. cross section [10^2 pb]	2.48	0.118	9.20	1.60	$1.94 \cdot 10^4$	38.8	0.0003	–
1. $n_\ell = 0$ with 2 fat jets [pb]	6.59	0.670	95.3	10.2	$2.83 \cdot 10^4$	129	0.0004	–
2. one top tag [eq.(5.2)]	819	81.4	14820	1350	$3.00 \cdot 10^5$	3015	0.0002	0.45
3. pruned mass [eq.(5.3)] [fb]	416	40.4	6439	578	$3.60 \cdot 10^4$	1005	0.0009	0.60
4. b -tag in top [fb]	166	15.5	2347	211	360	10.0	0.0050	0.88
5. p_{tj} cut [eq.(5.4)] [fb]	64.5	3.80	73.0	8.23	41.4	2.40	0.020	0.87
6s. $\cos \theta^*$ cut [eq.(5.8)] [fb]	23.5	3.48	55.6	6.93	29.0	1.78	0.030	1.02
7s. b -veto in recoil jet [fb]	0.24	1.73	11.5	0.75	0.29	0.02	0.14	1.53
8. recoil jet [eq.(5.6)] [fb]	0.11	0.75	0.52	0.05	0.10	–	0.96	2.68
9. $p_{T,miss}$ cut [eq.(5.7)]	0.11	0.71	0.32	0.02	0.10	–	1.29	3.02

Table 5.4: Number of events for 14 TeV LHC that pass the selection cuts optimized for s -channel single top search. The significance values are quoted for s -channel single top production assuming the other processes as backgrounds. S/\sqrt{B} is for 10 fb^{-1} . We take b -(mis)tag efficiency as 50% (1%) for b -quark (light quarks).

Chapter 6

Conclusion and Outlook

In this thesis we have studied fully hadronic single top searches at LHC. We have developed a strategy to identify s -channel and t -channel single top production separately. In our analysis we use the HEPTopTagger as a tool to identify top quarks inside geometrically large jets. It focuses on moderately boosted top quarks $p_{T,top} > 200$ GeV. In this regime the detected fat jet has a manageable size and a good subjet resolution. The fat jets substructure is used to identify the top decay products. This information is used to distinguish top initiated fat jets from QCD background events. In the moderately boosted regime the HEPTopTagger has a tagging efficiency of 12 – 15% and a mis-tag rate of 1%.

In the second part of this thesis we derived the leading order cross section for both single top production channels. We have seen that there is no interference between both productions channels at LO and NLO. Due to gluon emission at NNLO such an interference would be possible. At this order the cross section for s -channel single top production is much smaller than the t -channel production cross section and will therefore be harder to measure. To describe the signal processes we focus on their leading order contributions. We have seen that the distribution for the scattering angle appearing in the differential cross section differs for both channels. We have invented a way to measure the scattering angle for single top production directly using the features of the initial state particles parton distribution function. The scattering angle can be used to distinguish the t -channel process from s -channel single top production and top pair production.

We have simulated all relevant signal and background processes using Alpgen and Pythia. Applying successive cuts we have shown that it is possible to distinguish signal from background events, where $t\bar{t}$ and QCD were shown to be the major background contributions. In the first step we require one top tag with an additional b -tag and a small mass difference between the filtered and pruned mass of the tagged top. This provides a factor of 2000 rejection against the QCD background. In the next step we apply a cut on the momentum of the system consisting of the tagged top. This is possible since the HEPTopTagger provides the reconstructed top momentum. This provides a factor 10 rejection against $t\bar{t}$ and a factor 2 against QCD.

For the t -channel analysis we additionally require a small scattering angle. We achieve $S/B > 1$ and $S/\sqrt{B} > 10$ for 10 fb^{-1} integrated luminosity as shown in Tab. 5.1. If we want to further reduce background coming from top pair production we should apply additional cuts on the internal structure of the recoil jet and on the missing transverse momentum and apply a b -veto for the recoil jets to achieve $S/B > 2$. Using the same analysis we achieve $S/B > 3$ and $S/\sqrt{B} > 25$ for 10 fb^{-1} for the 14 TeV run of LHC.

To detect s -channel single top production we require an additional b -tag in the recoil jet which rejects most of the remaining QCD background. Top pair and t -channel single top production can be rejected using cuts on the scattering angle, the internal structure of the recoil jet and the missing transverse momentum. Finally we achieve $S/B > 1$ with a 2.2σ significance 10 fb^{-1} integrated luminosity at LHC 8 TeV. For the 14 TeV run we get similar results. A 5σ significance is expected at 25 fb^{-1} integrated luminosity.

In our analysis we have used the fast detector simulation Delphes. The next step would be to analyze the obtained results using a full detector simulation. This would include effects of the trigger, a precise description of the detector taking into account realistic detector efficiencies and

pile up. Finally, the aim is to measure the single top production cross section. This would allow us to test the CKM matrix element V_{tb} and therefore the unitarity of the CKM matrix. Furthermore the top quark is the only quark which decays before hadronization. Therefore it gives us the unique possibility to probe properties of a free quark. An example would be spin correlations as described in [62].

Due to its large mass the top quark is also an ideal probe for physics beyond the Standard Model. If the measured cross section differs from its predicted value this would be a hint towards new physics. Therefore the next step is to repeat the analysis assuming new physics models to check if they can be proven or excluded at LHC.

Acknowledgments

At first I want to thank Tilman for giving me the opportunity to work on this very interesting project and for his advice. Furthermore I would like to give special thanks to my collaborator Michi who spend a lot of time explaining our code and answering all the questions I had - especially at the beginning. Whenever I had a problem in physics or with the computer he showed me how to solve it. In addition I want to thank Cathy, David, Dorival, Jamil and Peter for their advice, help and the good time we had during all the lunch breaks and "cake with nut" sessions. Moreover I want to thank the people in the Westzimmer for all the nice discussions and the Institute for Theoretical Physics for providing interesting seminars that gave me an overview about current research topics. I also want to thank our Institute and BWGrid for providing the infrastructure necessary for my work. Furthermore I want to mention the Friedrich-Ebert-Foundation which supported me during my Bachelor and Master studies. Last but not least I want to thank my flatmates Sarah and Jens who prepared nice dinners for me when I stayed long in the institute.

Appendix A

Delphes

A.1 What Delphes does

In the first applications of the HEPTopTagger [37, 38, 40] we have only used data coming from a Monte Carlo Simulation as input for our top tagger. This information is much more precise than what could be realistically measured at a collider experiment. To get more realistic estimates of the expected signal signatures and their associated backgrounds, we need to simulate a detector before applying the top tagger. This is done by Delphes [87] which is a framework for fast simulation of collider experiments.

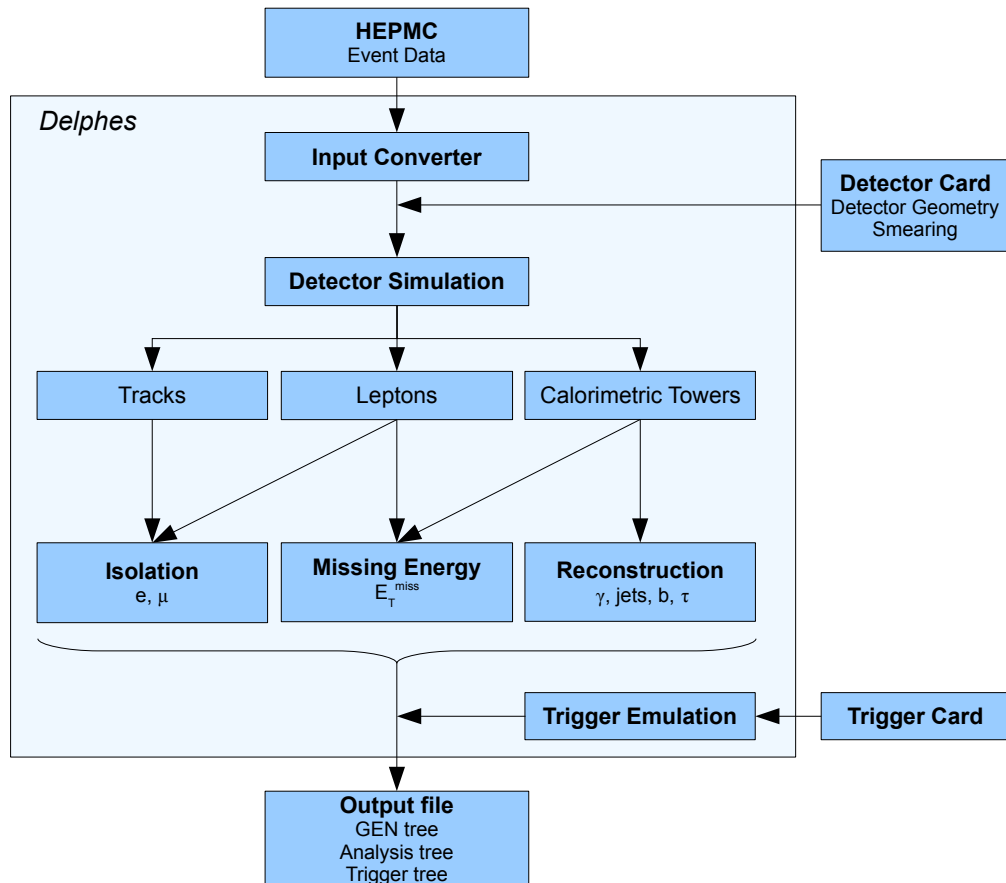


Figure A.1: Flow chart describing the principles behind Delphes

Delphes is not a full detector simulation. Therefore it does not include transport of particles through the detector material, various detector inefficiencies, dead material or geometrical details. But it provides a simulation of the detector including effects of the magnetic field, the granularity of the calorimeter resolution and the smearing of the final state particle kinematics. The mode of operation of Delphes shown in Fig. A.1 contains the most important experimental features we will use later in our analysis:

Coverting input file: For the event simulation we use HEPMC [92]. Delphes reads this information and fills it into the output Root file.

Geometry of the detectors: The layout of a generic detector in Delphes consist of three parts. The innermost part is a central tracking system. This is surrounded by a calorimeter consisting of hadronic and electromagnetic sections. The outer layer is a muon detector. There may be additional forward detectors, but we will not use them in our further analysis. Furthermore Delphes provides a detector card for all common detectors that contain a specific geometry. It is assumed that the segmentation for the hadronic and electromagnetic calorimeters are the same and that the detector is symmetric in ϕ . In our analysis we use the detector card for ATLAS. All detectable particles within the calorimeter volume (except muons) will activate a certain calorimeter cell and the corresponding energy is stored. The ratio between hadronic and electromagnetic energy deposited also get stored as they will be smeared differently later on. If different particles activate the same cell, their energy gets merged.

Smearing: For each calorimetric cell the energy is smeared according to a Gaussian distribution with variance σ satisfying

$$\frac{\sigma}{E} = \frac{S}{\sqrt{E}} \oplus \frac{N}{E} \oplus C \quad (\text{A.1})$$

where S , N and C describe stochastic, noise and constant terms that contribute to the smearing. \oplus means quadratic addition. These numbers are provided in the detector card.

Tracking system: The effects of the magnetic field in the detector are simulated for every charged particle within the tracking system. This provides a track that we store for later analysis. Details about the tracking system are specified in the detector card.

Leptons: The information about electrons and muons are computed and stored separately from the calorimeter data based on the generated data. Each particle get smeared separately from the calorimeter data. An isolation criteria using the track information is applied.

Reconstruction: Using the calorimeter data Delphes can reconstruct jets using the most common reconstruction algorithms. A b-tagging and τ -tagging algorithm is applied. We will not use this information later on. In addition, the missing transverse energy, E_T^{miss} , is calculated.

Trigger emulation: Delphes provides a trigger emulation that is characterized through a trigger card. We do not use it.

Generating output file: The processed data and the trigger information is stored in the output Root file.

A.2 Isolated leptons

The W -boson coming from the top decay can either decay hadronically into two quarks or leptonically into a lepton and a neutrino. If one W -boson decays leptonically we will be not able to reconstruct this boson and therefore the corresponding top quark since we can not detect a neutrino. Even if we would have a lucky situation in which the leptonically decaying top would be tagged we would expect an incorrect momentum of the tagged top due to the missing neutrino information. This momentum would not be useful for later analysis. Therefore we want to avoid

such mis-tagging. This can be done using information about isolated leptons. For semileptonic top pair production we will remove the lepton contribution from the HEPTopTagger input and for the detection of single top decay we will use a lepton veto.

Delphes treats the leptons independently from the calorimeter data. Their momenta is smeared according to the detector card. In Delphes a lepton is considered as isolated if there is no track of another charged particle with transverse momentum bigger than a certain threshold $p_T > p_{T,min}$ within a cone of ΔR [87]. For the ATLAS detector we use $p_{T,min} = 10$ GeV and $\Delta R = 0.5$.

Let us now concentrate on semileptonic top pair production. In this case we might be able to tag the hadronically decaying top. We know that a detected lepton cannot be part of the hadronically decaying top. If we want to use the Delphes calorimeter data as an input for the HEPTopTagger, we need to make sure that there are no contributions from isolated leptons in the calorimeter data. Such a signal could be used during the reconstruction algorithm and therefore contaminate our results.

Since Delphes provides us the position of the isolated leptons, we can simply remove all calorimeter data around the isolated leptons. Therefore we reconstruct jets with the calorimeter data using the C/A algorithm with a cone of $R = 0.5$ and a $p_{T,min} = 10$ GeV. If there is an isolated lepton in the calorimeter data, there should be a reconstructed jet that describes this lepton. If one of the jets and the isolated lepton have a $\Delta R < 0.25$ we can identify this jet as the isolated lepton and we remove all calorimeter information contributing to the jet. To analyze the behavior of this procedure we look at events with one isolated electron or muon and we define the following four cases

- Case 1:** an isolated lepton is detected and it is removed from the calorimeter data
- Case 2:** an isolated lepton is detected but it is not removed from the calorimeter data
- Case 3:** a nonisolated lepton is detected
- Case 4:** no lepton is detected

The corresponding distribution is shown in Tab. A.1. Fig. A.2 shows the ratio of energy stored in the calorimeter around a parton level lepton and the parton-level lepton itself.

particle	total cross section	case 1	case 2	case 3	case 4
muons [pb]	46.1	0.97 (2.1%)	25.4 (55.3%)	11.1 (24.0%)	8.56 (18.5%)
electrons [pb]	46.0	26.2 (57.0%)	0.06 (0.001%)	11.0 (23.9%)	8.77 (19.0%)

Table A.1: Cross section in fb of single isolated parton level leptons in different cases. These numbers are based on semileptonic $t\bar{t}$ events. Percentages are relative to the total cross section of single isolated parton level leptons.

Electrons that enter the detector will leave all of their energy in the calorimeter. Therefore the ratio of energy stored in the calorimeter around the lepton is the same as the parton level energy that we see in the curves for case 1 and 2 in the left plot in Fig. A.2 has a peak around $E_{deposit} \approx E_{parton}$. Furthermore we see in Tab. A.1 that in almost all events in which Delphes detects an isolated lepton, it is possible to remove the corresponding energy deposit in the calorimeter and the electrons are characterized by case 1.

For muons the situation is different. Muons cross the calorimeter and will be detected in a muon detector that encloses the central detector. Therefore the energy deposit in the calorimeter around a parton level muon is small compared to the muon energy. The central plot of Fig. A.2 shows the muon distribution which has a peak around $E_{deposit} \approx 0$. However, in a few events (about 2%) the muon will leave a signal in the calorimeter that we can remove. Most detected isolated muons are therefore describes by case 2.

About 24 % of the leptons are described by case 3 (see Tab. A.1). Since another charged particle is close to the lepton, it is detected as a nonisolated lepton. For both muons and electrons we can observe that the peak for case 3 is slightly shifted to a higher energy ratio and for high ratios it decays slower than case 1 and 2. Since we can not remove this energy deposit it will contaminate our results.

Finally case 4 describes the leptons that are not detected by Delphes due to a p_T cut and an η cut that are caused by the detector geometry as well as an overall detector efficiency of 90% for

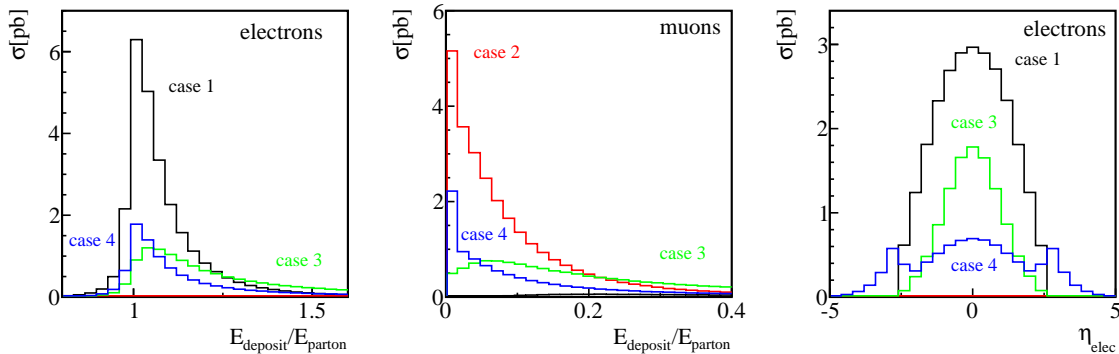


Figure A.2: Energy deposit in the calorimeter within a cone of $\Delta R = 0.5$ around the isolated lepton divided by the energy of the parton level isolated lepton for muons (left) and electrons (central). Right: eta distribution for the parton level isolated electrons. We show case 1 (black), case 2 (red), case 3 (green) and case 4 (blue).

electrons and muons. The effect of the η cut we can see in the right plot of Fig. A.2.

We are also interested in the detection of t -channel single top production. Since we want to tag the top using the HEPTopTagger we have to look at hadronically decaying tops. Therefore we can use the information about isolated leptons to reject (semi-) leptonic $t\bar{t}$ background. In that case we do not have to worry anymore about removing the lepton energy deposited in the calorimeter. In Tab. A.2 we show the correlation between classification as a leptonic or hadronic event before and after using Delphes for top pair production and single top production.

$t\bar{t}$	hadronic (Del)	leptonic (Del)	s -channel	hadronic (Del)	leptonic (Del)
hadronic [pb]	135 (58 %)	5.5 (2.4 %)	hadronic [pb]	4.21 (76 %)	0.095 (1.7 %)
leptonic [pb]	36.5 (15 %)	56 (24 %)	leptonic [pb]	0.48 (8.8 %)	0.75 (13.5 %)

Table A.2: Correlation between events identified as hadronic or leptonic after using Delphes and in parton level for $t\bar{t}$ (left) and s -channel (right) at LHC 8 TeV. Percentages are relative to the total cross section.

We can see that both in single top production and top pair production about 60% events with a leptonically decaying W -boson will be detected as leptonic events. That means that about 11% of the single top events that are actually detected as hadronic are leptonic in parton level. In $t\bar{t}$ production this fraction is 25%. This is due to the fact that there are two tops in the event. Since the momentum of the neutrino is not accessible in most cases, these misidentified events will fail top tagging. In about 2% of events it happens that Delphes detects a hadronic event as leptonic. Since Delphes does not provide fake leptons, this effect can be explained by misidentification of nonisolated leptons as isolated leptons.

A.3 Tagging behavior

Now we can use the calorimeter data provided by Delphes as an input for our tagger. Then we can compare the tagged tops using and not using Delphes event by event. We will do this with a semileptonic $t\bar{t}$ sample using the default configuration of the HEPTopTagger [37].

To analyze the tagging behavior under Delphes in detail we distinguish three cases of tagged tops based on the correspondence between subjects in the tagged top jet and decay products of the parton level top in the Monte Carlo data (see [39]). We have 6...8 constituents in parton level namely the three decay products for each of the two tops and 0...2 additional jets. Now we look at which of these constituents the three subjects used in the reconstruction correspond to. That means we are looking for the combination $\{j_i\}$ of constituents that minimizes the distance measure $\sum_{i=0}^3 \Delta R^2(p_i^{\text{subject}}, p_{j_i}^{\text{constituent}})$. Therefore we introduce three types of tagged tops.

type 1: all subjects correspond to constituents coming from one top decay

type 2: the two hardest subjets correspond to constituents coming from one top decay, the third constituent has another origin: either the other top or an additional jet

type 3: others

If we categorize all events as one of these three types and include the case that no top is detected, we get the distribution shown in Tab. A.3. At first we can see that the usage of a detector simulation preserves the type of the top. This happens in about 95% of all events in which a top is detected both with and without the detector simulation.

top type	type 1 (Del)	type 2 (Del)	type 3 (Del)	no tagged top (Del)
type 1 [fb]	1210 (1.49%)	14.6 (0.02%)	17.7 (0.02%)	629 (0.77%)
type 2 [fb]	9.07 (0.01%)	172 (0.21%)	12.5 (0.02%)	183 (0.22%)
type 3 [fb]	9.94 (0.01%)	12.2 (0.02%)	83.6 (0.10%)	105 (0.13%)
no tagged top [fb]	561 (0.69%)	265 (0.75%)	162 (0.20%)	$77 \cdot 10^3$ (95.64%)
all tagged tops	1783 (2.20%)	453 (1.00%)	276 (0.34%)	$78 \cdot 10^3$ (96.77%)

Table A.3: Correlation of tagged top type with and without Delphes for a semileptonic $t\bar{t}$ sample at LHC 8 TeV in fb. The percentage is relative to the the total semileptonic $t\bar{t}$ cross section.

Furthermore we see that the ratio between the number of tops in the three different types stays the same. Most of the detected tops are type 1 tops in which the subjets correspond to the decay products of the top. This can be easily explained if we look at Fig. A.3. The left and right panels show top momentum reconstruction in terms of $\Delta R(t_{tag}, t_{parton})$ and $\Delta p_T(t_{tag}, t_{parton})/p_T(t_{parton})$ with and without using Delphes. For type 1 tops we get a peak around $\Delta R = 0$ and $\Delta p_T = 0$. However, the shape of the distribution for type 2 and type 3 tops is shifted significantly due to a poor jet reconstruction that causes the wrong identification of the subjets. This could cause problems for a later analysis in which we use the tagged top momentum. If we compare the shape of these distributions with (solid line) and without (dashed line) Delphes we see no significant difference.

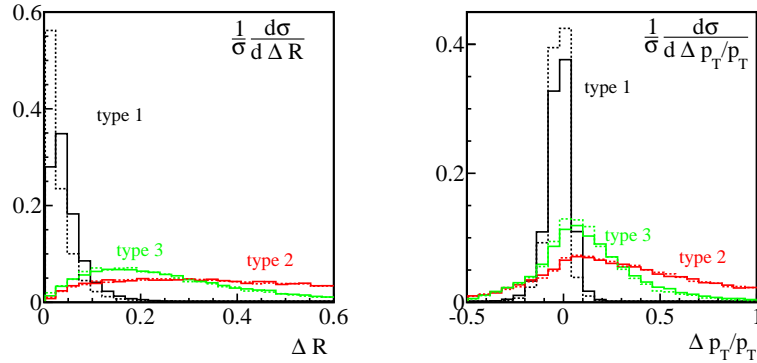


Figure A.3: Normalized distribution for $\Delta R(t_{tag}, t_{parton})$ (left) and $\Delta p_T(t_{tag}, t_{parton})/p_T(t_{parton})$ (right) for a semileptonic $t\bar{t}$ sample at LHC 8 TeV. We show type 1 (black), type 2 (red) and type 3 (green) tops separately. Solid lines denote the result with Delphes, dashed lines are results without Delphes

Now we have to look at tops that were only tagged either with or without Delphes. To understand the way the tagger processes the data we distinguish the following cases of events that may appear:

no fat jet: events with no reconstructed fat jet (Cambridge/Aachen, $R = 1.5$) that includes the top decay products

fat jet: there is at least one fat jet reconstructed where all distances ΔR between top decay products and the fat jet are less than 1.5

include: fat jets where all distances ΔR between top decay products and their closest subjets are less than 0.4

candidate: all decay products appear in a fat jet which is a top candidate within the top mass window $150 \text{ GeV} < m_{jjj}^{filter} < 200 \text{ GeV}$

Here a top candidate means that we can find three filtered hard subjets within the fat jet that fulfill the mass drop criteria described in [37] and that have a combined mass close to the top mass. At first, let us look at the case in which a top was tagged without Delphes but no top is tagged with Delphes. We will abbreviate this as "case A" and the distribution is shown in Tab. A.4.

	no fat jet	fat jet	include	candidate
case A [fb]	149 (23.6%)	479 (76.1%)	342 (54.3%)	203 (32.2%)
case B [fb]	218 (38.4%)	342 (60.9%)	252 (44.9%)	180 (32.1%)

Figure A.4: Event classification for a semileptonic $t\bar{t}$ sample at LHC 8 TeV in fb. We show the distribution for events in which a type 1 top is tagged without using Delphes but not using Delphes (case A) and vice versa (case B). The percentage is relative to the total cross section for case A and B tops.

We see that in 76% of these events, it is possible to find at least one fat jet. However, only for 54% of these fat jets it is possible to match the subjets with the decay products of a top. This is a sign that we have lost some information in at least one subjet in the detector simulation. This is what causes a poor reconstruction of a top. Therefore it is not surprising that only 32% of the fat jets are top candidates of type 1.

For the other case, in which the top is tagged using data processed by Delphes but not in the original data, shows a similar behavior. We will denote it by "case B". At first we recognize that there is a relatively large fraction of events (38 %) in which we did not even find a fat jet that includes the top decay products without using the detector simulation although we find a top of type 1 using Delphes. For the events in which we find a fat jet, in about 74% of the cases it is possible to match subjets and partons and in about 53% we can identify the fat jet as a top candidate. Again, this loss of events is a sign of a poor reconstruction of the fat jets and the subjets. Delphes changes the input data for the tagger slightly due to smearing of the momenta, a non-perfect detection of isolated leptons, and a finite detector efficiency. These small differences cause a different reconstruction history which may lead to different tagging behavior as described by case A and case B. Although there are many tagged tops that were tagged either using Delphes or not, these reconstructed tops describe the original tops very well. This we have seen in Fig. A.3 which includes these cases.

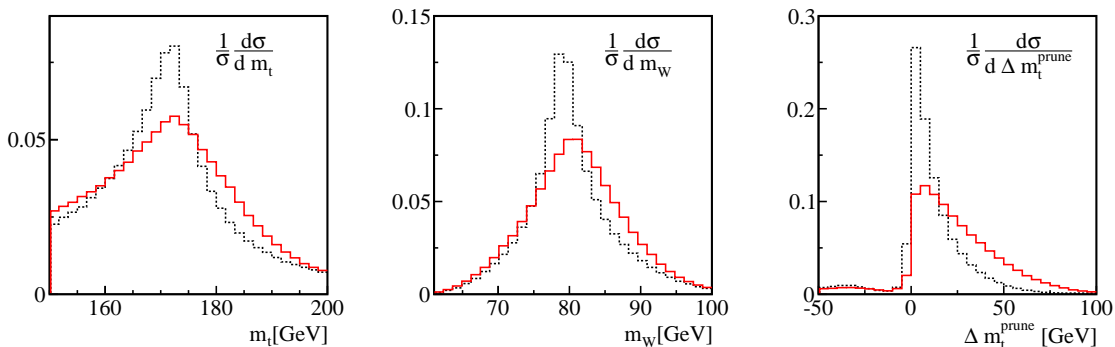


Figure A.5: Observables describing the mass of the tagged top for the t -channel single top sample: m_t (left), m_W (center) and Δm_t^{prune} (right). Solid red lines denote the result with Delphes, dashed black lines are results without Delphes. Figures taken from [41]

Finally we compare the tagging performance with and without Delphes. This is done for the t -channel single top sample. The left and central panel of Fig. A.5 show the reconstructed top mass m_t and W mass m_W distribution. We can see that both distributions are smeared out using Delphes due to detector effects. The position of the peak stays unchanged. The right panel of Fig.

A.5 shows the mass difference between the filtered top mass and the pruned top mass Δm_t^{prune} . Using Delphes, the distribution of this observable is shifted towards larger values since the pruned mass itself is more sensitive to detector effects.

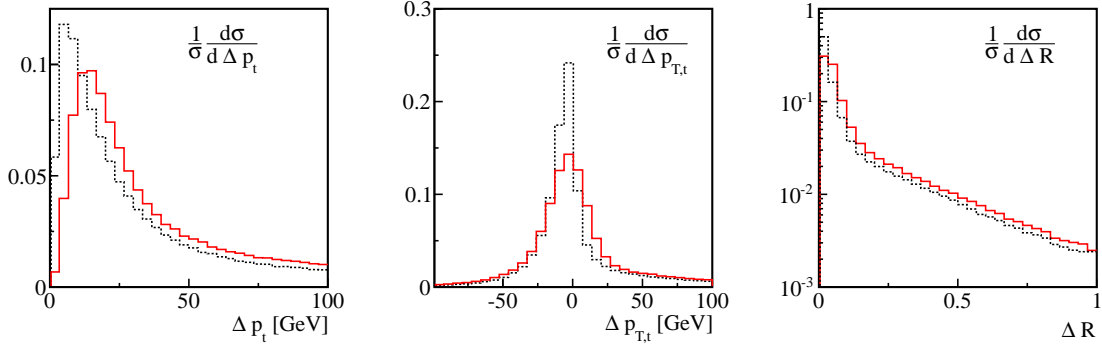


Figure A.6: Observables describing the reconstruction of the tagged top momentum for the t -channel single top sample: Δp_t (left), $\Delta p_{T,t}$ (center) and ΔR (right). Solid red lines denote the result with Delphes, dashed black lines are results without Delphes. Figures taken from [41]

In Fig. A.6 we show the differences between the reconstructed and parton-level top momentum. We show the momentum difference $\Delta p_t = |\vec{p}_t^{tag} - \vec{p}_t|$, the transverse momentum difference $\Delta p_{T,t} = p_{T,t}^{tag} - p_{T,t}$ and the distance ΔR between the tagged top momentum and the parton-level top momentum. Again, we observe a smearing of these observables but no significant difference.

A.4 Tagging efficiency

We have seen that tagging behavior does not change under the usage of Delphes. Let us now look on the tagging efficiency that is shown in Fig. A.7. In the left panel we show the tagging efficiency for semileptonic $t\bar{t}$ events as a function of the parton level top p_T normalized to the number of hadronic tops. The black curve shows the fraction of events in which a fat jet containing the top decay products exists. We see that this number is small for low p_T since we use a cut of $p_{T,min} = 200$ GeV. For high p_T , we can detect a fat jet for almost all tops. The red curve shows fat jets whose subjects match the top decay products, and the green curve the top candidates. The blue curve shows the tagged tops. For events with high enough p_T the algorithm is almost independent from p_T . Approximately half of the tops are identified as top candidates and 30% are tagged as tops. If we compare this result with the same distribution without using Delphes (denoted by the dashed lines) we see again that Delphes does not change the behavior of the tagger.

Let us now look at the tagging efficiency: the number of tagged tops relative to the number of tops in parton level with $p_T > 200$ GeV. If we average over the transverse momentum range of the parton level top with $p_T > 200$ we get a tagging efficiency of 17.8% using Delphes. This is close to the tagging efficiency without Delphes of 19.5%.

We can do the same analysis for full hadronic $t\bar{t}$ production. Due to the two hadronic tops we observe more fat jets and more tagged tops. This can be seen in the central panel of Fig. A.7. In about 26% of the events which have a parton level top with transverse momentum $p_T > 200$ GeV we tag a top. This is again close to the tagging efficiency without Delphes of 28%. For all considered samples we see that only a very small fraction of tagged tops that do not correspond to a top in parton level (purple line).

The tagging efficiencies for t -channel single top production are similar to the case of semileptonic $t\bar{t}$ production. Since there is only one top quark and one recoil jet with opposite momentum in a single top event, we expect a correct subject-parton matching for the tagged tops. Indeed, we observe that both with and without Delphes, about 99% of the tagged tops can be classified as type 1. This fraction was lower for $t\bar{t}$ events. We can reject type 2 and type 3 tops by choosing a tighter configuration of the HEPTopTagger or by applying cuts on the pruned mass. This will therefore increase the number of tagged single top events relative to the number of tagged $t\bar{t}$ events. The tagging efficiency is 18.7% with Delphes and 20.1% without Delphes for tops with transverse

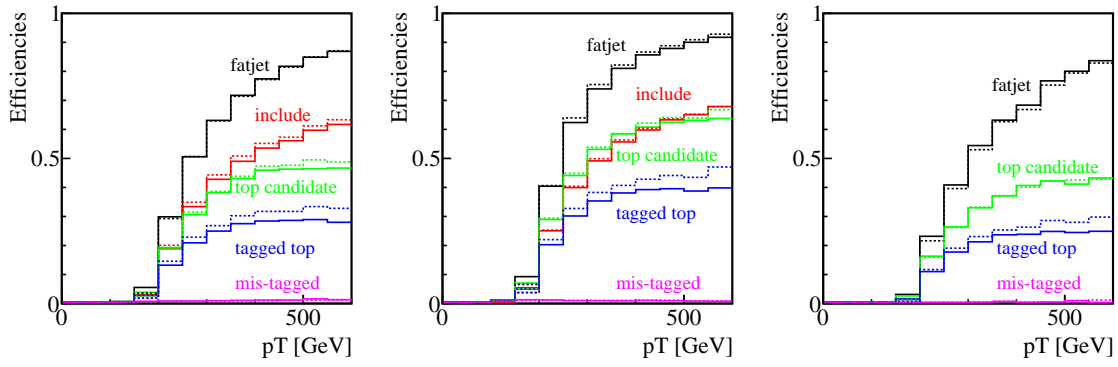


Figure A.7: Tagging efficiencies for semileptonic (left), fully hadronic (central) top pair production, and t -channel single top production (right).

momenta higher than 200 GeV. Again we see that the tagging efficiency does not change under Delphes as we can see in the right panel of Fig. A.7.

Bibliography

- [1] V. C. Rubin, W. K. J. Ford and N. Thonnard, *Rotational properties of 21 SC galaxies with a large range of luminosities and radii, from NGC 4605 $R = 4\text{kpc}$ to UGC 2885 $R = 122\text{kpc}$* , *Astrophysical Journal* **238**, 471–487 (1980).
- [2] N. Jarosik, C. Bennett, J. Dunkley, B. Gold, M. Greason et al., *Seven-Year Wilkinson Microwave Anisotropy Probe (WMAP) Observations: Sky Maps, Systematic Errors, and Basic Results*, *Astrophys.J.Suppl.* **192**, 14 (2011), [arXiv:1001.4744 \[astro-ph.CO\]](#).
- [3] A. G. R. Saul Perlmutter, Brian P. Schmidt, *The accelerating universe*, The Royal Swedish Academy of Sciences, Kungl. Vetenskaps-Akademien (2011), Scientific Background on the Nobel Prize in Physics 2011.
- [4] J. A. Frieman, *Lectures on dark energy and cosmic acceleration*, *AIP Conf.Proc.* **1057**, 87–124 (2008), [arXiv:0904.1832 \[astro-ph.CO\]](#).
- [5] S. P. Martin, *A Supersymmetry primer*, (1997), [arXiv:9709356 \[hep-ph\]](#).
- [6] Beringer, J. et al., (*Particle Data Group*), *PR* **D86** (2012), <http://pdg.lbl.gov/2012/listings/rpp2012-list-neutrino-prop.pdf>.
- [7] M. Trodden, *Electroweak baryogenesis*, *Rev.Mod.Phys.* **71**, 1463–1500 (1999), [arXiv:9803479 \[hep-ph\]](#).
- [8] (Tevatron Electroweak Working Group, CDF and D0 Collaborations), *Combination of CDF and D0 results on the mass of the top quark using up to 5.8 fb^{-1} of data*, (2011), [arXiv:1107.5255 \[hep-ex\]](#).
- [9] V. Abazov et al. (D0 Collaboration), *Experimental discrimination between charge $2e/3$ top quark and charge $4e/3$ exotic quark production scenarios*, *Phys.Rev.Lett.* **98**, 041801 (2007), [arXiv:0608044 \[hep-ex\]](#).
- [10] (CDF Collaboration Collaboration), *The CDF Measurement of the Top Quark Charge using the Top Decay Products in Lepton+Jet channel*, CDF conference note **10460** (2011), www-cdf.fnal.gov/physics/new/top/2011/topQLJ/cdf10460_topq_56invsb.pdf.
- [11] T. Aaltonen et al. (CDF, D0 Collaboration), *Combination of CDF and D0 measurements of the W boson helicity in top quark decays*, (2012), [arXiv:1202.5272 \[hep-ex\]](#).
- [12] T. E. W. Group (CDF and D0 Collaborations), *Combination of CDF and D0 Measurements of the Single Top Production Cross Section*, (2009), [arXiv:0908.2171 \[hep-ex\]](#).
- [13] T. M. Tait and C.-P. Yuan, *Single top quark production as a window to physics beyond the standard model*, *Phys.Rev.* **D63**, 014018 (2000), [arXiv:0007298 \[hep-ph\]](#).
- [14] J. Alwall, R. Frederix, J.-M. Gerard, A. Giammanco, M. Herquet et al., *Is $V(tb) = 1?$* , *Eur.Phys.J.* **C49**, 791–801 (2007), [arXiv:0607115 \[hep-ph\]](#).
- [15] D. E. Morrissey, T. Plehn and T. M. Tait, *Physics searches at the LHC*, *Phys.Rept.* **515**, 1–113 (2012), [arXiv:0912.3259 \[hep-ph\]](#).
- [16] T. Aaltonen et al. (CDF Collaboration), *First Observation of Electroweak Single Top Quark Production*, *Phys.Rev.Lett.* **103**, 092002 (2009), [arXiv:0903.0885 \[hep-ex\]](#).

- [17] T. Aaltonen et al. (CDF Collaboration), *Observation of Single Top Quark Production and Measurement of $|V_{tb}|$ with CDF*, Phys.Rev. **D82**, 112005 (2010), arXiv:1004.1181 [hep-ex].
- [18] V. Abazov et al. (D0 Collaboration), *Observation of Single Top Quark Production*, Phys.Rev.Lett. **103**, 092001 (2009), arXiv:0903.0850 [hep-ex].
- [19] V. Abazov et al. (D0 Collaboration), *Measurement of the t -channel single top quark production cross section*, Phys.Lett. **B682**, 363–369 (2010), arXiv:0907.4259 [hep-ex].
- [20] V. Abazov et al. (D0 Collaboration Collaboration), *Measurements of single top quark production cross sections and $|V_{tb}|$ in $p\bar{p}$ collisions at $\sqrt{s} = 1.96$ TeV*, Phys.Rev. **D84**, 112001 (2011), arXiv:1108.3091 [hep-ex].
- [21] (CDF Collaboration Collaboration), *Measurement of Single Top Quark Production in 7.5 fb^{-1} of CDF Data Using Neural Networks*, CDF conference note **10793** (2012), www-cdf.fnal.gov/physics/new/top/confNotes/cdf10793_SingleTop_7.5_public.pdf.
- [22] V. Abazov et al. (D0 Collaboration Collaboration), *Model-independent measurement of t -channel single top quark production in $p\bar{p}$ collisions at $\sqrt{s} = 1.96$ TeV*, Phys.Lett. **B705**, 313–319 (2011), arXiv:1105.2788 [hep-ex].
- [23] J. Thaler and L.-T. Wang, *Strategies to Identify Boosted Tops*, JHEP **0807**, 092 (2008), arXiv:0806.0023 [hep-ph].
- [24] I. W. Stewart, F. J. Tackmann and W. J. Waalewijn, *N -Jettiness: An Inclusive Event Shape to Veto Jets*, Phys.Rev.Lett. **105**, 092002 (2010), arXiv:1004.2489 [hep-ph].
- [25] D. E. Kaplan, K. Rehermann, M. D. Schwartz and B. Tweedie, *Top Tagging: A Method for Identifying Boosted Hadronically Decaying Top Quarks*, Phys.Rev.Lett. **101**, 142001 (2008), arXiv:0806.0848 [hep-ph].
- [26] L. G. Almeida, S. J. Lee, G. Perez, I. Sung and J. Virzi, *Top Jets at the LHC*, Phys.Rev. **D79**, 074012 (2009), arXiv:0810.0934 [hep-ph].
- [27] A. Hook, M. Jankowiak and J. G. Wacker, *Jet Dipolarity: Top Tagging with Color Flow*, JHEP **1204**, 007 (2012), arXiv:1102.1012 [hep-ph].
- [28] T. Plehn and M. Spannowsky, *Top Tagging*, (2011), arXiv:1112.4441 [hep-ph].
- [29] D. Krohn, J. Thaler and L.-T. Wang, *Jets with Variable R* , JHEP **0906**, 059 (2009), arXiv:0903.0392 [hep-ph].
- [30] D. Krohn, J. Thaler and L.-T. Wang, *Jet Trimming*, JHEP **1002**, 084 (2010), arXiv:0912.1342 [hep-ph].
- [31] S. D. Ellis, A. Hornig, T. S. Roy, D. Krohn and M. D. Schwartz, *Qjets: A Non-Deterministic Approach to Tree-Based Jet Substructure*, Phys.Rev.Lett. **108**, 182003 (2012), arXiv:1201.1914 [hep-ph].
- [32] I. Feige, M. Schwartz, I. Stewart and J. Thaler, *Precision Jet Substructure from Boosted Event Shapes*, (2012), arXiv:1204.3898 [hep-ph].
- [33] L. G. Almeida, S. J. Lee, G. Perez, G. F. Sterman, I. Sung et al., *Substructure of high- p_T Jets at the LHC*, Phys.Rev. **D79**, 074017 (2009), arXiv:0807.0234 [hep-ph].
- [34] M. Jankowiak and A. J. Larkoski, *Jet Substructure Without Trees*, JHEP **1106**, 057 (2011), arXiv:1104.1646 [hep-ph].
- [35] A. Altheimer, S. Arora, L. Asquith, G. Brooijmans, J. Butterworth et al., *Jet Substructure at the Tevatron and LHC: New results, new tools, new benchmarks*, J.Phys.G **G39**, 063001 (2012), arXiv:1201.0008 [hep-ph].
- [36] T. Plehn, G. P. Salam and M. Spannowsky, *Fat Jets for a Light Higgs*, Phys.Rev.Lett. **104**, 111801 (2010), arXiv:0910.5472 [hep-ph].

- [37] T. Plehn, M. Spannowsky, M. Takeuchi and D. Zerwas, *Stop Reconstruction with Tagged Tops*, JHEP **1010**, 078 (2010), [arXiv:1006.2833 \[hep-ph\]](#).
- [38] T. Plehn, M. Spannowsky and M. Takeuchi, *Boosted Semileptonic Tops in Stop Decays*, JHEP **1105**, 135 (2011), [arXiv:1102.0557 \[hep-ph\]](#).
- [39] T. Plehn, M. Spannowsky and M. Takeuchi, *How to Improve Top Tagging*, Phys.Rev. **D85**, 034029 (2012), [arXiv:1111.5034 \[hep-ph\]](#).
- [40] T. Plehn, M. Spannowsky and M. Takeuchi, *Stop searches in 2012*, (2012), [arXiv:1205.2696 \[hep-ph\]](#).
- [41] F. Kling, T. Plehn and M. Takeuchi, *Tagging single Tops*, (2012), [arXiv:1207.4787 \[hep-ph\]](#).
- [42] M. E. Peskin and D. V. Schroeder, *An Introduction to Quantum Field Theory*, Westview Press, 1. edition, 1995.
- [43] M. Srednicki, *Quantum field theory*, Cambridge University Press, 1. edition, 2007.
- [44] T. Plehn, *Lectures on LHC Physics*, Lect.Notes Phys. **844**, 1–193 (2012), [arXiv:0910.4182 \[hep-ph\]](#).
- [45] Beringer, J. et al., (*Particle Data Group*), PR **D86** (2012), <http://pdg.lbl.gov/2012/tables/rpp2012-sum-quarks.pdf>.
- [46] Beringer, J. et al., (*Particle Data Group*), PR **D86** (2012), <http://pdg.lbl.gov/2012/tables/rpp2012-sum-leptons.pdf>.
- [47] F. Gianotti (ATLAS Collaboration), *Update on the Standard Model Higgs search in ATLAS*, ATLAS-CONF-2012-093 (July, 4 2012).
- [48] J. Incandela (ATLAS Collaboration), *Update on the Standard Model Higgs search in CMS*, CMS-PAS-HIG-12-020 (July, 4 2012).
- [49] G. P. Salam, *Towards Jetography*, Eur.Phys.J. **C67**, 637–686 (2010), [arXiv:0906.1833 \[hep-ph\]](#).
- [50] M. Dasgupta, L. Magnea and G. P. Salam, *Non-perturbative QCD effects in jets at hadron colliders*, JHEP **0802**, 055 (2008), [arXiv:0712.3014 \[hep-ph\]](#).
- [51] M. Cacciari, G. P. Salam and S. Sapeta, *On the characterisation of the underlying event*, JHEP **1004**, 065 (2010), [arXiv:0912.4926 \[hep-ph\]](#).
- [52] K. Jakobs, *Physics at the LHC – From Standard Model measurements to Searches for New Physics*, (2012), [arXiv:1206.7024 \[hep-ex\]](#).
- [53] M. Kobayashi and T. Maskawa, *CP-Violation in the Renormalizable Theory of Weak Interaction*, Progress of Theoretical Physics **49**, 652–657 (1973).
- [54] F. Abe and et al. (CDF Collaboration), *Observation of Top Quark Production in $p\bar{p}$ Collisions with the Collider Detector at Fermilab*, Physical Review Letters **74**, 2626–2631 (1995), [arXiv:9503002 \[hep-ex\]](#).
- [55] S. Abachi and et al. (D0 Collaboration), *Search for High Mass Top Quark Production in $p\bar{p}$ Collisions at $s = 1.8$ TeV*, Physical Review Letters **74**, 2422–2426 (1995), [arXiv:9411001 \[hep-ex\]](#).
- [56] Beringer, J. et al., (*Particle Data Group*), PR **D86** (2012), <http://pdg.lbl.gov/2012/listings/rpp2012-list-t-quark.pdf>.
- [57] P. Meade and M. Reece, *Top partners at the LHC: Spin and mass measurement*, Phys.Rev. **D74**, 015010 (2006), [arXiv:hep-ph/0601124 \[hep-ph\]](#).

- [58] T. Aaltonen et al. (CDF Collaboration), *Forward-Backward Asymmetry in Top Quark Production in $p\bar{p}$ Collisions at $\sqrt{s} = 1.96$ TeV*, Phys.Rev.Lett. **101**, 202001 (2008), arXiv:0806.2472 [hep-ex].
- [59] V. M. Abazov et al. (D0 Collaboration Collaboration), *Forward-backward asymmetry in top quark-antiquark production*, Phys.Rev. **D84**, 112005 (2011), arXiv:1107.4995 [hep-ex].
- [60] N. Kidonakis, *Top Quark Theoretical Cross Sections and p_T and Rapidity Distributions*, (2011), arXiv:1109.3231 [hep-ph].
- [61] Beringer, J. et al., (*Particle Data Group*), PR **D86** (2012), <http://pdg.lbl.gov/2012/reviews/rpp2012-rev-ckm-matrix.pdf>.
- [62] G. Mahlon, *Observing spin correlations in single top production and decay*, (2000), arXiv:0011349 [hep-ph].
- [63] T. Chwalek (CDF and D0 Collaborations), *Measurement of the W^- boson helicity fractions in top-quark decays at CDF*, pages 487–490 (2007), arXiv:0705.2966 [hep-ex].
- [64] K. Rehermann and B. Tweedie, *Efficient Identification of Boosted Semileptonic Top Quarks at the LHC*, JHEP **1103**, 059 (2011), arXiv:1007.2221 [hep-ph].
- [65] Y. L. Dokshitzer, G. Leder, S. Moretti and B. Webber, *Better jet clustering algorithms*, JHEP **9708**, 001 (1997), arXiv:9707323 [hep-ph].
- [66] M. Cacciari and G. P. Salam, *Dispelling the N^3 myth for the k_t jet-finder*, Phys.Lett. **B641**, 57–61 (2006), arXiv:0512210 [hep-ph].
- [67] M. Cacciari, G. P. Salam and G. Soyez, *FastJet user manual*, Eur.Phys.J. **C72**, 1896 (2012), arXiv:1111.6097 [hep-ph].
- [68] J. M. Butterworth, A. R. Davison, M. Rubin and G. P. Salam, *Jet substructure as a new Higgs search channel at the LHC*, Phys.Rev.Lett. **100**, 242001 (2008), arXiv:0802.2470 [hep-ph].
- [69] S. D. Ellis, C. K. Vermilion and J. R. Walsh, *Techniques for improved heavy particle searches with jet substructure*, Phys.Rev. **D80**, 051501 (2009), arXiv:0903.5081 [hep-ph].
- [70] S. D. Ellis, C. K. Vermilion and J. R. Walsh, *Recombination Algorithms and Jet Substructure: Pruning as a Tool for Heavy Particle Searches*, Phys.Rev. **D81**, 094023 (2010), arXiv:0912.0033 [hep-ph].
- [71] C. K. Vermilion, *Jet Substructure at the Large Hadron Collider: Harder, Better, Faster, Stronger*, (2011), arXiv:1101.1335 [hep-ph].
- [72] J. R. Walsh and S. Zuberi, *Factorization Constraints on Jet Substructure*, (2011), arXiv:1110.5333 [hep-ph].
- [73] T. Plehn, M. Rauch and M. Spannowsky, *Understanding Single Tops using Jets*, Phys.Rev. **D80**, 114027 (2009), arXiv:0906.1803 [hep-ph].
- [74] G. Aad et al. (ATLAS Collaboration Collaboration), *Measurement of the t -channel single top-quark production cross section in pp collisions at $\sqrt{s} = 7$ TeV with the ATLAS detector*, (2012), arXiv:1205.3130 [hep-ex].
- [75] G. Aad et al. (ATLAS Collaboration Collaboration), *Evidence for the associated production of a W boson and a top quark in ATLAS at $\sqrt{s} = 7$ TeV*, (2012), arXiv:1205.5764 [hep-ex].
- [76] S. Chatrchyan et al. (CMS Collaboration Collaboration), *Measurement of the t -channel single top quark production cross section in pp collisions at $\sqrt{s} = 7$ TeV*, Phys.Rev.Lett. **107**, 091802 (2011), arXiv:1106.3052 [hep-ex].

- [77] M. L. Mangano, M. Moretti, F. Piccinini, R. Pittau and A. D. Polosa, *ALPGEN, a generator for hard multiparton processes in hadronic collisions*, JHEP **0307**, 001 (2003), [arXiv:0206293 \[hep-ph\]](#).
- [78] T. Sjostrand, S. Mrenna and P. Z. Skands, *PYTHIA 6.4 Physics and Manual*, JHEP **0605**, 026 (2006), [arXiv:0603175 \[hep-ph\]](#).
- [79] T. Sjostrand, S. Mrenna and P. Z. Skands, *A Brief Introduction to PYTHIA 8.1*, Comput.Phys.Commun. **178**, 852–867 (2008), [arXiv:0710.3820 \[hep-ph\]](#).
- [80] M. L. Mangano, M. Moretti, F. Piccinini and M. Treccani, *Matching matrix elements and shower evolution for top-quark production in hadronic collisions*, JHEP **0701**, 013 (2007), [arXiv:0611129 \[hep-ph\]](#).
- [81] N. Kidonakis, *Differential and total cross sections for top pair and single top production*, (2012), [arXiv:1205.3453 \[hep-ph\]](#).
- [82] N. Kidonakis, *NNLL resummation for s-channel single top quark production*, Phys.Rev. **D81**, 054028 (2010), [arXiv:1001.5034 \[hep-ph\]](#).
- [83] N. Kidonakis, *Next-to-next-to-leading-order collinear and soft gluon corrections for t-channel single top quark production*, Phys.Rev. **D83**, 091503 (2011), [arXiv:1103.2792 \[hep-ph\]](#).
- [84] N. Kidonakis, *Top Quark Cross Sections and Differential Distributions*, (2011), [arXiv:1105.3481 \[hep-ph\]](#).
- [85] N. Kidonakis, *Next-to-next-to-leading soft-gluon corrections for the top quark cross section and transverse momentum distribution*, Phys.Rev. **D82**, 114030 (2010), [arXiv:1009.4935 \[hep-ph\]](#).
- [86] N. Kidonakis, *Two-loop soft anomalous dimensions for single top quark associated production with a W- or H-*, Phys.Rev. **D82**, 054018 (2010), [arXiv:1005.4451 \[hep-ph\]](#).
- [87] S. Ovnyn, X. Rouby and V. Lemaitre, *DELPHES, a framework for fast simulation of a generic collider experiment*, (2009), [arXiv:0903.2225 \[hep-ph\]](#).
- [88] G. Aad et al. (ATLAS Collaboration Collaboration), *Expected Performance of the ATLAS Experiment - Detector, Trigger and Physics*, page 79 (2009), [arXiv:0901.0512 \[hep-ex\]](#).
- [89] Piacquadio, G., *Identification of b-jets and investigation of the discovery potential of a Higgs boson in the WH channel with the ATLAS experiment*, (2010), CERN-THESIS-2010-027.
- [90] D. Sosa, G. Kasieczka, S. Schaetzel and A. Schoening, *HEPTopTagger Optimisation Studies*, DPG conference talk **T 36.7** (2012).
- [91] M. Heldmann and D. Cavalli, *An improved tau-Identification for the ATLAS experiment*, Technical Report ATL-PHYS-PUB-2006-008. ATL-COM-PHYS-2006-010, CERN, Geneva, Dec 2005.
- [92] M. Dobbs and J. Hansen, *The HepMC C++ Monte Carlo event record for High Energy Physics*, Comput. Phys. Commun. **134**, 41–46 (2001).

STATEMENT OF AUTHORSHIP

Ich versichere, dass ich diese Arbeit selbstständig verfasst habe und keine anderen als die angegebenen Quellen und Hilfsmittel benutzt habe.

Heidelberg, den

FELIX KLING